2015 POLinSAR-Course, Frascati, Jan 19 - 23

WMB Concluding Lecture, 2015 January 23, 1600 - 1730

The Vector Electromagnetic Spectrum with its strong polarization dependences across all spectral bands, and especially for POLinSAR sensing and imaging:

Future Perspectives of Radar Polarimetry and its Applications - Reduced Version -

Wolfgang-Martin Boerner

UIC-ECE Communications, Sensing & Navigation Laboratory
900 W. Taylor St., SEL (607) W-4210, M/C 154, CHICAGO IL/USA-60607-7018
T&F: +[1] (312) 996-5480, Email: wmb1uic@yahoo.com

Summary

- With the un-abating global population increase our natural resources are stressed as never before, and the global day/night monitoring of the terrestrial covers from the mesosphere to the litho-sphere becomes all the more urgent.

- Microwave radar sensors ~~are~~ ideally suited for space imaging because those are almost weather independent, and microwaves propagate through the atmosphere with little deteriorating effects due to clouds, storms, rain, fog aerosol and haze: Globally humidity, haze and aerosols next to cloudiness are increasing at a rather rapid pace.

- Thus, optical remote sensing from space especially in the tropical and sub-tropical vegetated belts is already and will become ever more ineffective, and microwave remote sensing technology must now be advanced strongly and most rapidly hand in hand with digital communications technology.

Summary continued

- The basic radar technologies to do the job at day and night are the multimodal Synthetic Aperture Radar (SAR) sensors, first developed for air-borne sensing implemented as for example in 1978 with the first space-borne digital Sea-Sat L-Band SAR which had severe limitations in that it was of fixed wide swath-width at a single arbitrary polarization (HH) and of rather poor 25m resolution.
- In the meantime, fully polarimetric multi-modal high resolution SAR systems at multiple frequencies and incidence angles were introduced first with the multi-band AIRSAR of NASA-JPL culminating in the once-only pair of SIR-C/X-SAR shuttle missions of 1994 April & October. This resulted in true day/night space remote sensing of the terrestrial barren and vegetated land and ocean covers using multi-band polarimetric SAR.
- Thereafter, the Canadian CCRS, the German DLR and the Japanese NASDA & CRL {now JAXA & NICT} took over steadily advancing the Convair-580, the E-SAR (now F-SAR) and Pi-SAR airborne highly advanced fully polarimetric sensors platforms, respectively.

Summary continued

- These separate international multi-modal fully polarimetric and also interferometric airborne SAR developmental efforts culminated in a well coordinated group effort of three independent teams eventually launching and operating Fully Polarimetric Satellite SAR Sensors :
- L-Band (ALOS-PALSAR-I launched by JAXA/Japan in 2006 January with ALOS-PALSAR-II launched by JAXA/Japan in 2014 May 24;
- C-Band (RADARSAT-2 launched by CSA-MDA in 2007 December
- X-Band (TerraSAR-X launched by DLR-Astrium in 2007 July with the follow-on tandem mission TanDEM-X launched in June 2010) .

- **Thus, international collaboration on advancing day & night global monitoring of the terrestrial covers was demonstrated with the launch of the set of three fully polarimetric multi-modal SAR Satellites at L-, C-, X-Band and its first tandem satellite-pair update of the DLR TanDEM-X**
- **These efforts will be topped by the near-future joint DLR-JPL/JAXA DESDynI/Tandem-L wide-swath, high-resolution fully polarimetric sensor implementation for both polar and equatorially orbiting satellite sensors.**

Research Collaborators

Wolfgang-Martin Boerner & Jorge J. Morisaki
ECE/CSN, University of Illinois at Chicago, USA
Alberto Moreira, Gerhard Krieger, Andreas Reigber
Kostas P. Papathanassiou, Irena Hajnsek
Richard Bamler, Michael Eineder
DLR (German Aerospace Centre), Oberpfaffenhofen, Germany
Eric Pottier, Laurent Ferro-Famil
IETR, UMR CNRS-6164, PMOR, Campus de Beaulieu, Rennes, France
Ridha Touzi
Canadian Centre for Remote Sensing, CCRS, Ottawa, Canada
Yoshio Yamaguchi, Hiroyoshi Yamada, Ryoichi Sato
Niigata University, Info-Eng, Niigata, Japan
Jakob J. van Zyl, Scott Hensley, Paul A. Rosen
CALTEC=NASA/JPL, Pasadena, CA, USA
Gopala Venkataraman, Gulab Singh
IIT-Bombay, Powai, Maharashtra, India
Jong-Sen Lee, Tom L. Ainsworth
Naval Research Laboratory (NRL), Washington, DC, USA
Kun-Shan Chen , Chih-Tien Wang, Chung-Pai Chang
CSRSR, National Central University, Taiwan
Wooil Moon & Duk-Jin Kim
ESI3, Seoul National University, Kwanuk-ku, Seoul, Korea
Joong-Sun Won & Lee Seung-Kuk
ESS, Yonsei University, Seodaemun-ku, Korea
Josaphat Tetuko Sri Sumanyo & Katsumi Hattori
CEReS, Chiba University, Nishi-Chiba, Japan
Tat-sun Yeo & Hong-bo Sun, Kye-Yak See
National University Singapore & Nanyang Technological University

Apollo 11: 1969 July 16 – 24: Neil Armstrong, Michael Collins, Edwin Aldrin, Jr.

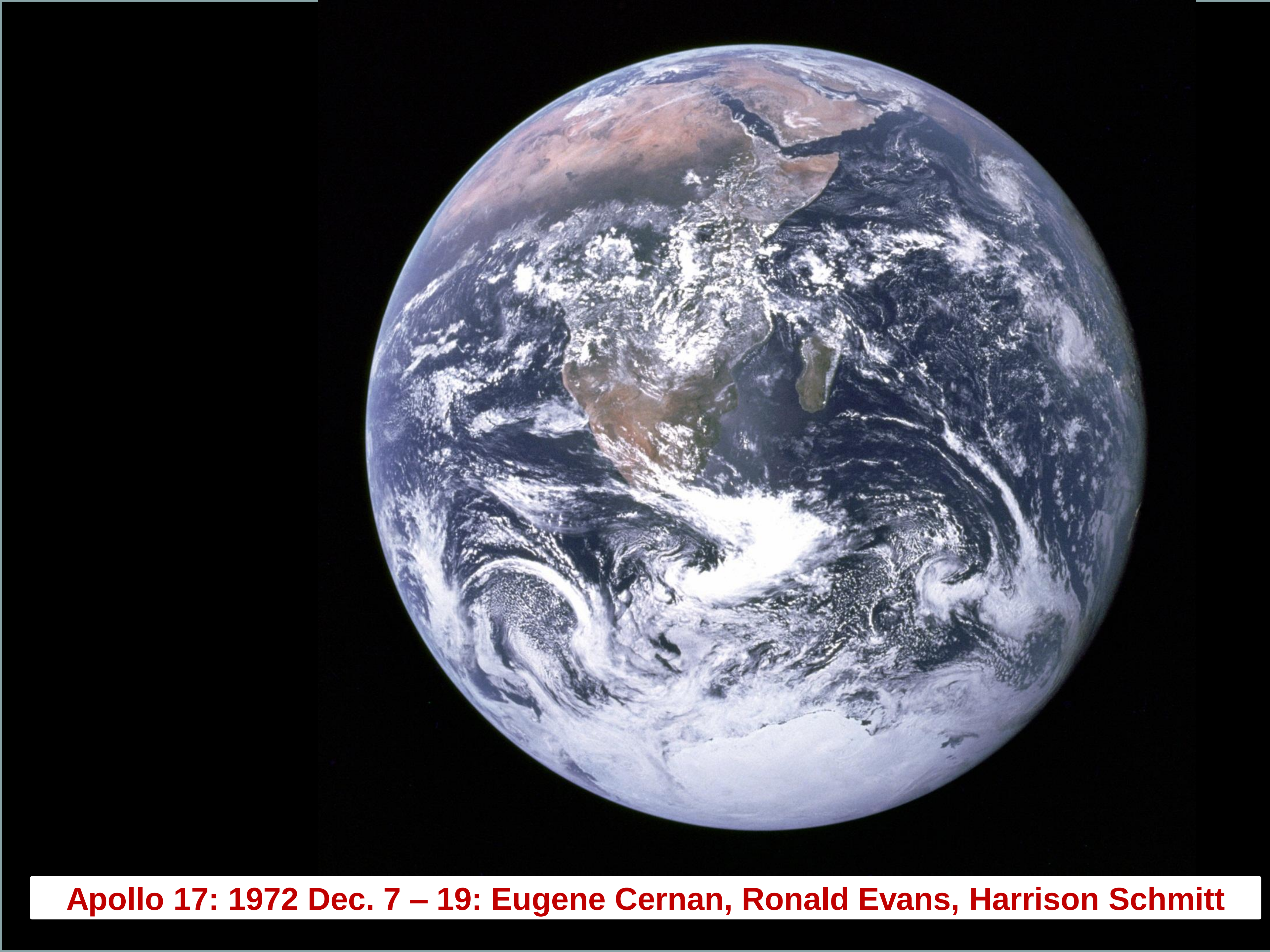

Apollo 17: 1972 Dec. 7 – 19: Eugene Cernan, Ronald Evans, Harrison Schmitt

Evolutionary Development of Planet Earth:

- Wegner – 1912
  - Discovering Plate Tectonics

- Hilgenberg – 1932
- Exploring Historical Planetary Evolution
- Of Planet Earth

The terrestrial tectonology: Alfred Wegener’s tectonic plate theory and the two major seismic belts

The theory of plate tectonics was pioneered by Alfred Wegener in the early 20th C. He was originally drawn to the idea when he tried to explain the ancient climates.

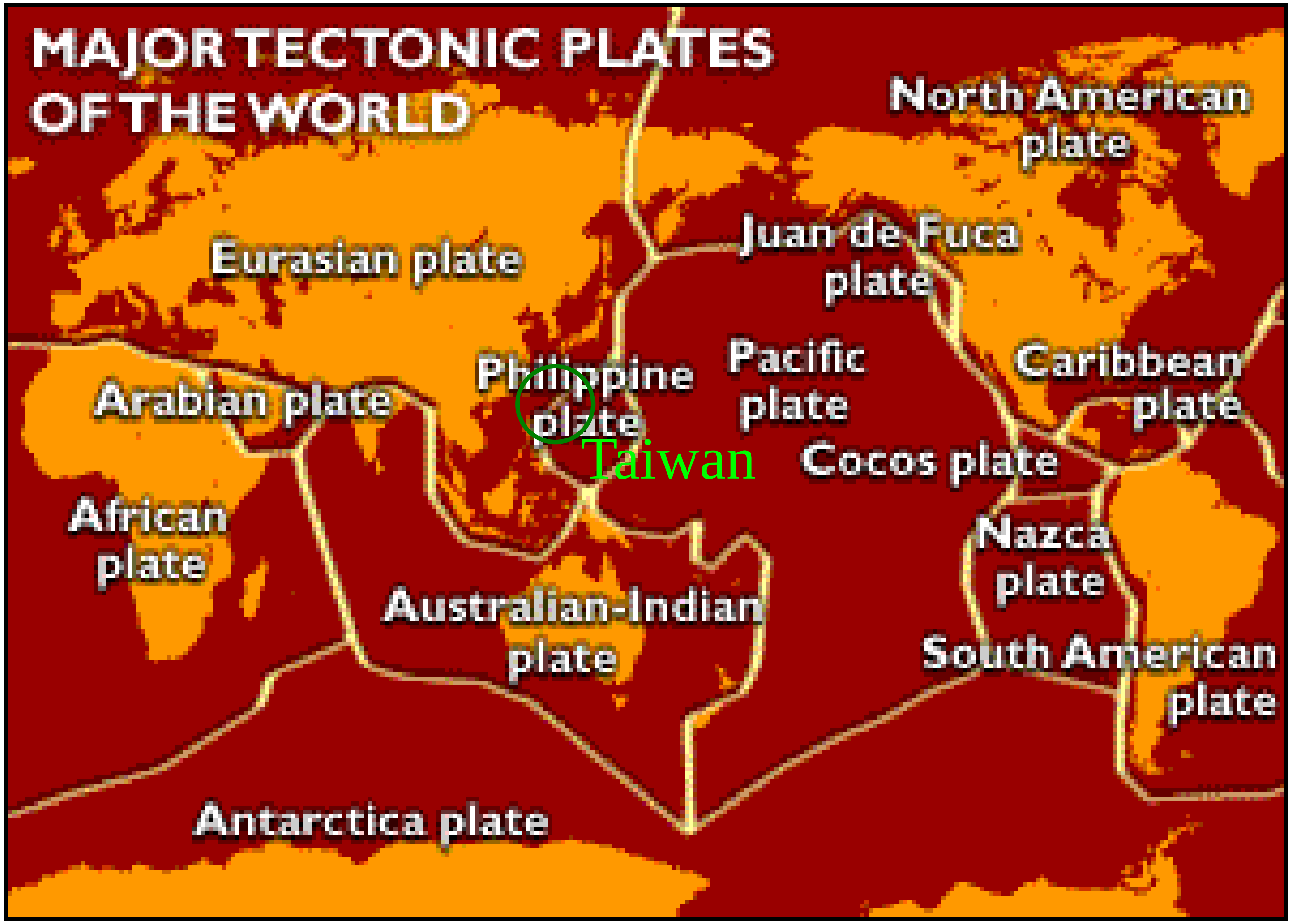

From BBC news site

EARTH'S EXPANSION

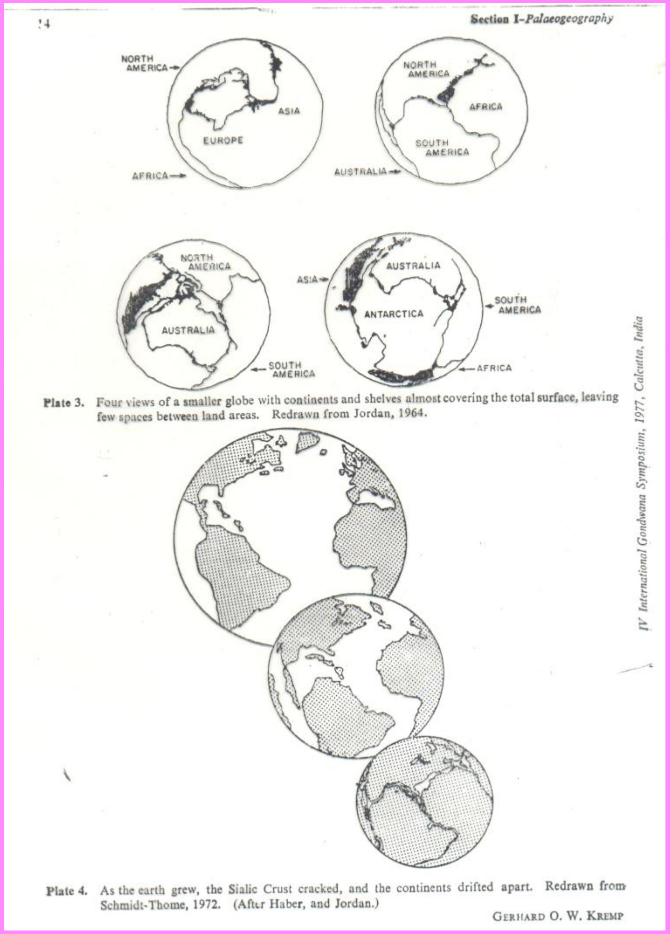
14

Section I–*Palaeogeography*

Plate 3. Four views of a smaller globe with continents and shelves almost covering the total surface, leaving few spaces between land areas. Redrawn from Jordan, 1964.

IV International Gondwana Symposium, 1977, Calcutta, India

Plate 4. As the earth grew, the Sialic Crust cracked, and the continents drifted apart. Redrawn from Schmidt-Thome, 1972. (After Haber, and Jordan.)

GERHARD O. W. KREMP

EARTH'S EXPANSION

1932 HILGENBERG Model of Primondial Earth

• O. C. Hilgenberg of Germany in 1933 showed that if the radius in a model of earth could be reduced to two-third of its length, all the continental blocks could be adjusted in a perfectly snug-fit manner. The concept of earth's expansion was revived in the 1960s by S. W. Carey of Australia.

• It can be noted that in the primordial small earth there were no oceans although epicontinental seas or lakes were present. The ocean-forming water at that stage must have been associated with the mantle. Under such condition, namely, association of large quantum of water under pressure, the mantle rock must have been considerably fluid (Sen, 1983-2003).

• **This vital clue has been based on experimental studies conducted by Roy and Tuttle (1961) confirming depression of melting point of silicate rocks under hydrothermal and ultrahigh pressure condition.**

Internal structure of the expanded earth

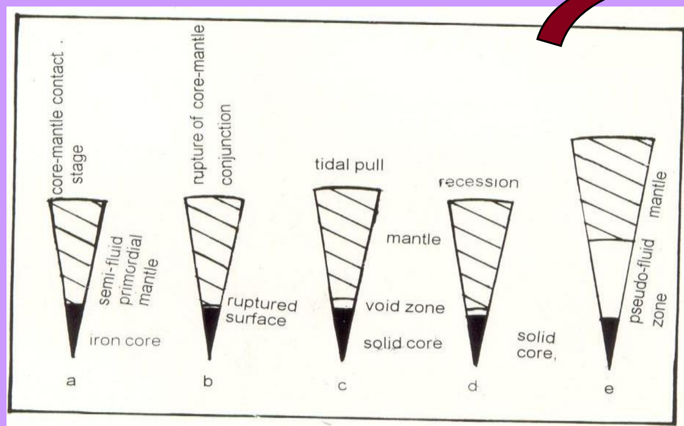

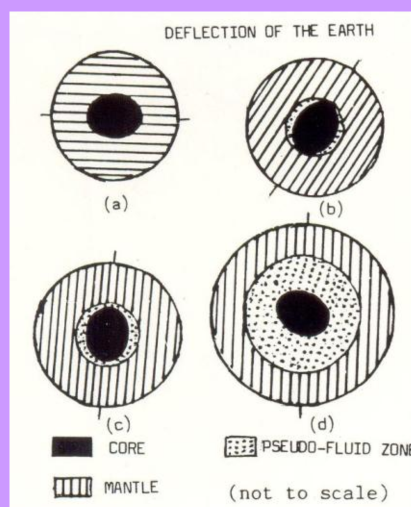

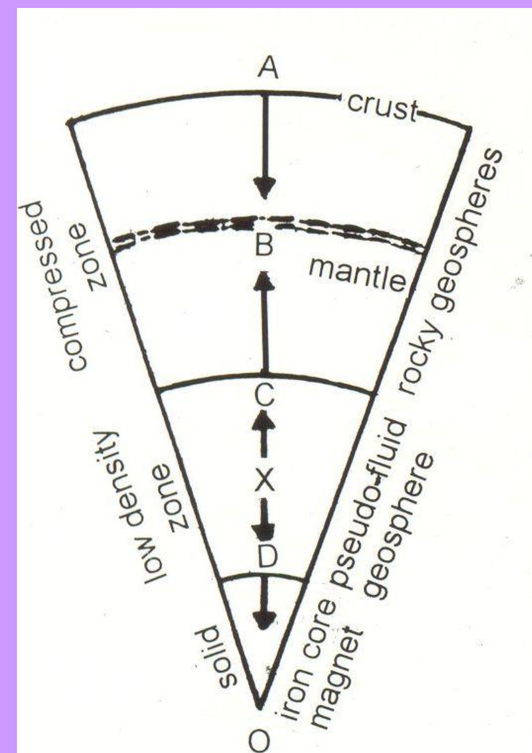

Fundamental Earth Parameters

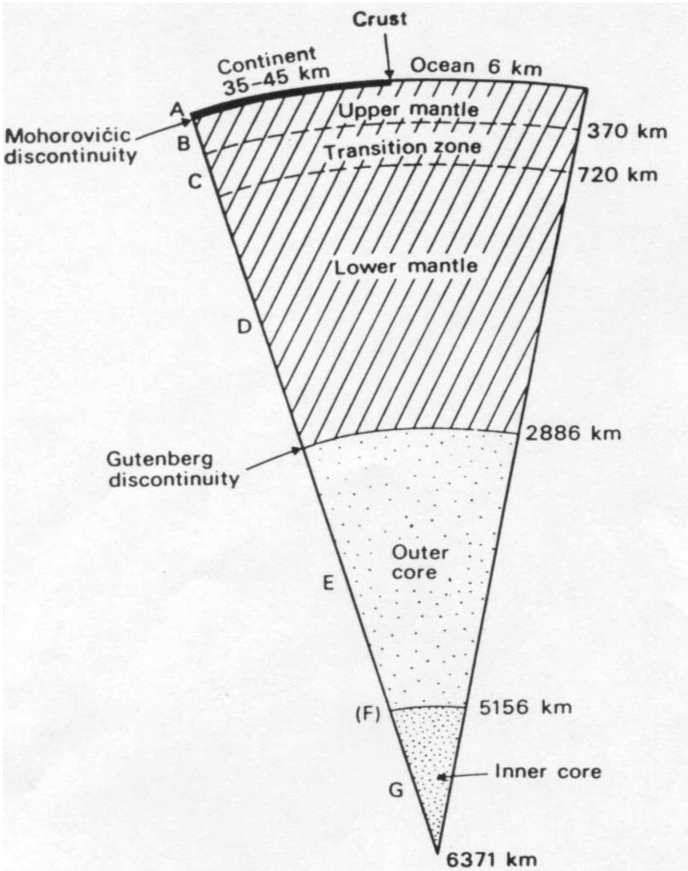

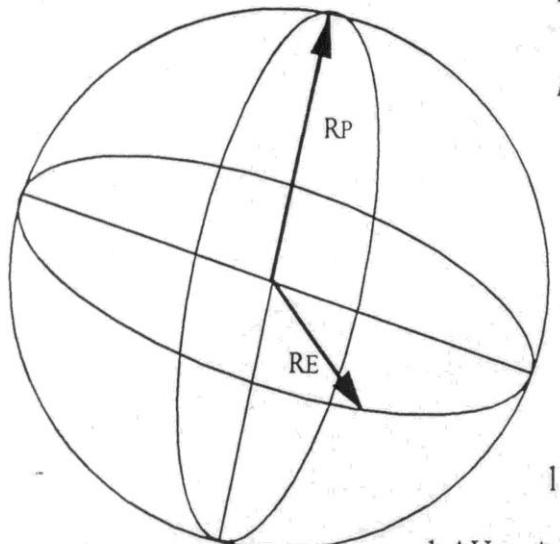

$R_{EQUATOR} \cong 6.378 \times 10^6 m$

$R_{POLAR} \cong 6.356 \times 10^6 m$

$L = 2\pi R \qquad L_E \cong 40,054 km$

$L_P = 39,918 km$

1 mi = 5280 ft = 1.609 km

1 AU ≡ Astronomial Unit = 1.496×10^{11} m

The layering within the planet earth and its equatorial and polar radius

Introduction: Why is “Air- and Space-borne Multimodal SAR Remote Sensing” of relevance to Applications in Geology and Tectonology

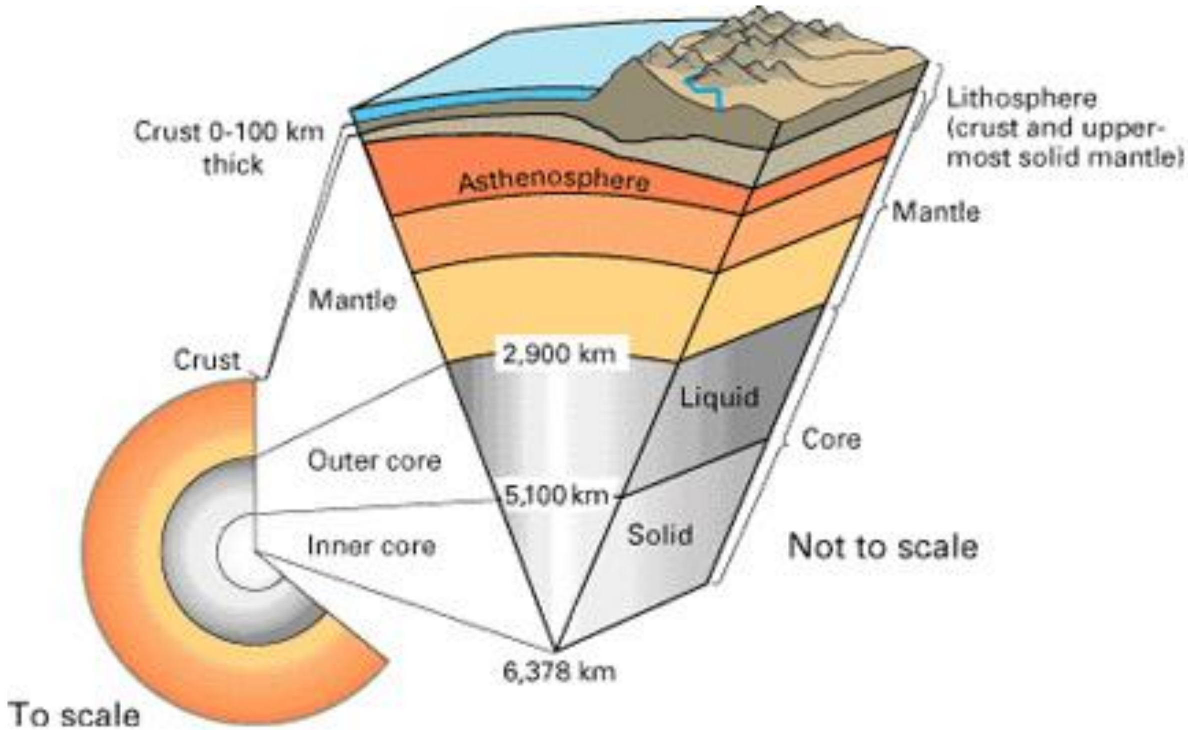

Earth Layers

Introduction: Why is "Air- and Space-borne Multimodal SAR Remote Sensing" of relevance to Applications in Geology and Tectonology

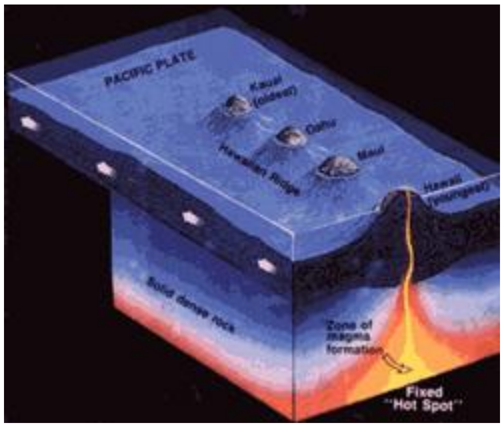

Hawaii Hotspots

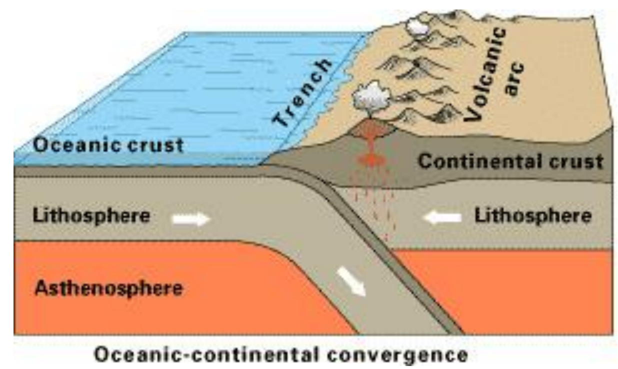

Ocean-Continent Convergence

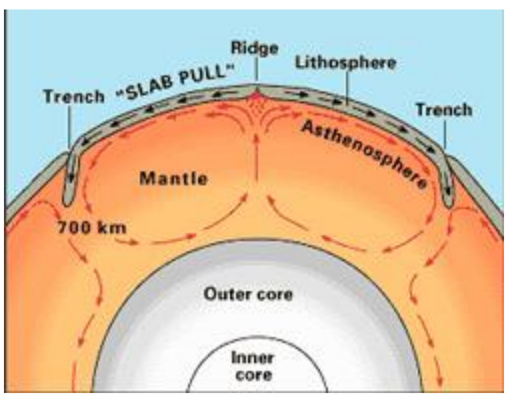

Plate Actions

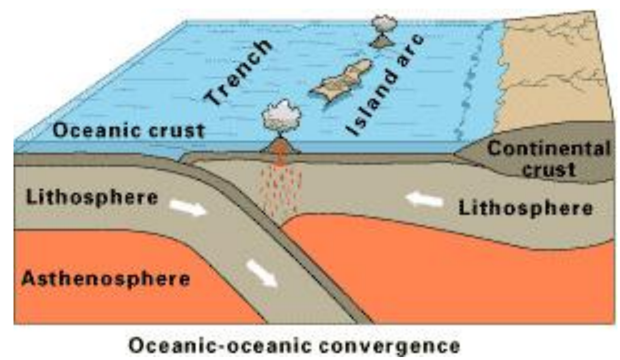

Ocean-Ocean Convergence

Electromagnetic Spectrum from SLF - ULF – Visible - UV

- Ionospher & ULF/ELF Signatures: Green & Hattori postulates

- Vision in Optical Spectral Window: Planck’s law

- HF Ground-Penetrating Radar and SAR

Vector (Polarization) Electromagnetic Spectrum

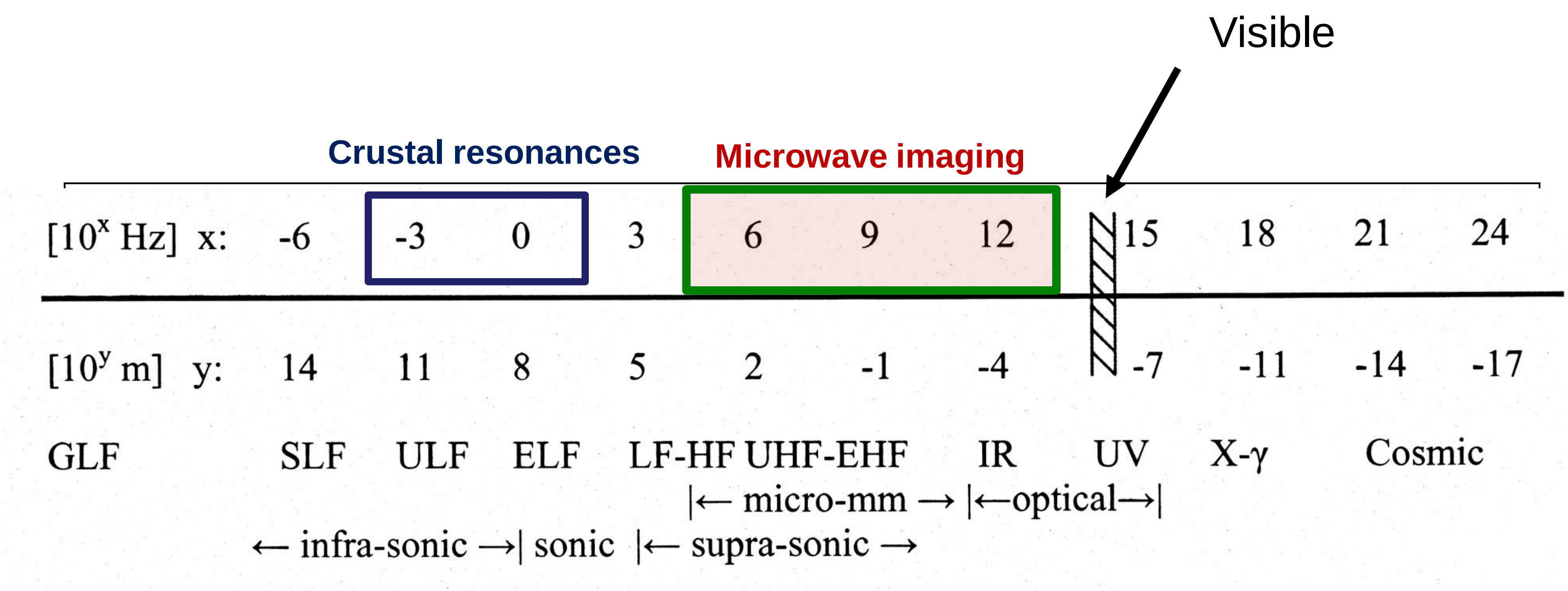

Vision in optical window

- Planck's Law

  Max Planck * ,

  Discovered reason why terrestrial creatures make use of one and the same optical spectrum from interpretation of his radiation law:

$$S_{of}^{*} = \frac{2h}{c^2} f^3 \left(e^{\frac{h \cdot f}{k \cdot T}} - 1 \right)^{-1}$$

MW-Bereich: hf << kT
Näherung von Rayleigh-Jeans

$$S_{of}^{*} = \frac{2kT}{c^2} f^2$$

α = Absorptionsvermögen ≤ 1

$$S_{0f} = \alpha \, S_{of}^{*}$$

S_{0f}= Spektrale Leistungsdichte

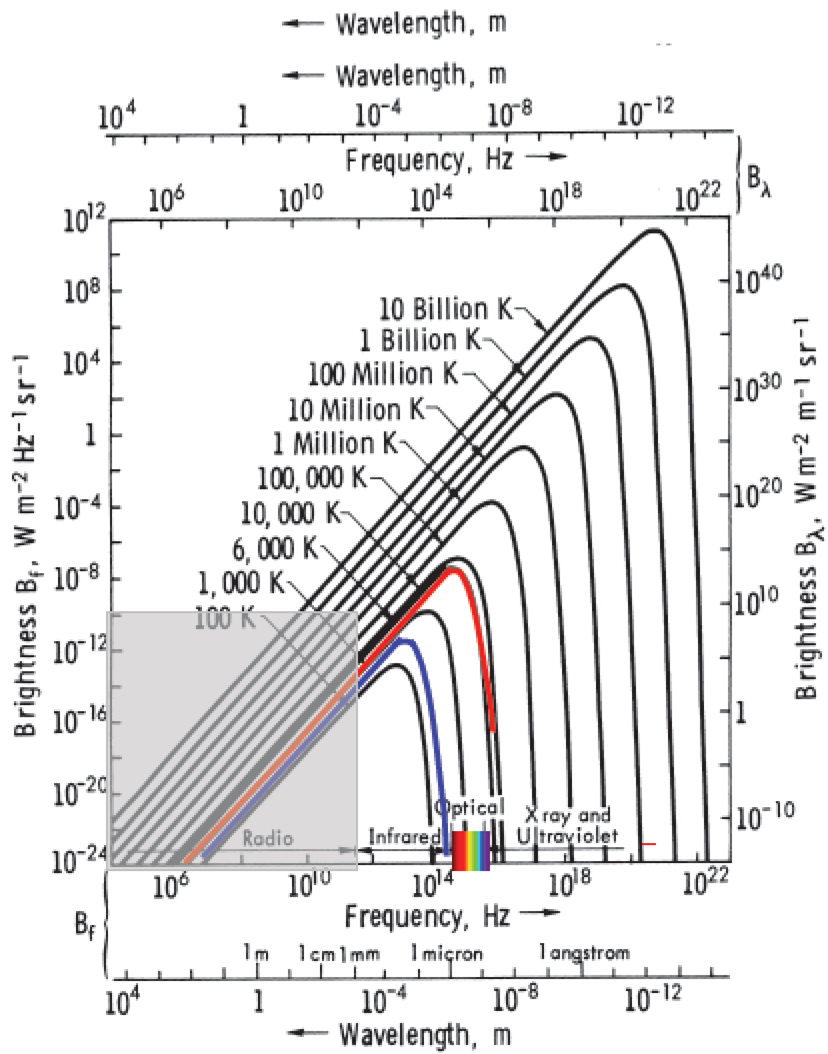

Deutsches Zentrum für Luft- und Raumfahrt e.V.
in der Helmholtz-Gemeinschaft
DLR

Microwaves and Radar Institute, Wolfgang Keydel

Planksches Strahlungsgesetz

Transmission Spectrum of Atmosphere

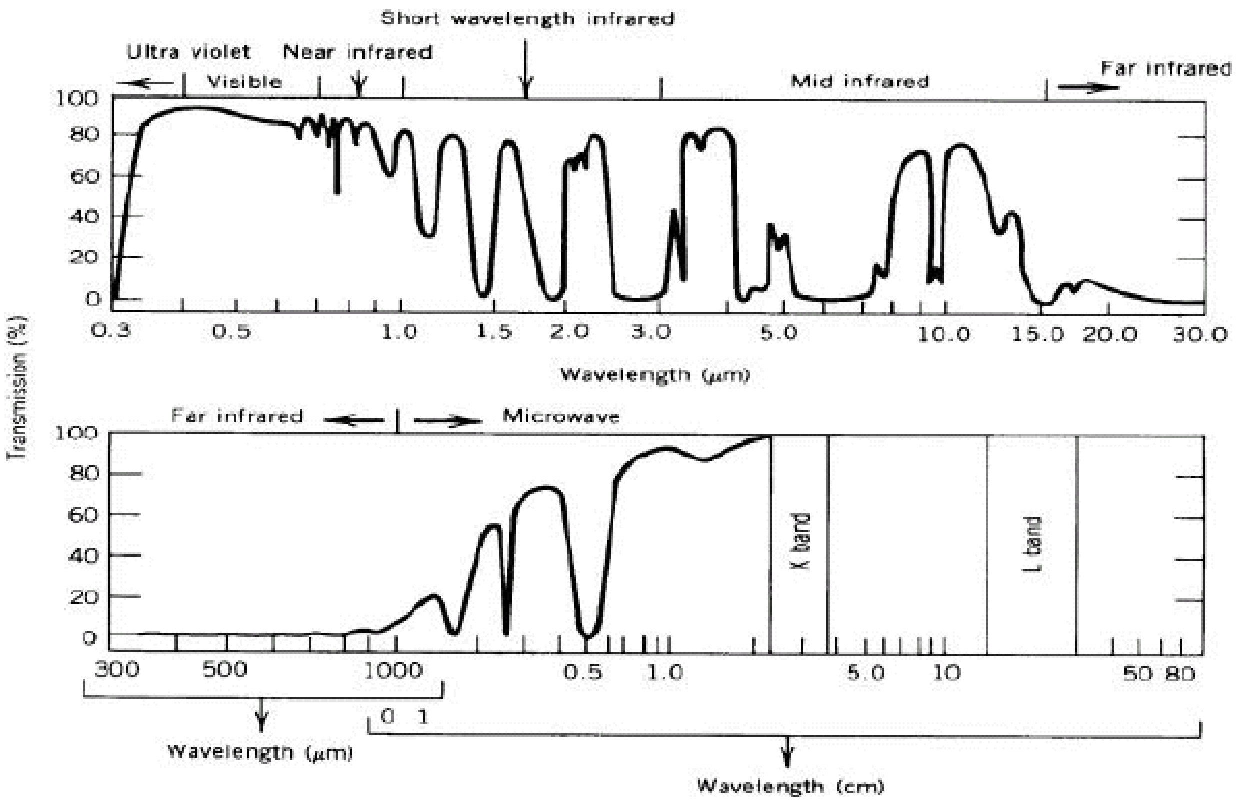

Ionospher & ULF/ELF Signatures:

- Schumann resonances
- Green postulates
- Hattori postulates

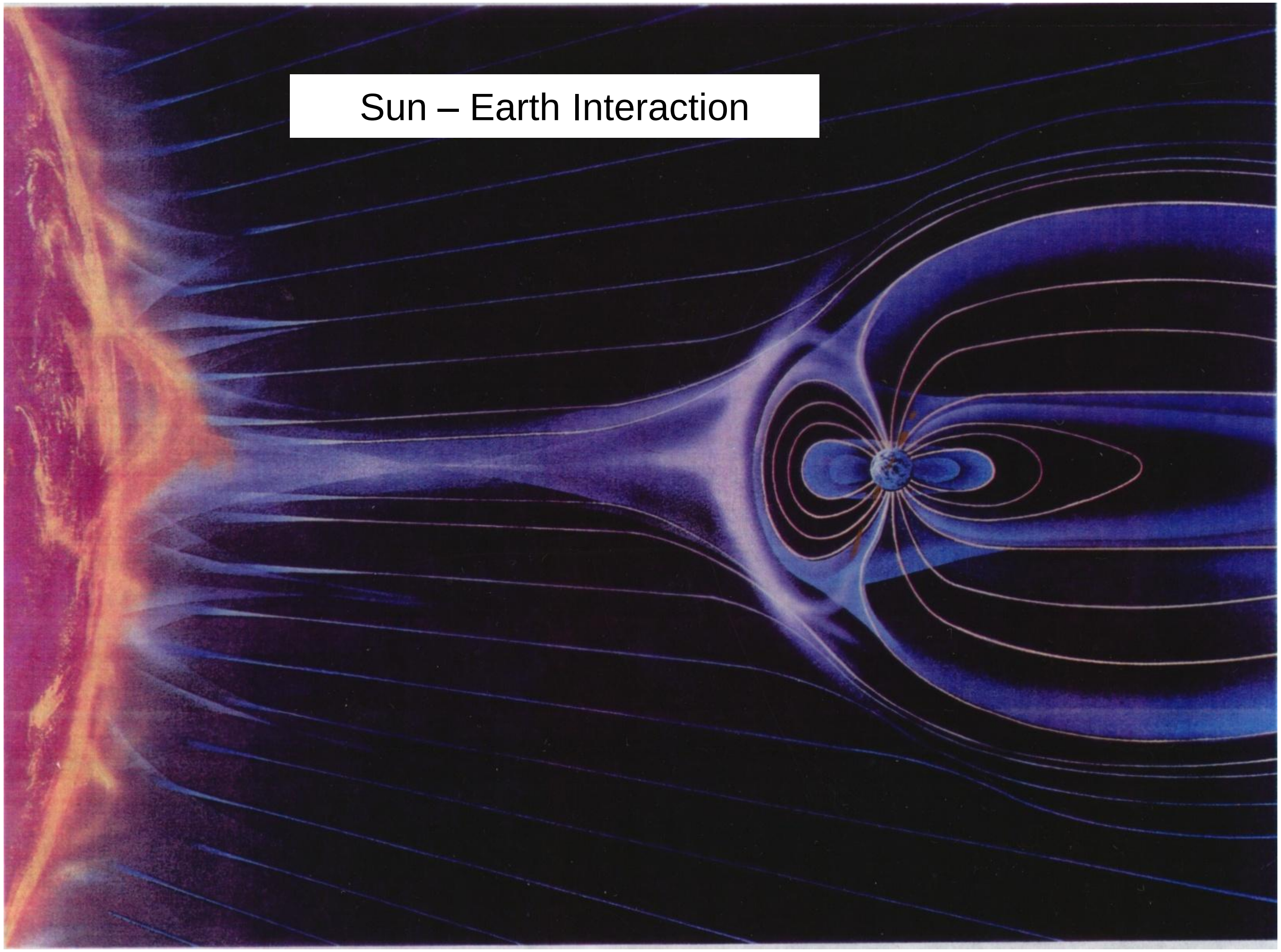
Sun – Earth Interaction

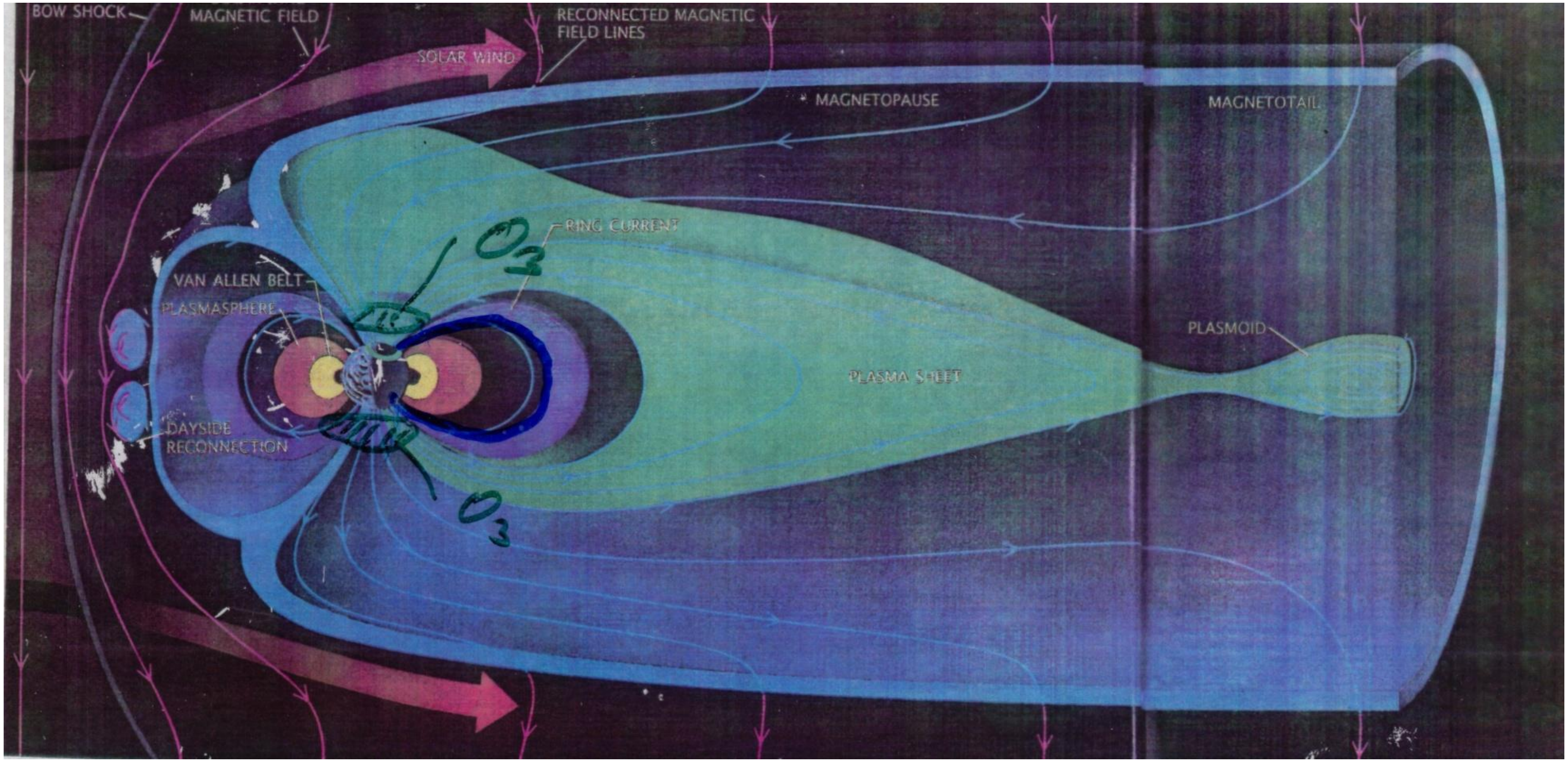

Terrestrial Ionosphere & Magnetosphere

ELF/ULF Electromagnetic Spectrum

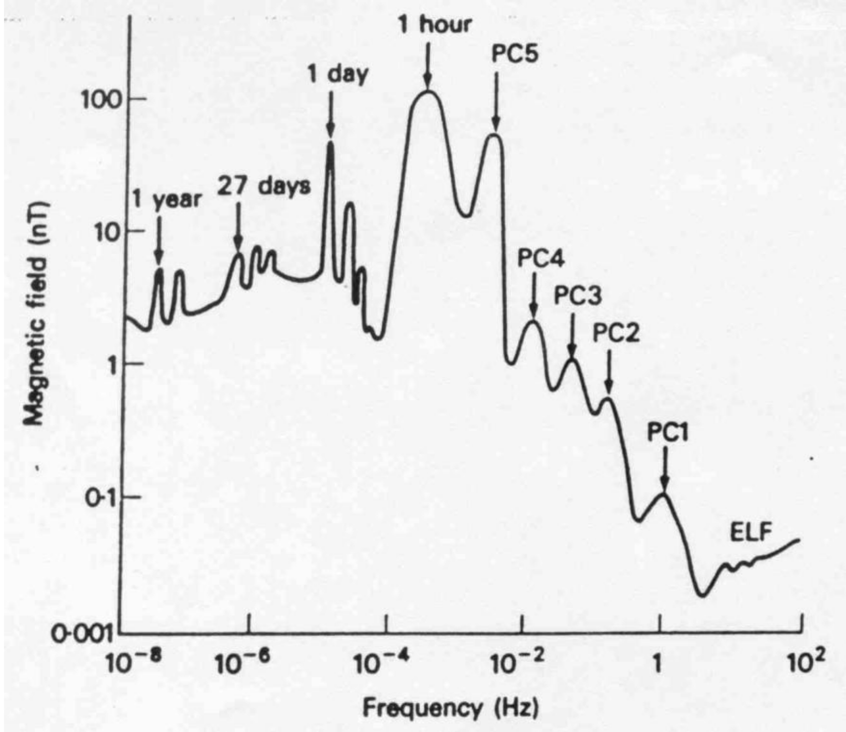

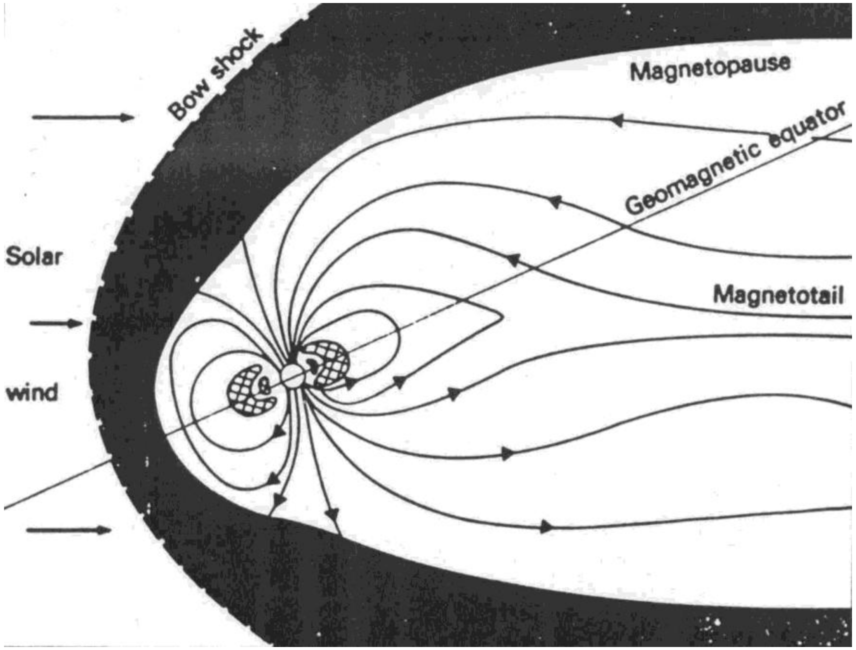

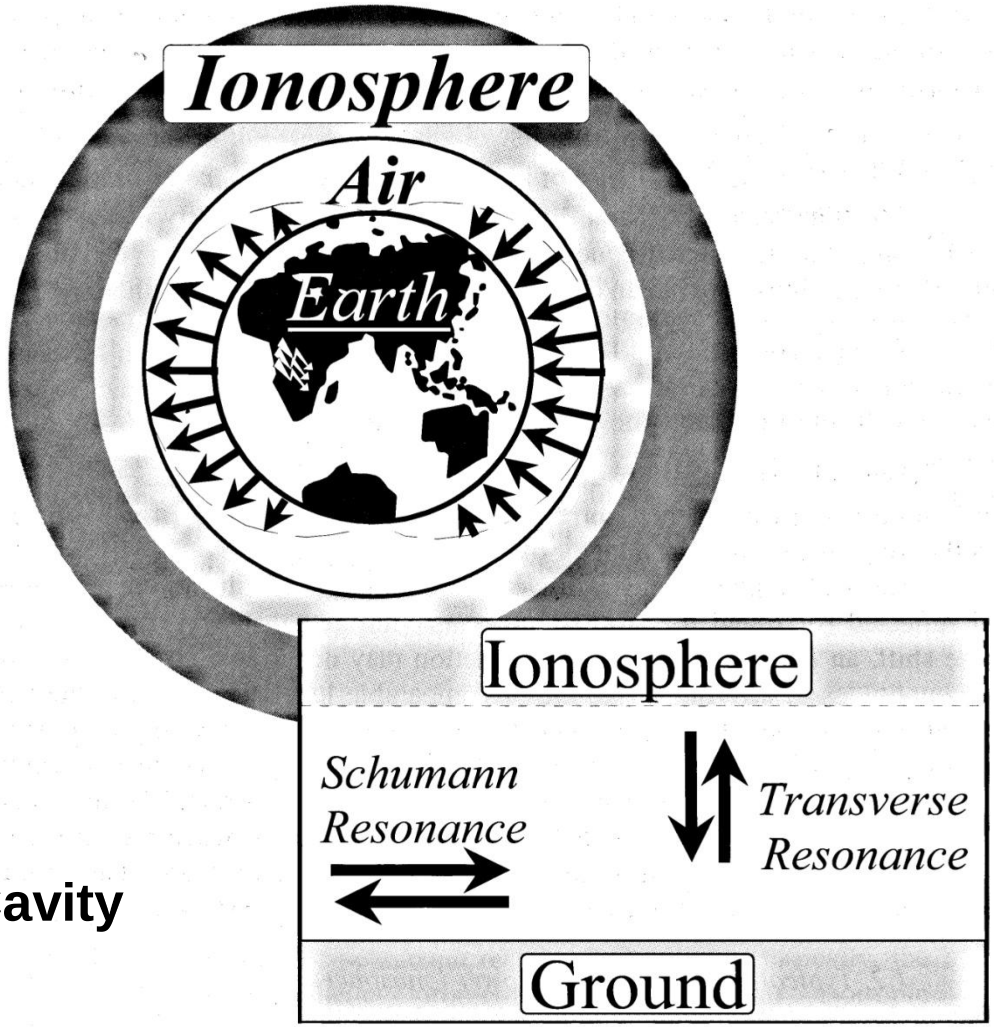

Earth-Ionosphere Cavity

Schumann resonance

- Basic Resonance of Earth-Ionosphere Cavity
- Excited by Electric Storm Discharges: Lightening
- Approximate fundamental resonance length:
- Circumferential length at ~ 4km above earth surface $\mathbf{L_s}$
- Basic Resonance frequency: f_{so} = $\mathbf{L_s / c \sim 8.6\ Hz}$
- Because Earth-Ionosphere cavity is not perfectly con-spherical, a complete eigen-frequency calculation was developed by Winfried Otto Schumann (1988 – 1974) of which the first three eigen-frequencies are pertinent:
- f_{So} **= 8.6 Hz,** f_{S1} **= 14.1 Hz,** f_{S2} **= 21.4 Hz,** : f_{S3} **= 28.7 Hz, ...**

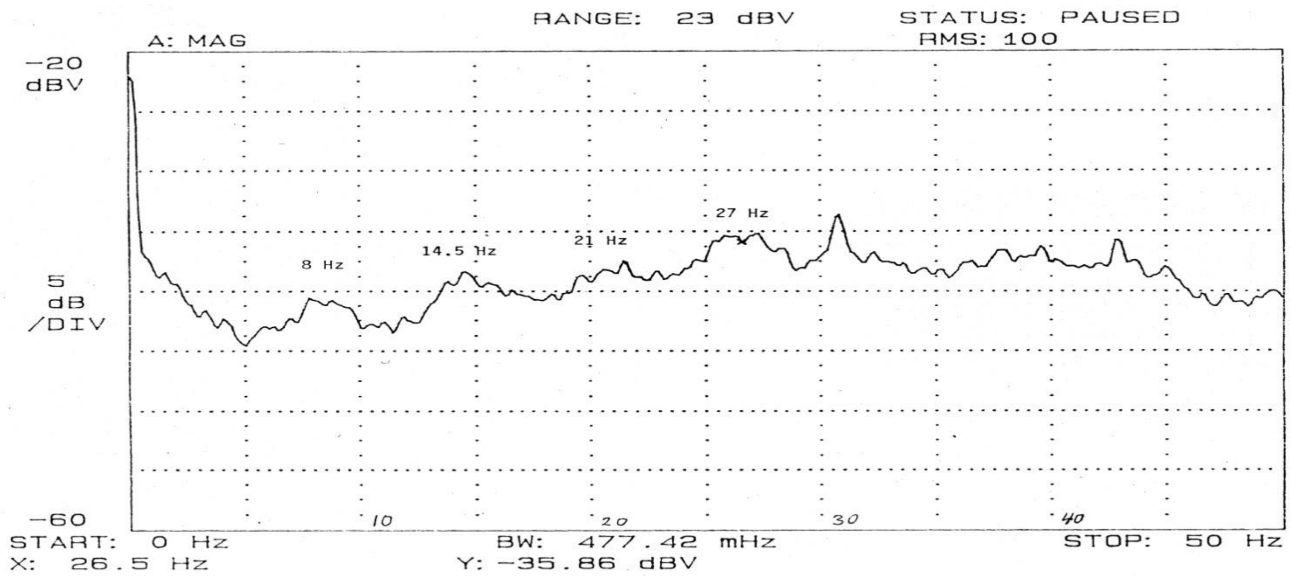

Schumann Spherics (Electric Storm) Signatures

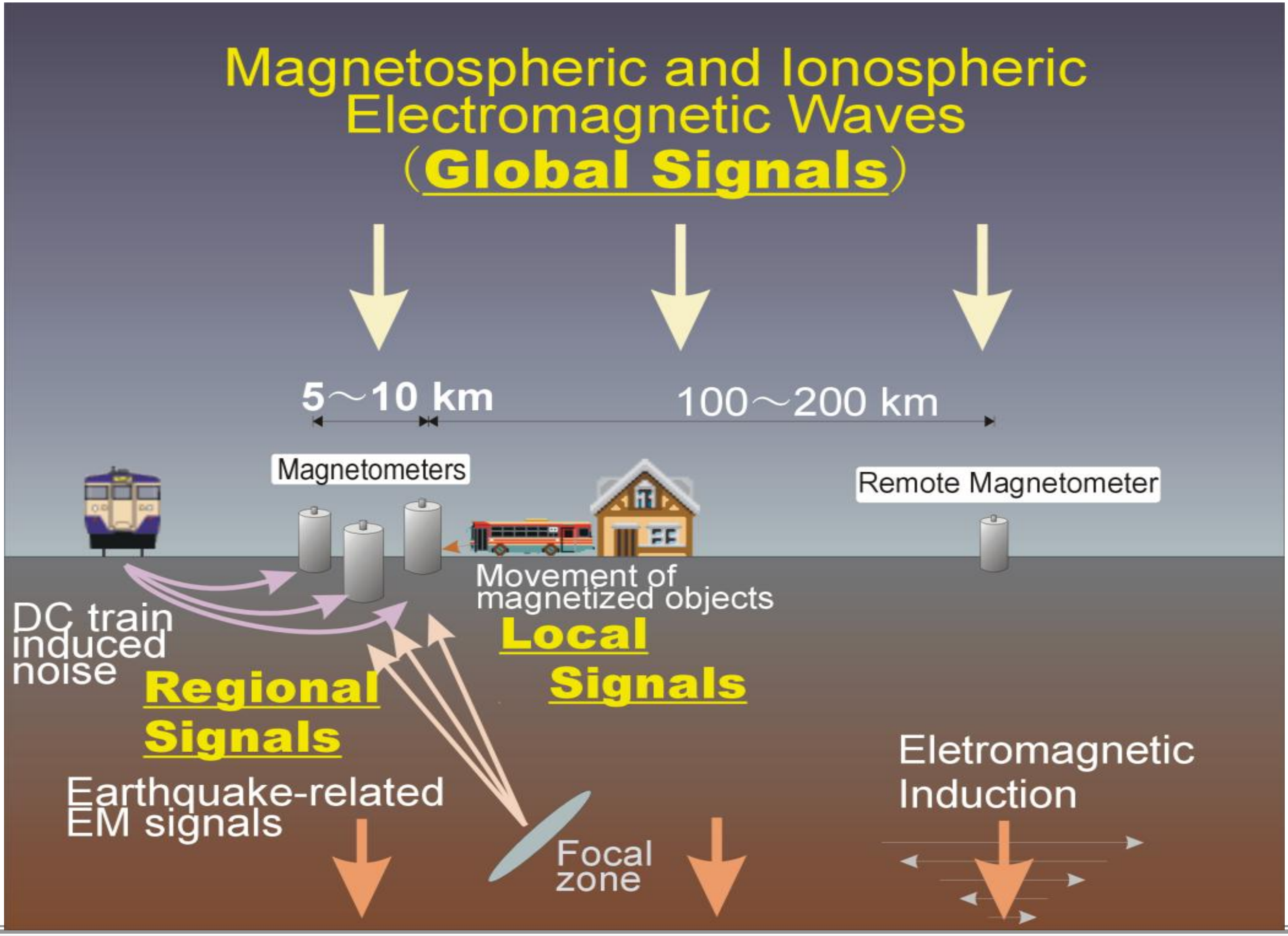
Magnetospheric and Ionospheric
Electromagnetic Waves
(Global Signals)
5～10 km
100～200 km
Magnetometers
Remote Magnetometer
Movement of
magnetized objects
Local
Signals
DC train
induced
noise
Regional
Signals
Earthquake-related
EM signals
Focal
zone
Eletromagnetic
Induction

Green postulate

- The 3 Hz minimum was suggested by Arthur William (Bill) Green, and utilized by Dr. Jack Dea at NOSC, Point Loma, San Diego first because man-made local disturbances had not been too prevalent, and the basic principles had been developed by him during early 1990ies at the sea-side USN-NOSC Laboratory

Green and Hattori postulates

- The Terrestrial eigen-frequency spectrum

possess among others, two specific natural resonances at 0.1 Hz and at 3 Hz which are utilized for detecting natural and also man-induced disturbances, known as the Hattori and the Green resonances for earth-quake pre-cursor detection, as demonstrated next

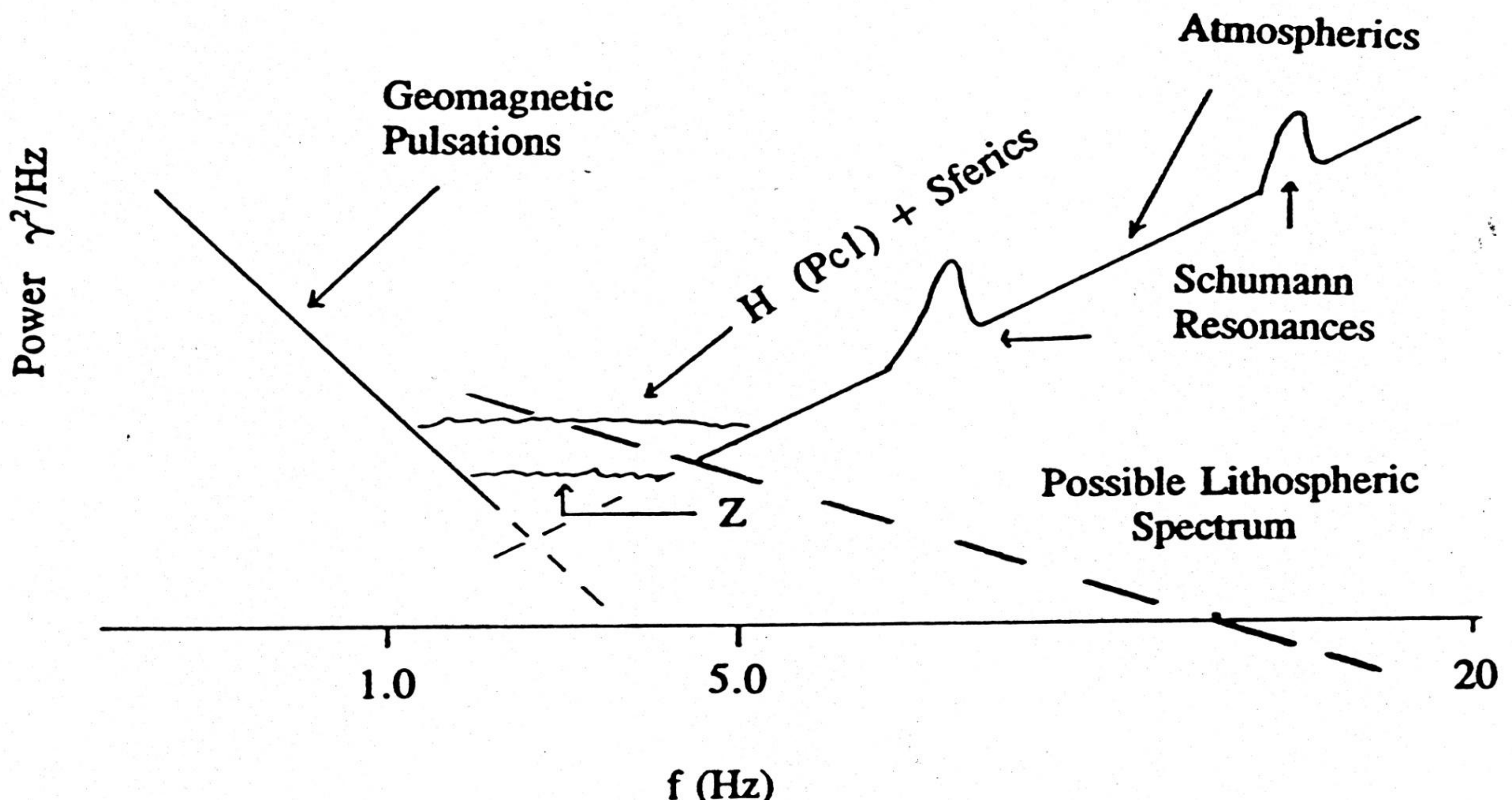

Green's Tectonic Stress Electromagnetic Signatures

Recent electromagnetic signatures associated with the Chi-Chi and Chia-Yi earthquakes of 1999.

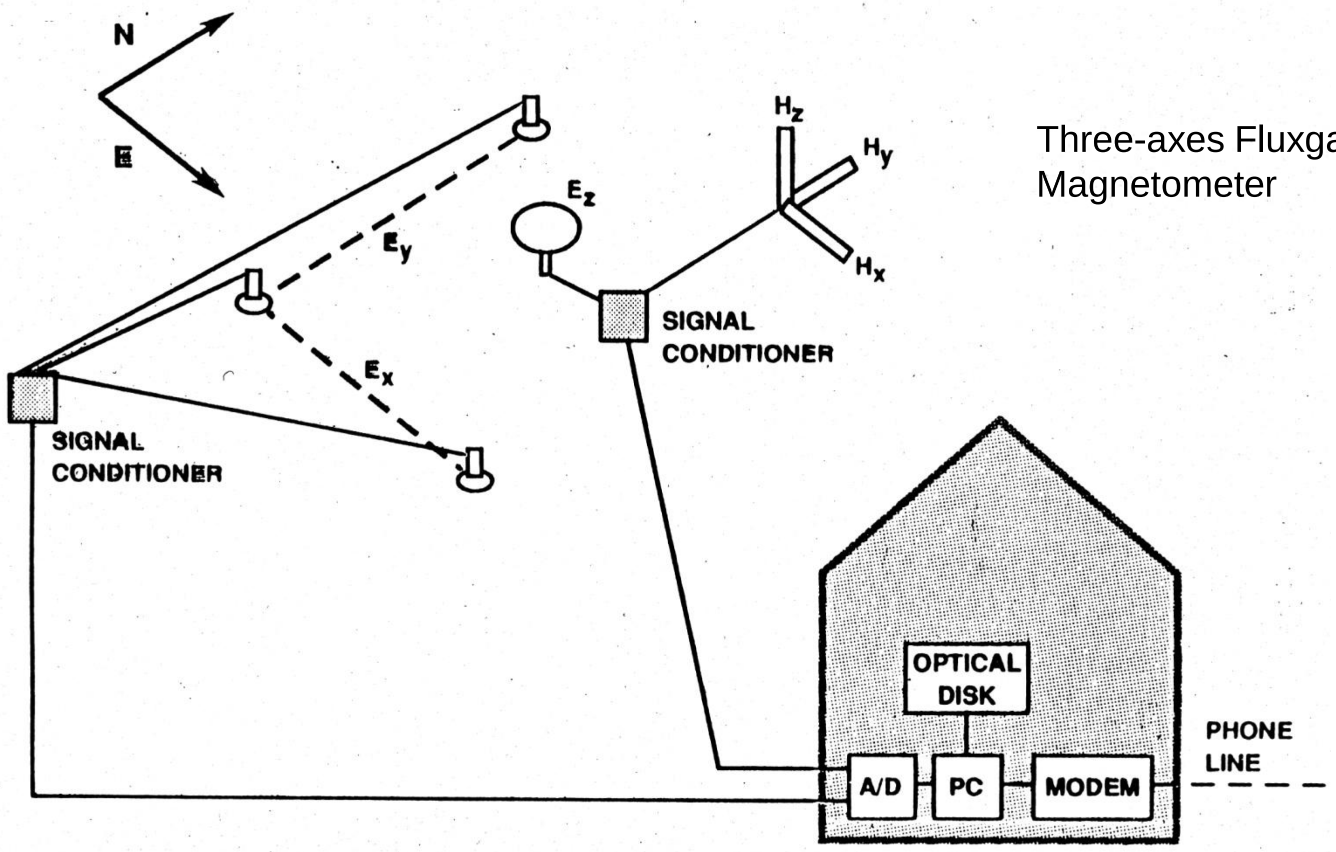

Three-axes Fluxgate Magnetometer

ULF Magnetometric & Electrometric Measurement Arrangement

Recent electromagnetic signatures associated with the Chi-Chi and Chia-Yi earthquakes of 1999.

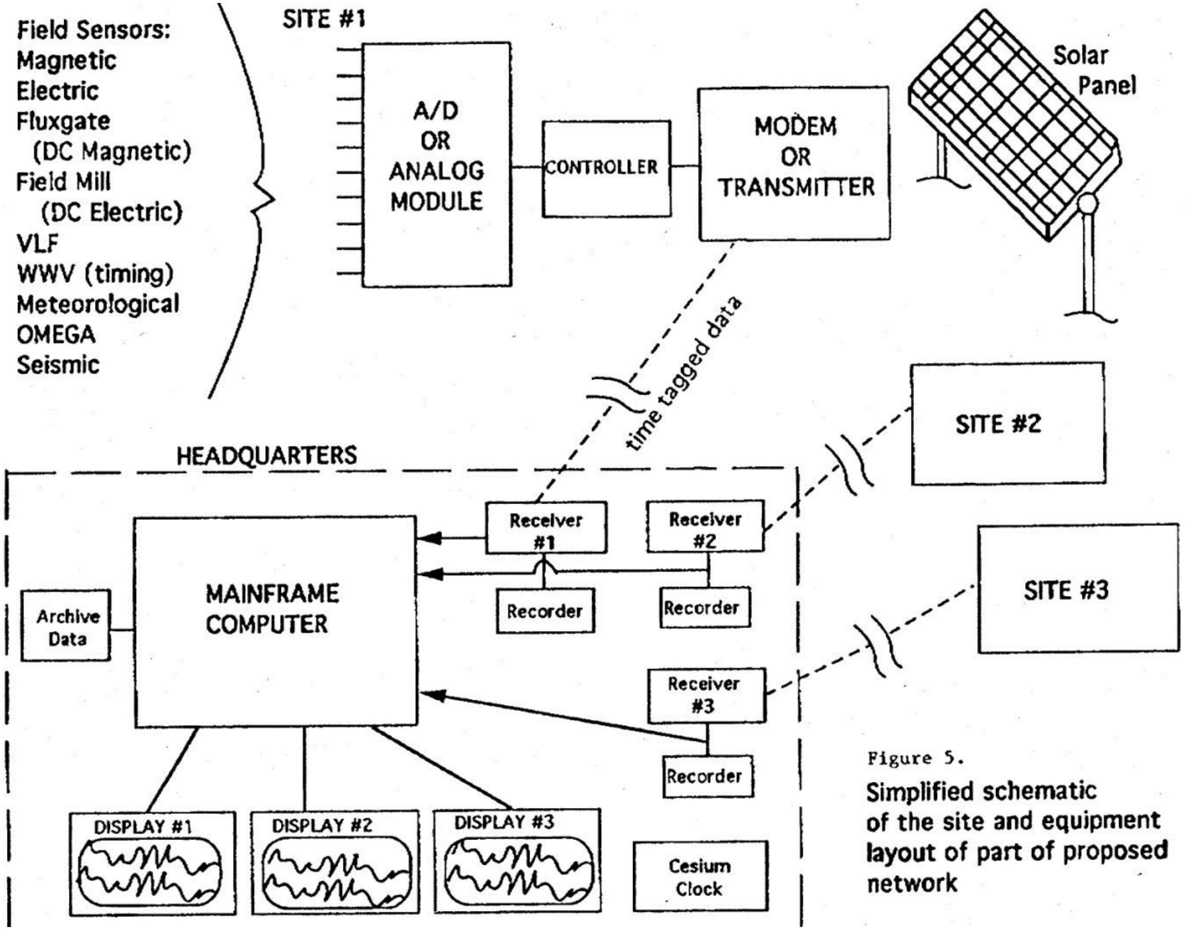

Figure 5.
Simplified schematic of the site and equipment layout of part of proposed network

Simplified Schematic of the Site and Equipment Layout

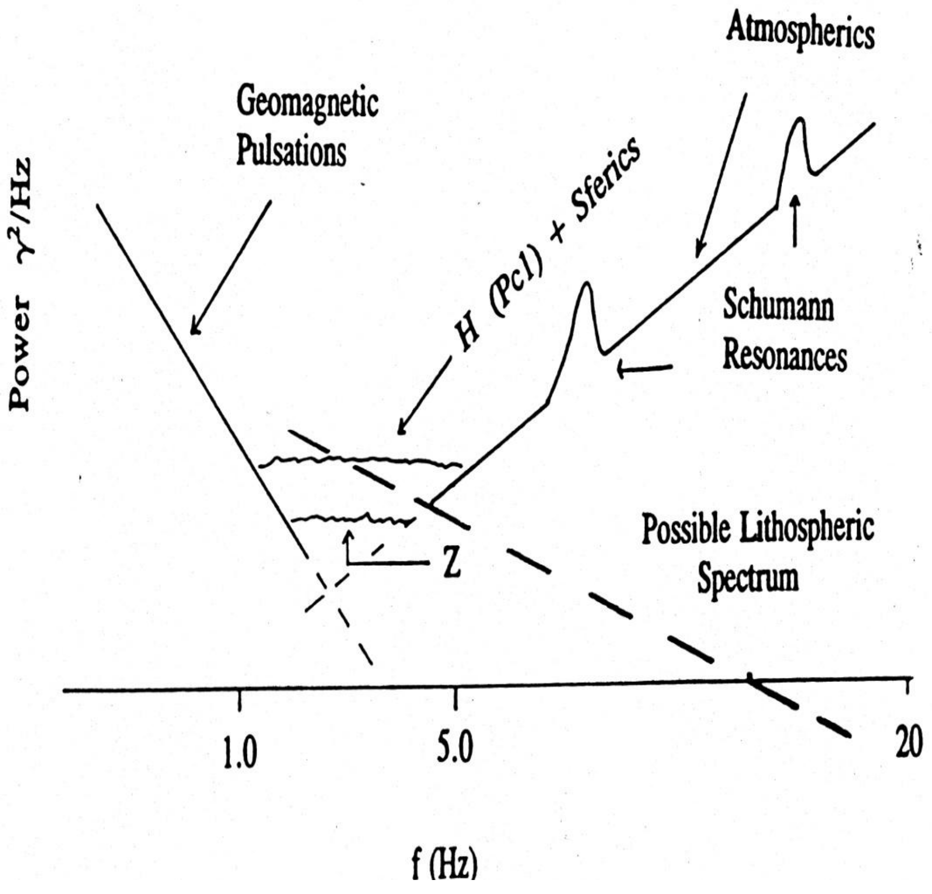

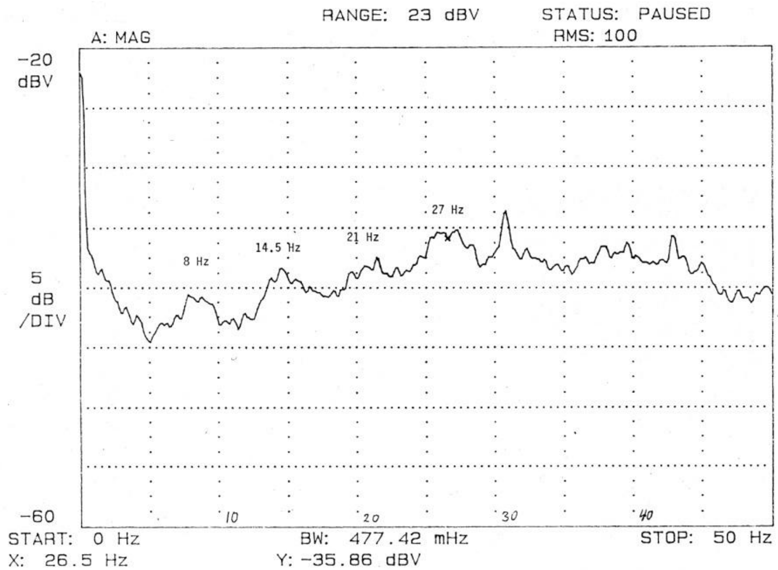

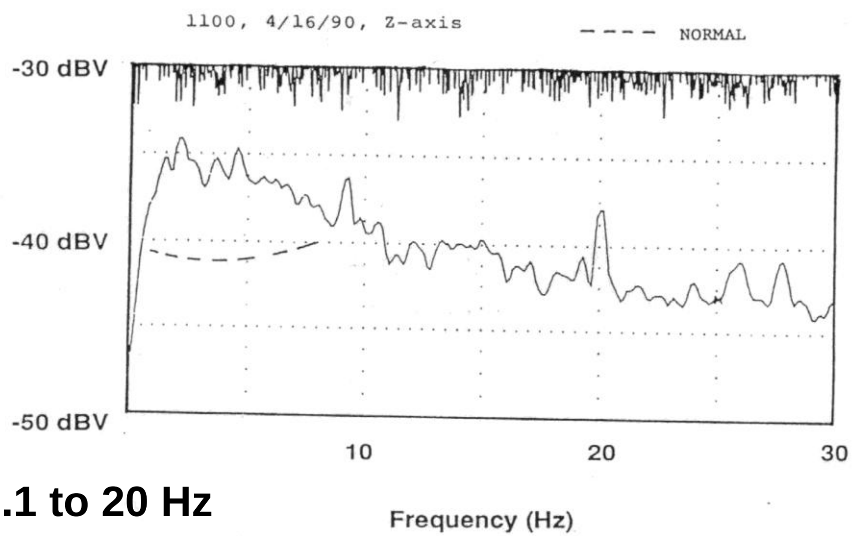

ULF Tectonic & Spherics Signatures at About .1 to 20 Hz

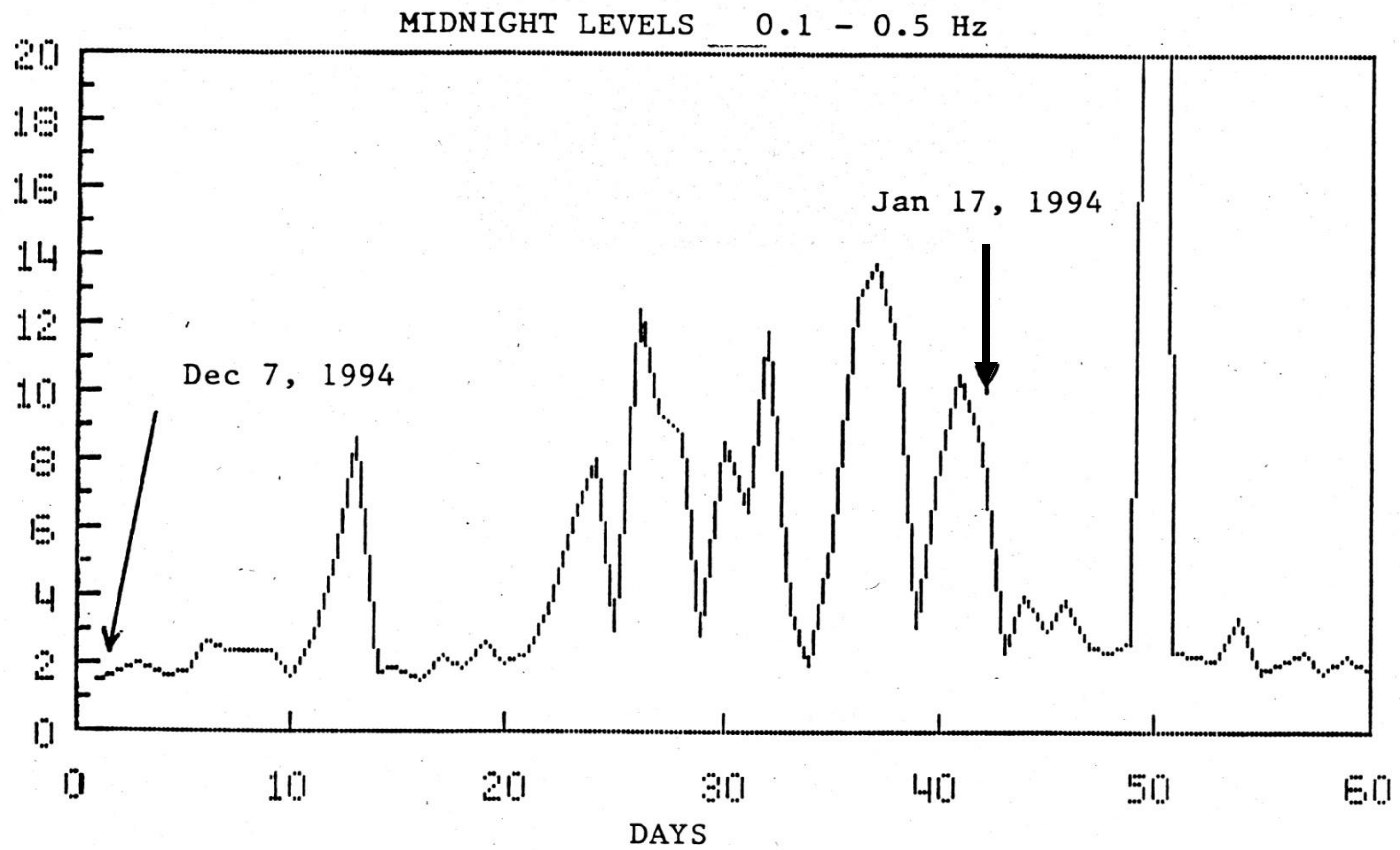

Averaged Tectonic Stress Signatures during Northridge Earthquake

Discrimination of seismo-magnetic signals

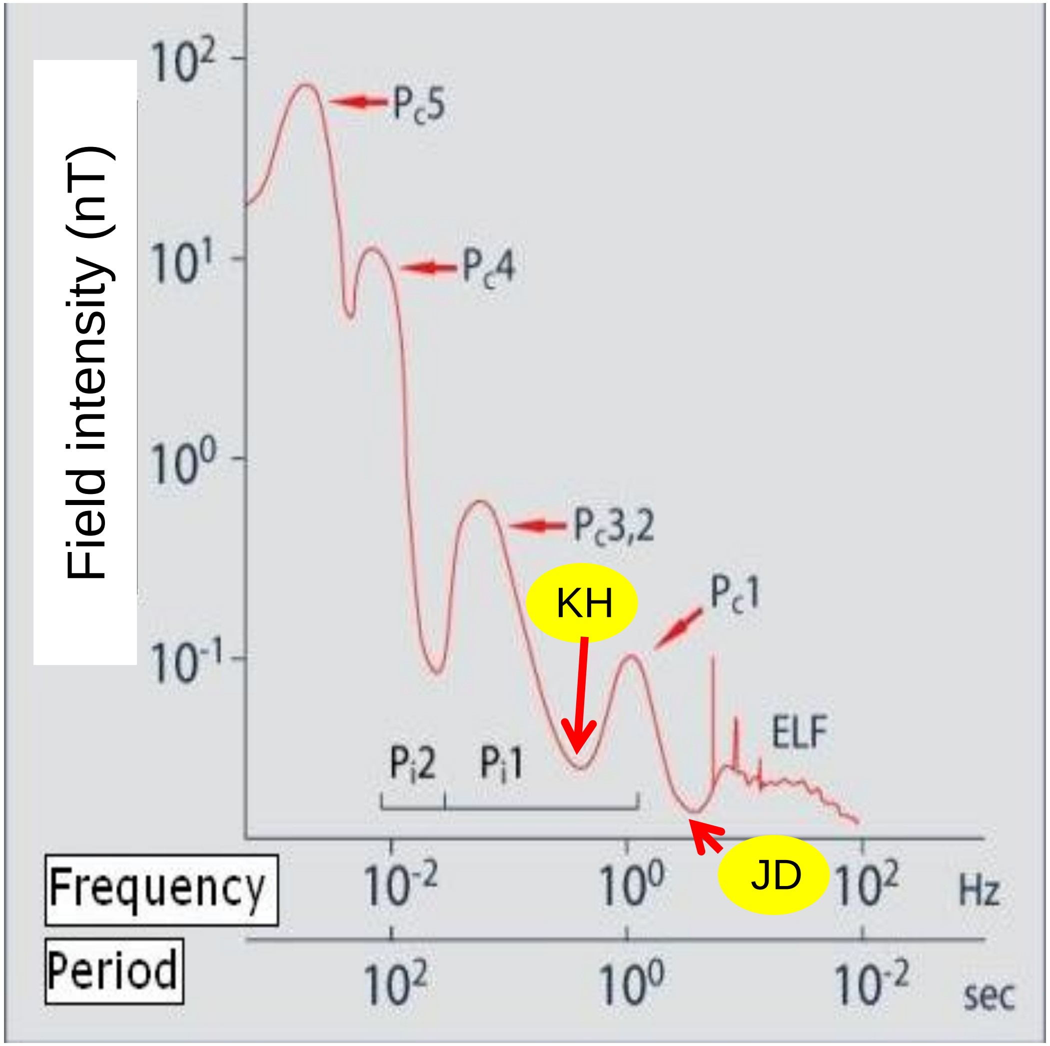

$$P = \frac{\lambda}{2\pi} = \frac{1}{2\pi}\sqrt{10\rho_{(\Omega.m)}.T_{(s)}}$$

Signals with short periods have small skin depths.

For nigthtime energy study, we focused on the 100 s (0.01 Hz) period which was one of the most frequently reported periods in previous studies.

Monitoring of ongoing surface deformation along Cheleng-Pu fault

Taiwan

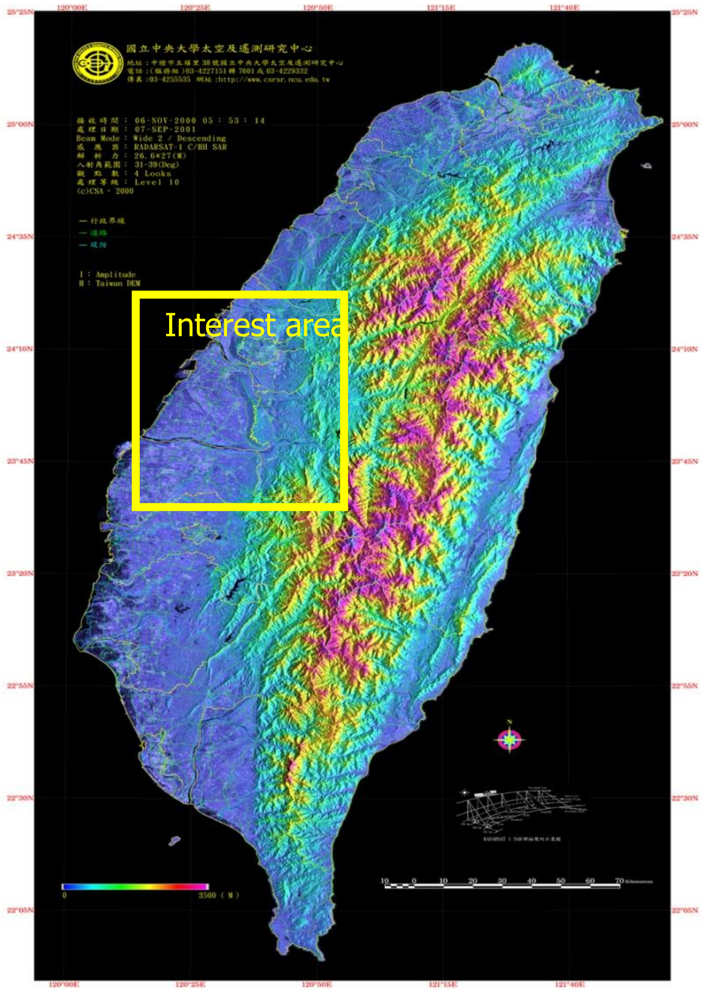

Data fusion of DEM and RADARSAT SAR images By CSRSR.

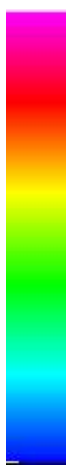

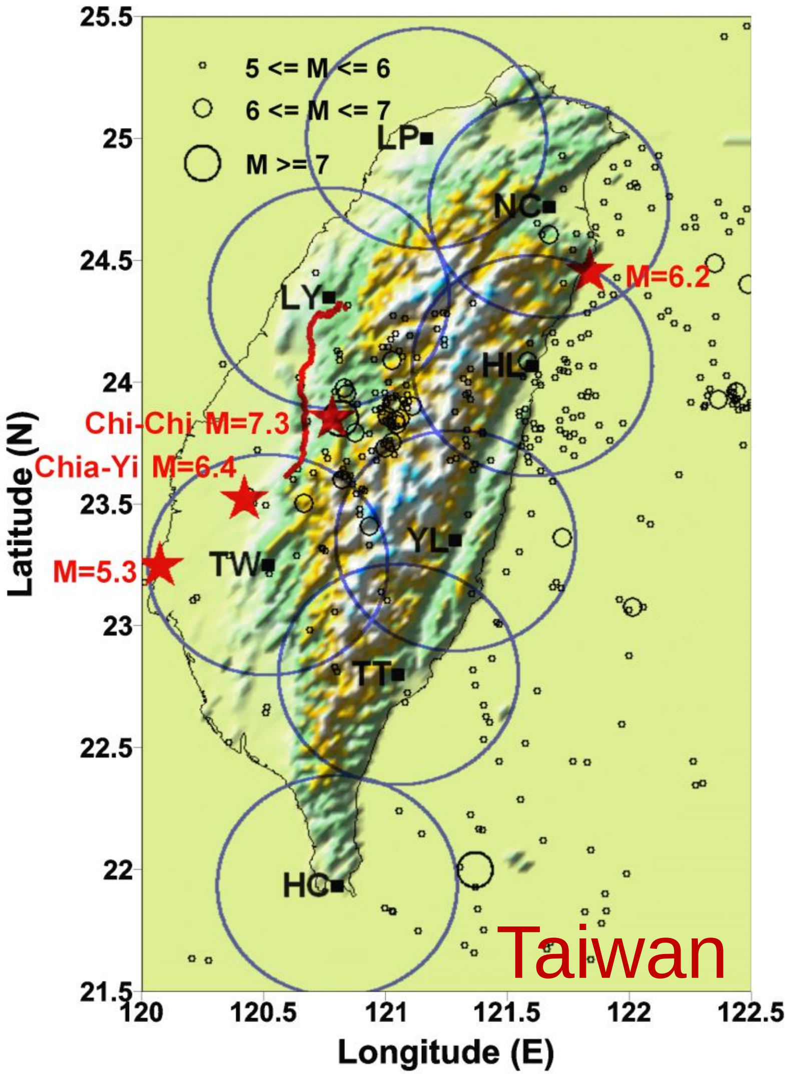

Earthquakes

- **Blue circle:**
  Radius 50 Km
- **Red line:**
  Chelungpu fault
- **Star mark: Three sample earthquakes**
- **Black circle: Earthquakes M >= 5.0**

Earthquakes occurred in six blue circles (except HC, LP) were compared with the anomaly

The Western Pacific Rim of the Circum Pacific Rim and Taiwan

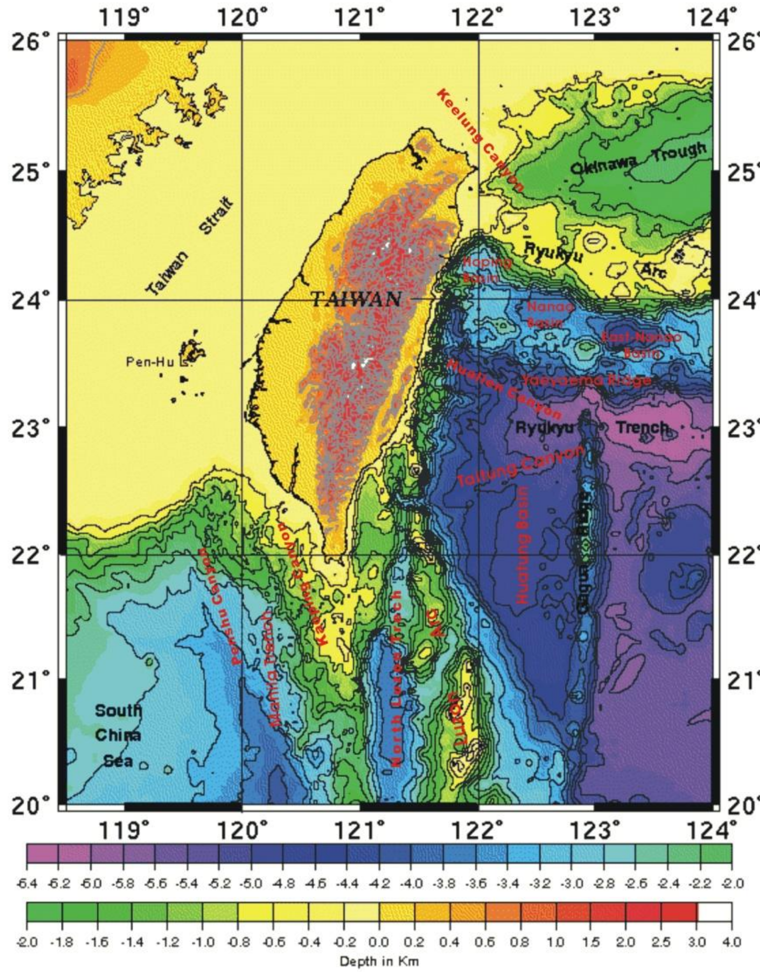

The Western Pacific Rim of the Circum Pacific Rim and Taiwan

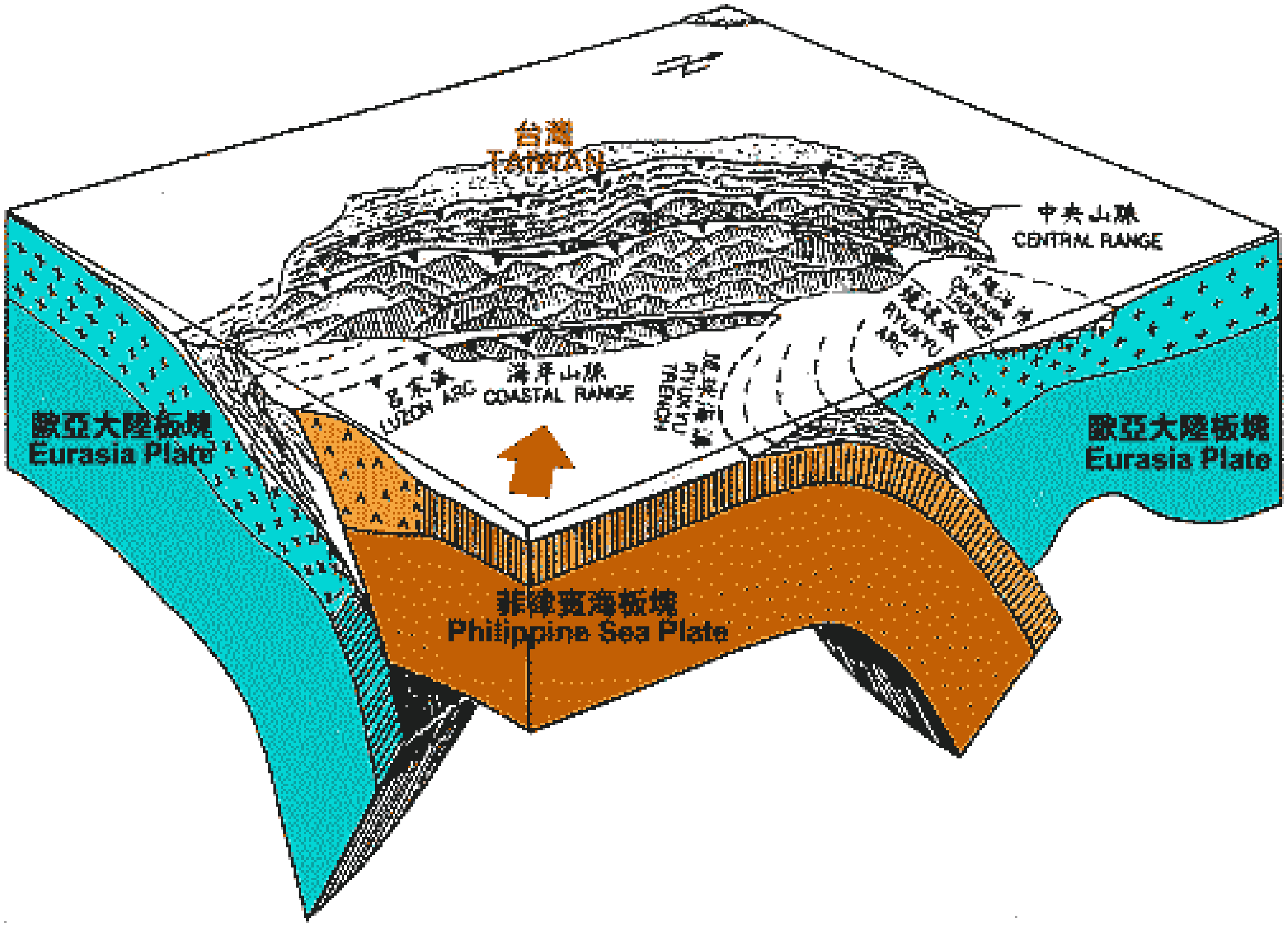

From gis.geo.ncu.edu.tw/921

The Western Pacific Rim of the Circum Pacific Rim and Taiwan

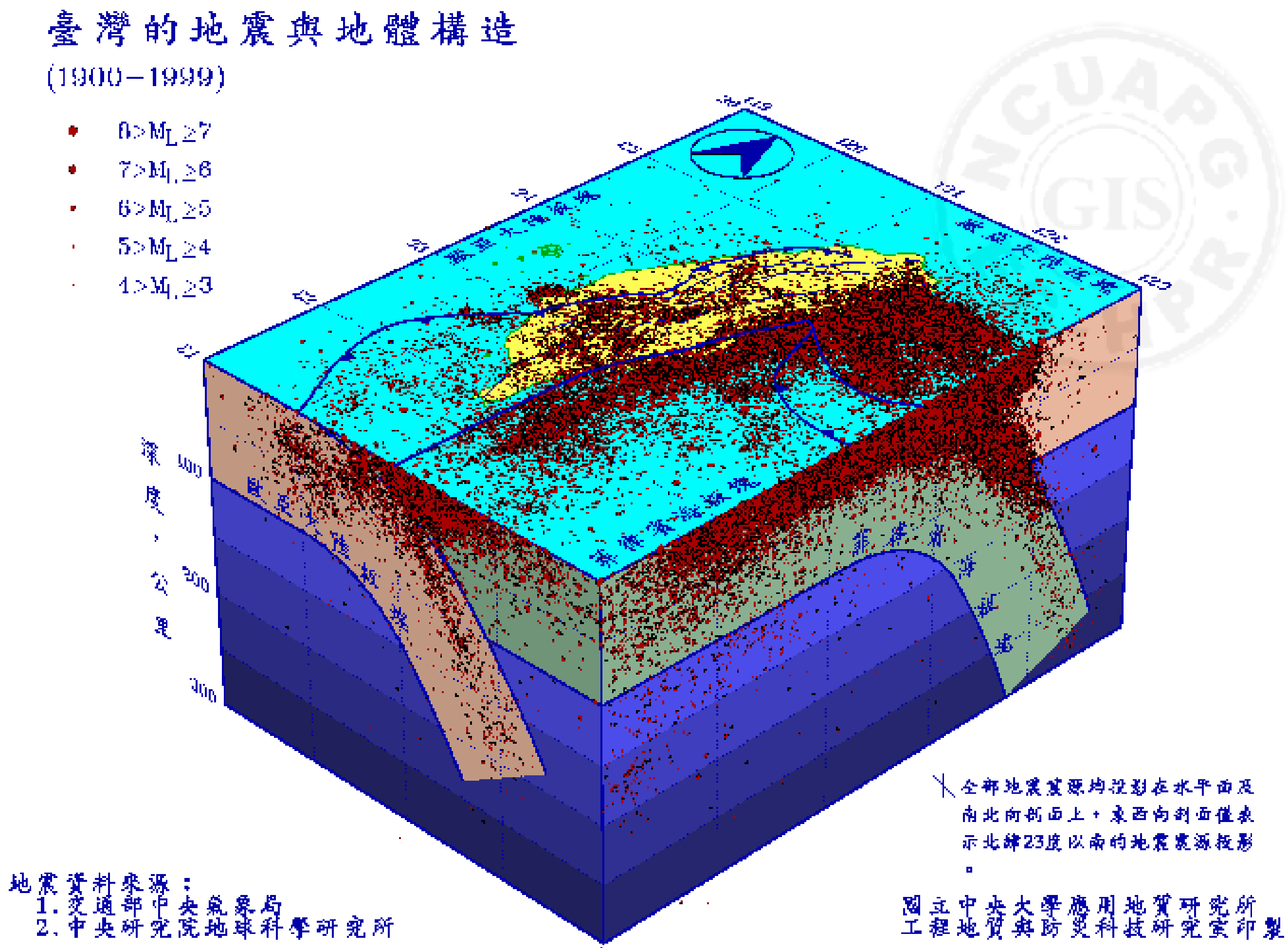

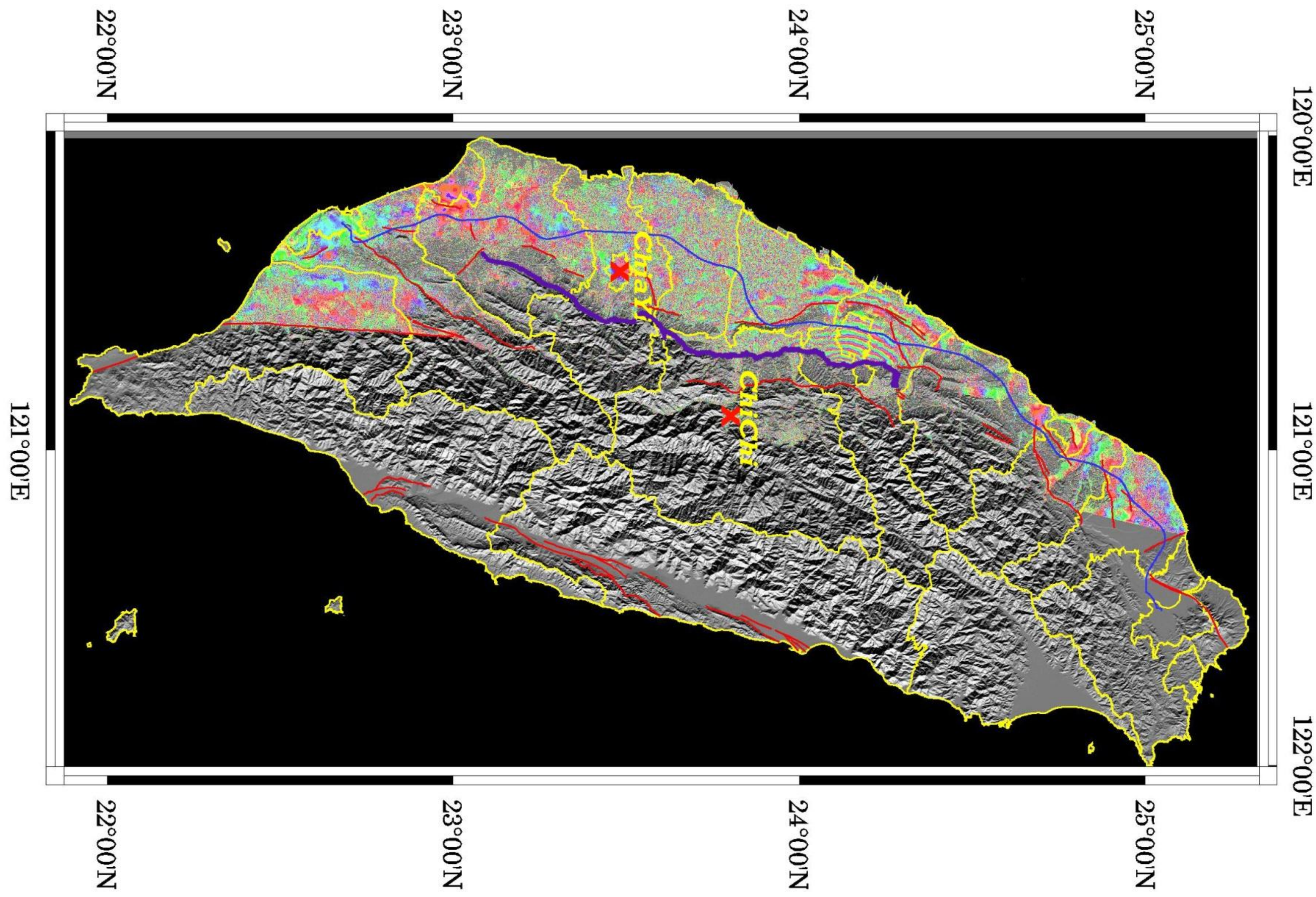
22°00'N
23°00'N
24°00'N
25°00'N
120°00'E
121°00'E
122°00'E
ChiaYi
ChiChi

The destruction along the Cheleng-Pu fault caused by the Chi-Chi earthquake of 1999 September 21

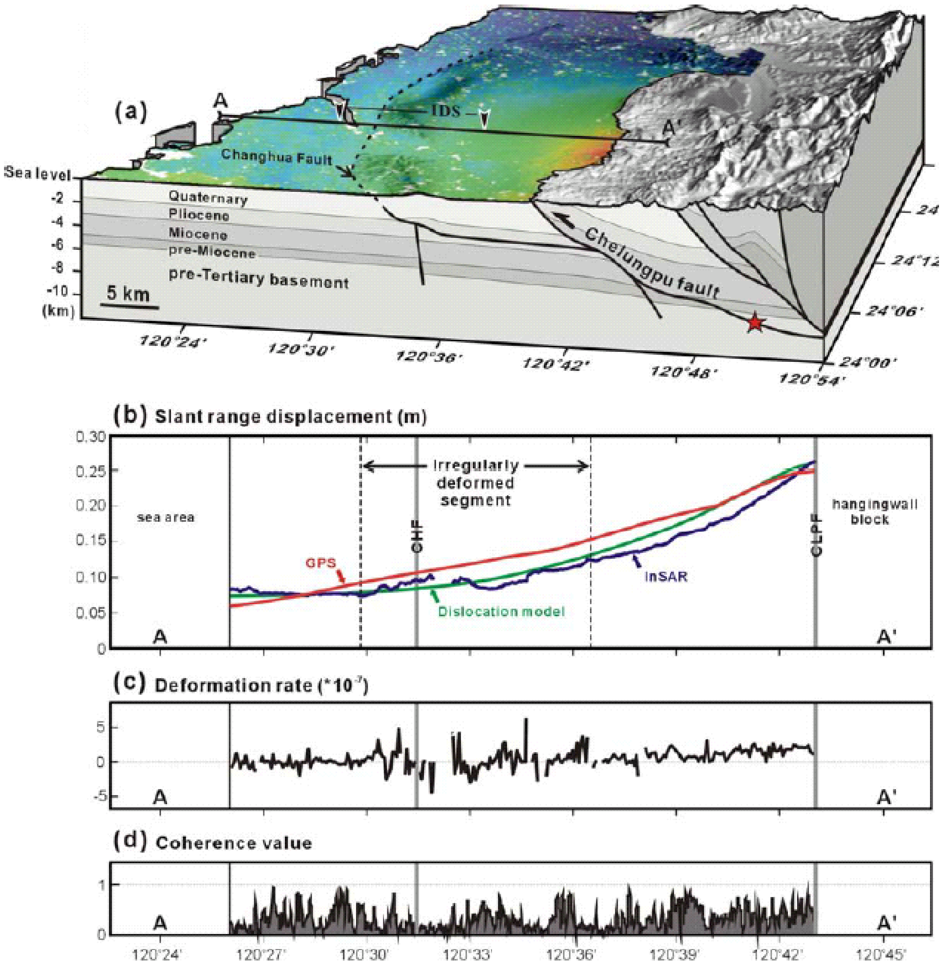

Recent electromagnetic signatures associated with the Chi-Chi and Chia-Yi earthquakes of 1999, May to December in Taiwan

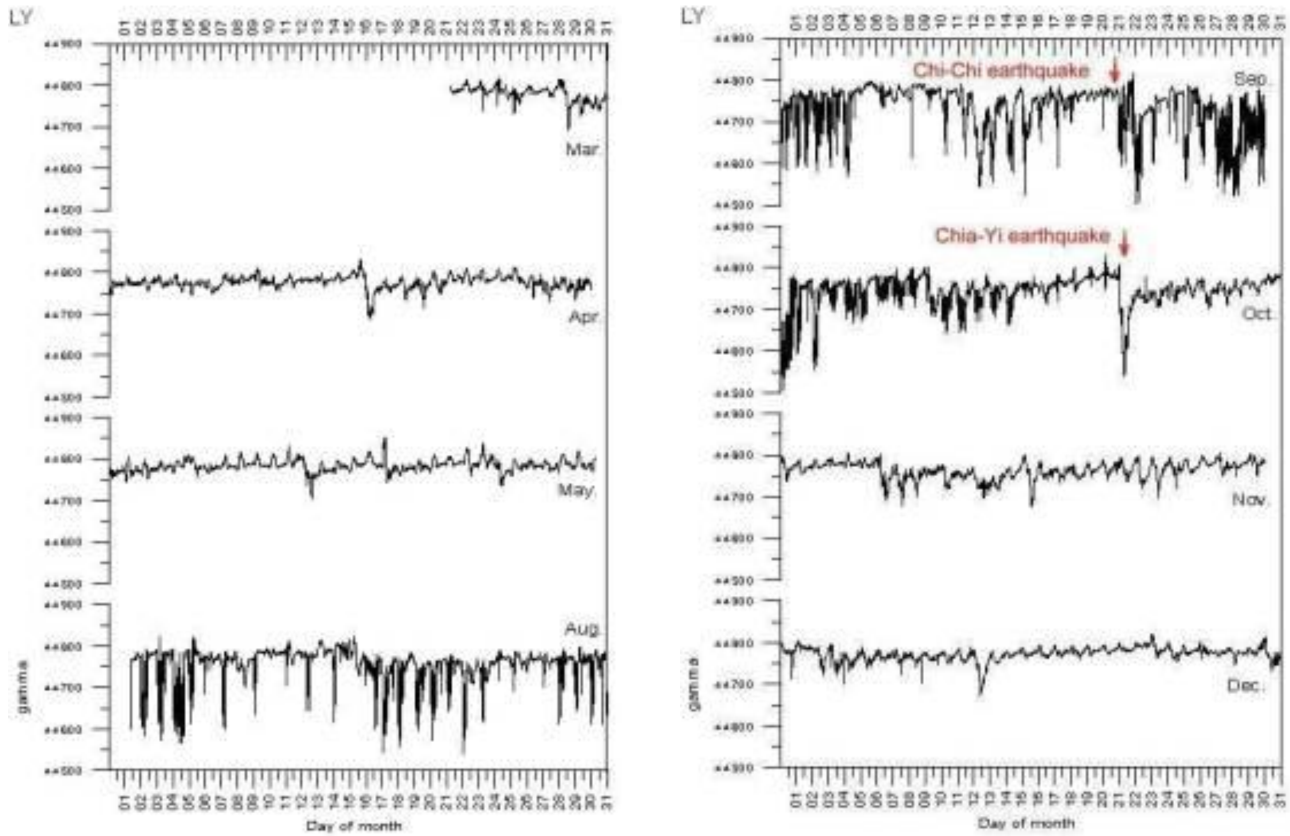

The raw data in LY station in March, April May, August, September, October, November and December, 1999.

Recent electromagnetic signatures associated with the Chi-Chi and Chia-Yi earthquakes of 1999.

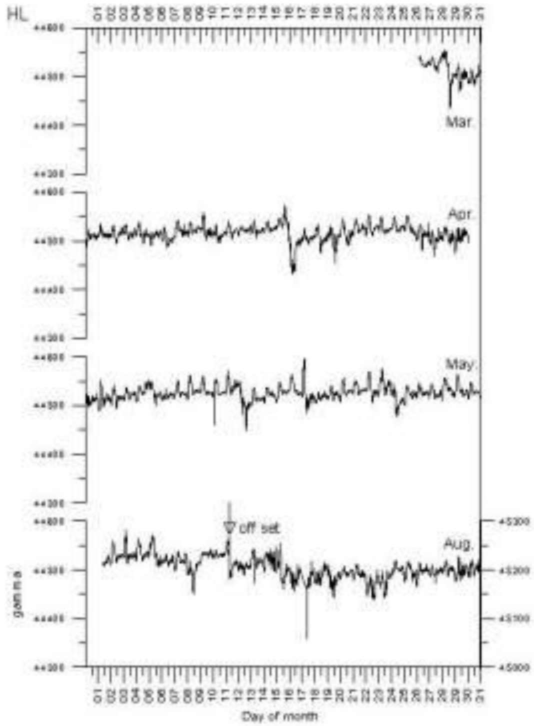

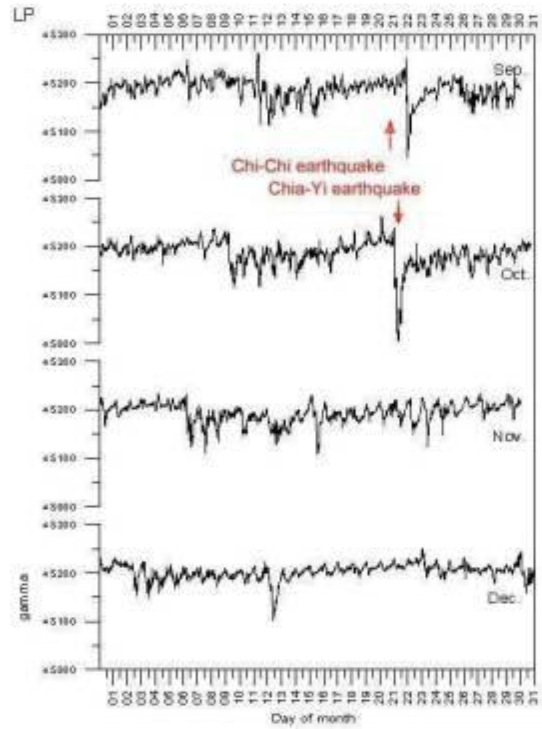

The raw data in HL and LP in March, April May, August, September, October, November and December, 1999.

Monitoring of ongoing surface deformation along Cheleng-Pu fault

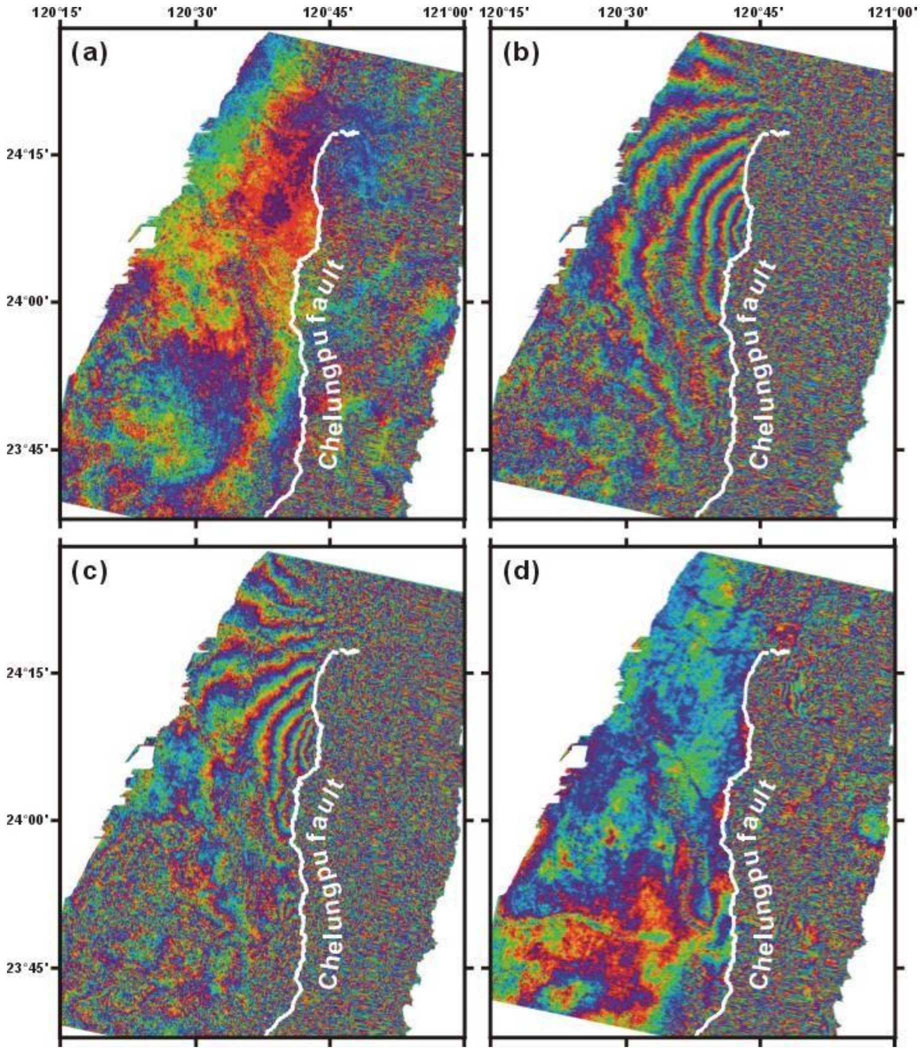

The destruction along the Cheleng-Pu fault caused by the Chi-Chi earthquake of 1999 September 21

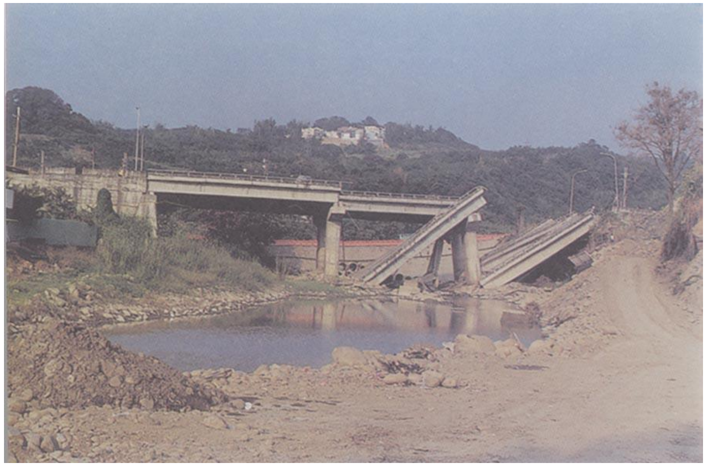

The destruction along the Cheleng-Pu fault caused by the Chi-Chi earthquake of 1999 September 21

PART-II, Microwave Polarization Radar & Polarimetric SAR

4. The Electromagnetic Microwave Spectrum & Signatures over land & ocean
5. Background on Polarization Radar Theory & Scattering Matrix Acquisition
6. Polarimetric Airborne SAR Sensors
7. Satellite POLSAR sensors
8. Scattering matrix decomposition theories and algorithms\

The Microwave Spectrum & Signatures

- Electromagnetic Environment

- Resonant signatures over land & ocean

Multi-Altitude Near-Range and Remote Sensing in Wide-Area Environmental Surveillance for Real Time Monitoring of the Earth's Biosphere

for an ecological investigation of the Earth through observation and identification of harmful anthropogenic influences due to the interaction of:

- Oceans ⟷ Atmosphere/Stratosphere/Mesosphere

Biosphere (Water)

81 << ε(f) >> 1

Hydrosphere

$$v_r = \frac{v_c}{\sqrt{\varepsilon_r}}$$

$$v_c \approx 3\times 10^8 [m/s]$$

$$\eta_r = \frac{\eta_0}{\sqrt{\varepsilon_r}}$$

$$\eta_0 = 120\pi [\Omega]$$

- **for an early warning system of natural and man-made environmental catastrophes and to take quick actions to buffer the impact to the catastrophe under the increasing pressures of a relentlessly un-abating population explosion:**

Severe weather	⟷	**Typhoons**
Earthquakes	⟷	**Volcanic Eruptions**

☆ **Global Weather Changes**

Degeneration into steppe	⟷	**Retreating Glaciers**
Pollution of Ground Water	⟷	**Pollution of Air**

☆ **Destruction of the Biosphere**

Hydrologic cycle with volcanologic & seismic activity

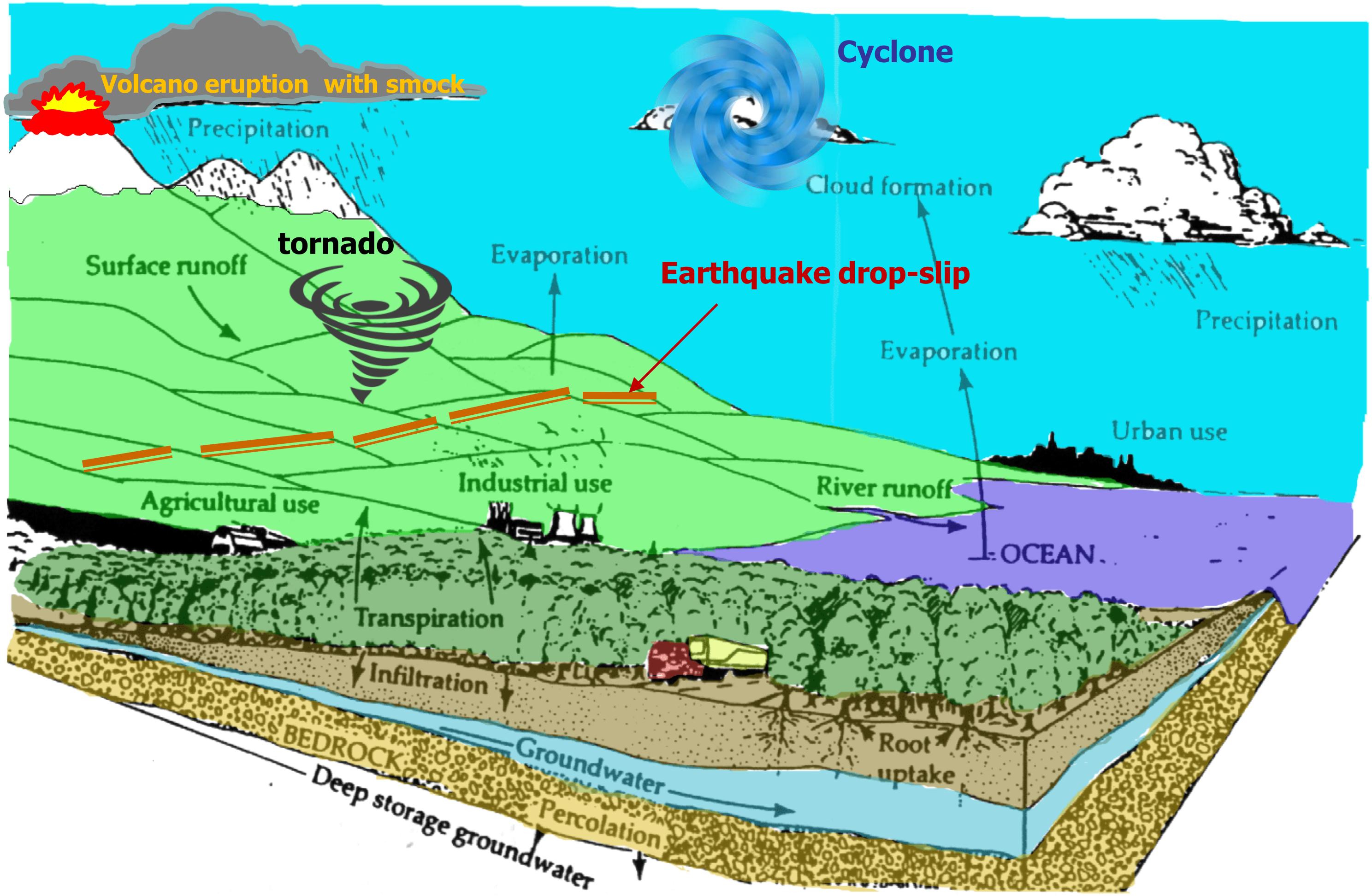

Background on Polarization Radar Theory & Polarimetric SAR Scattering Matrix Acquisition

- Kennaugh's basic Polarization radar concept: The radar target operator
- Kennaugh-Huynen Polarization Fork
- Characteristic Coherent Radar Co/Cross-Polarization Signatures
- The completely coherent case
- The partially coherent case

Kennaugh's Polarization Radar formulation

$$\mathbf{E}^s(\mathbf{r}) = [S]\,\mathbf{E}^{i*}(\mathbf{r}) \tag{4.1}$$

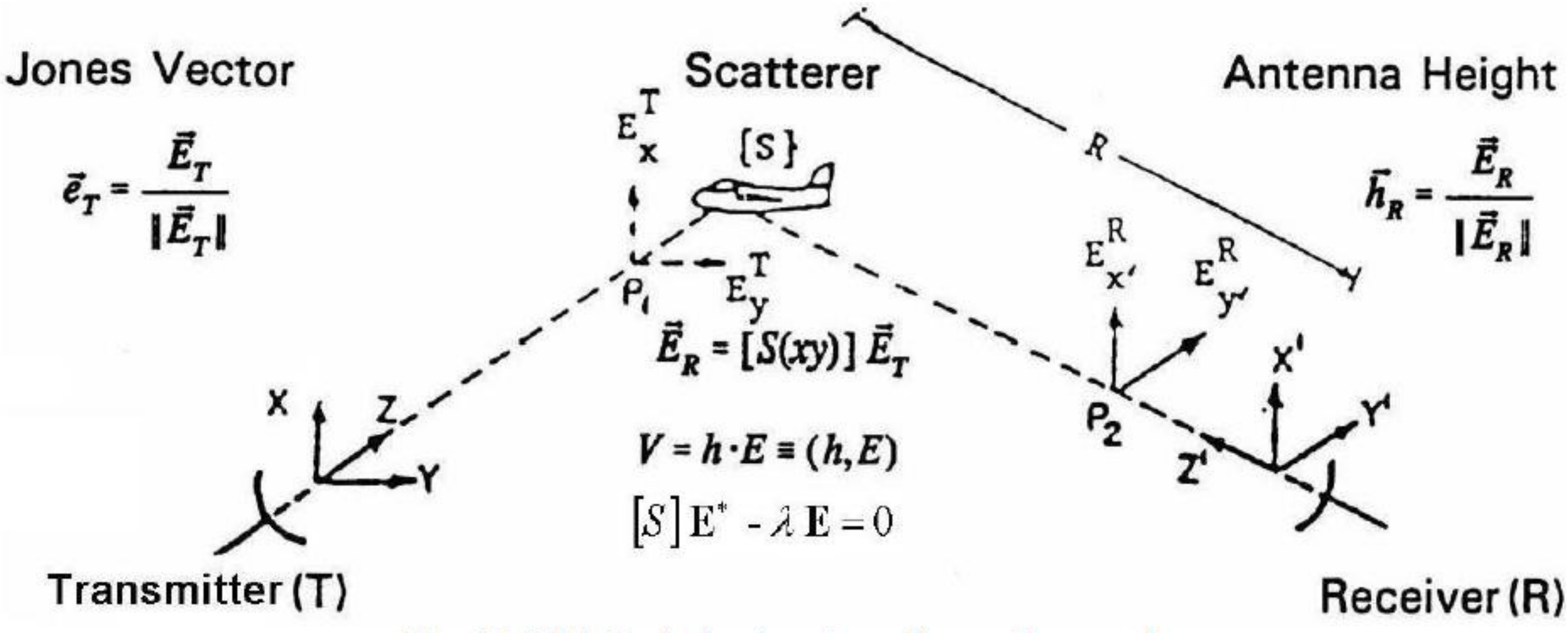

Huynen's Polarization Fork and its Significance to (Radar)-Polarimetry

Xi-Boerner[1] Solution of the Polarization Fork

$$[S] = [U^*(\rho)]\exp(\nu[L]^*)\,m\begin{bmatrix}1 & 0\\ 0 & \tan^2\gamma\end{bmatrix}\exp(\nu[L]^*)^T[U^*(\rho)]^T\exp(j\xi)$$

$$[U(\rho)]^* = \frac{1}{\sqrt{1+\rho\rho^*}}\begin{bmatrix}e^{-j\psi_1} & -\rho(\phi_m,\tau_m)e^{-j\psi_4}\\ \rho^*(\phi_m,\tau_m)e^{-j\psi_1} & e^{-j\psi_4}\end{bmatrix}$$

$$m = |\lambda_1|$$

$$\rho'_{xn1} = H = \rho'_{cm1}\,,\quad \rho'_{xn2} = V = \rho'_{cm2}$$

$$\rho'_{cn1,2} = \pm\tan(\pi/2-\gamma)\exp[j(2\gamma+\pi/2)]$$

$$\rho'_{xm1,2} = \pm\exp[j(2\gamma+\pi/2)] \qquad (LR)$$

$$\rho'_{xs1,2} = \pm\exp(j2\gamma) \qquad (45^\circ/135^\circ)$$

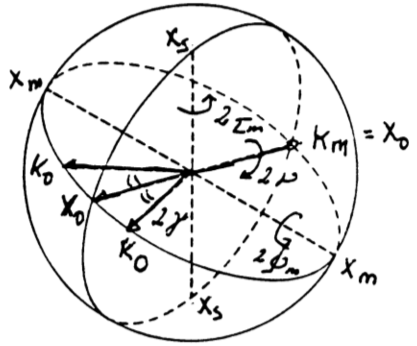

Huynen's Solution of the Polarization Fork

$$[H] = [U^*(\psi,\tau_m,\nu)]\,m\begin{bmatrix}1 & 0\\ 0 & \tan^2\gamma\end{bmatrix}[U^{*\prime}(\psi,\tau_m,\nu)]\exp(j\xi)$$

$$[U(\psi,\tau_m,\nu)] = e^{\psi[J]}e^{\tau_m[K]}e^{\nu[L]}$$

Pauli Spin-Matrices: SU(2) Unitary Rotation Group

$$[I] = \begin{bmatrix} 1 & 0 \\ 0 & 1 \end{bmatrix}, \quad [J] = \begin{bmatrix} 0 & -1 \\ 1 & 0 \end{bmatrix}, \quad [K] = \begin{bmatrix} 0 & j \\ j & 0 \end{bmatrix}, \quad [L] = \begin{bmatrix} -j & 0 \\ 0 & j \end{bmatrix}.$$

Rotation on the Polarization Unit Sphere

$m = |\lambda_1| = (\sigma_K = Span\{[S]\} + 2Det\{[S]\})$: Target Strength

ϕ Orientation Angle, ν Target-Reflection Angle, τ Target-Ellipticity

γ Characteristic Target Angle

σ_K Kennaugh's Polarimetric Excess

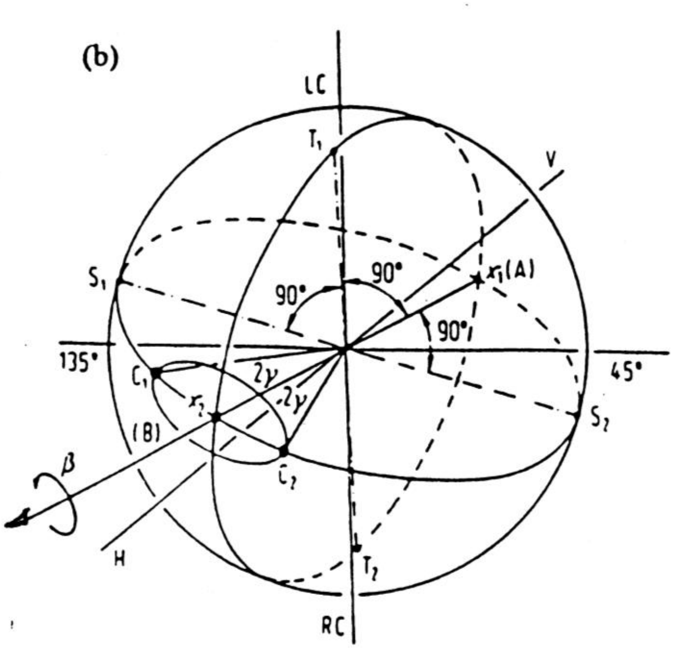

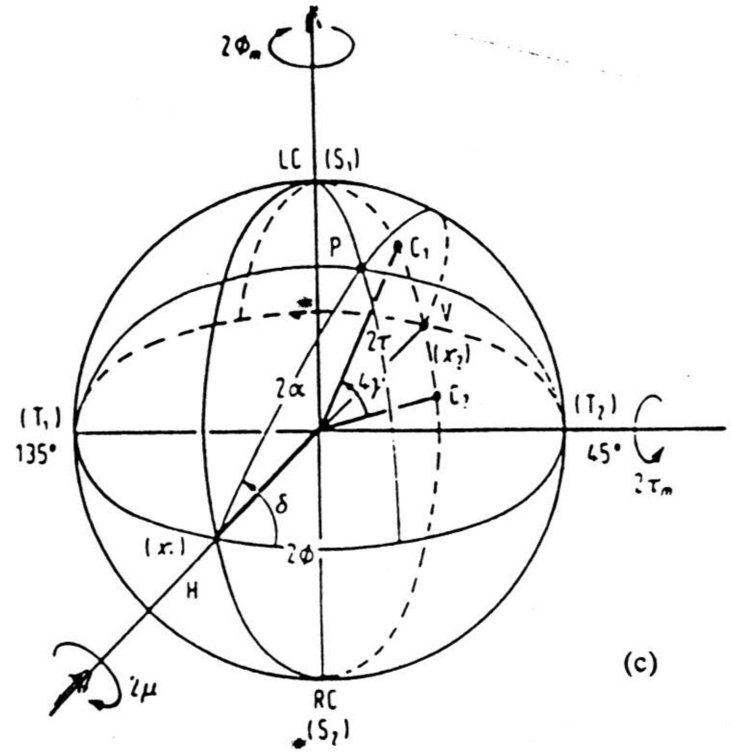

Characteristic Polarization States

X, X-Pol Null = Co-Pol Max

$C_{1,2}$ Co-Pol Nulls - Pair

$M_{1,2}$ X-Pol Max - Pair

$S_{1,2}$ X-Pol Saddle Point - Pair

Standardized Huynen Fork

m - Target Strength

ϕ - Orientation Angle

ν - Phase Change Angle

τ - Ellipticity

γ - Charakteristic Angle

Representations of Optimal Polarization States

I-2 SAR Polarimetry and SAR Interferometry.

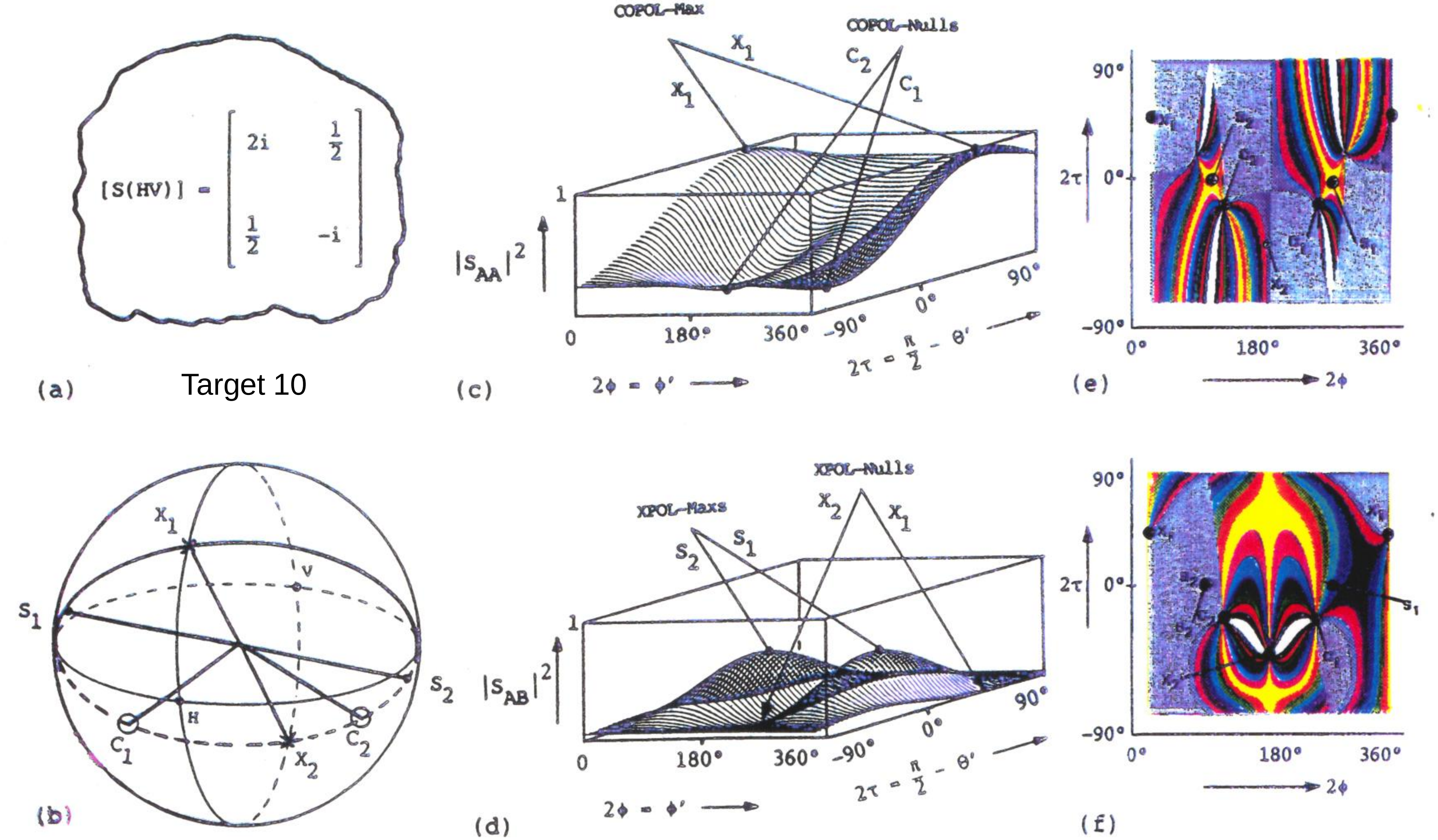

A General Example

(a) Target Shape (c) Co-Polarization Spectrum (e) Relative Co-Polarization Phase
(b) Polarization Fork (d) Cross-Polarization Spectrum (f) Relative Cross-Polarization Phase

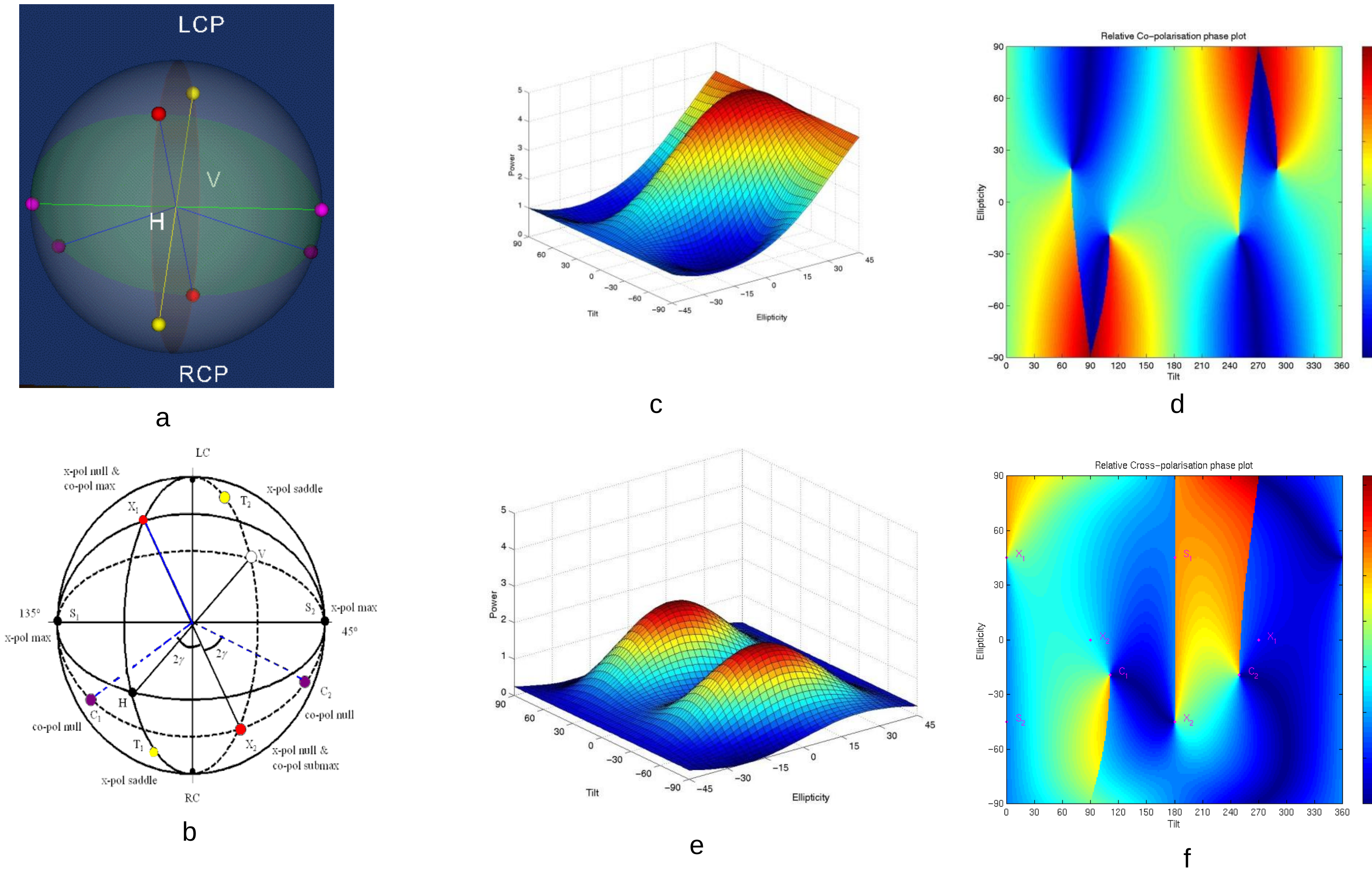

The Kennaugh Spinorial (Huynen) Polarization Fork and Polarization Power and Phase Plots

I-2 SAR Polarimetry and SAR Interferometry.

Optimization of the Kennaugh Matrix by means of the Lagrange Method (Boerner with Chan , Tanaka , Kostinski , Yan , Liu , Lüneburg ,...)

Principle: Separation of the received Stokes Vector into a fully polarized and an unpolarized Component Vector: $\vec{g}_s = \vec{g}_{pol} + \vec{g}_{unp}$

$$\vec{g}_s = \begin{pmatrix} g_{s0} \\ g_{s1} \\ g_{s2} \\ g_{s3} \end{pmatrix} = \begin{pmatrix} pg_0 \\ g_1 \\ g_2 \\ g_3 \end{pmatrix} + \begin{pmatrix} (1-p)g_0 \\ 0 \\ 0 \\ 0 \end{pmatrix}$$

p = Degree of Polarization

g_{so}	entire power density of the scattered field at the receiver
Max pg_{so}	fully polarized part of the scattered intensity (i.e., the useful "coherent partial component" in Polarimetry)
Min $(1-p)g_{so}$	unpolarized noise component, where $1/2(1-p)g_{so}$ is always received
$½(1+p)g_{so}$	maximum total intensity of the coherent component: pg_{so}

I-2 SAR Polarimetry and SAR Interferometry.

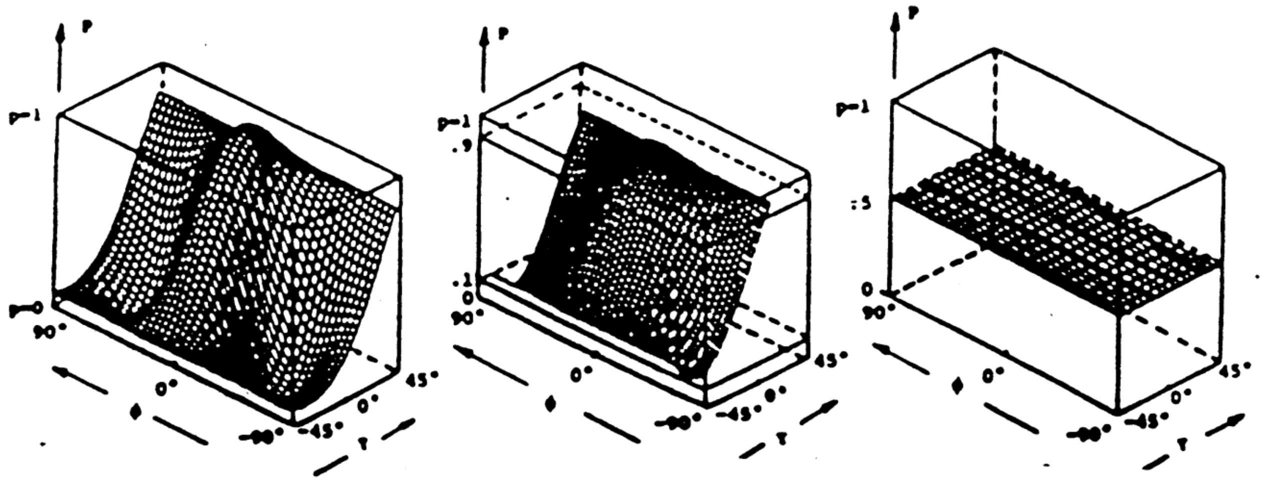

p=1
coherent
point scatterer

p = .8
distributed partially
coherent scatterer

p = 0
total polarization
noise

PARTIALLY POLARIZED: b) Dependence on the received power density from the degree of polarization p

Optimal Polarization States for the Partially Polarized Case

The Electromagnetic Vector Scattering Operator [S]

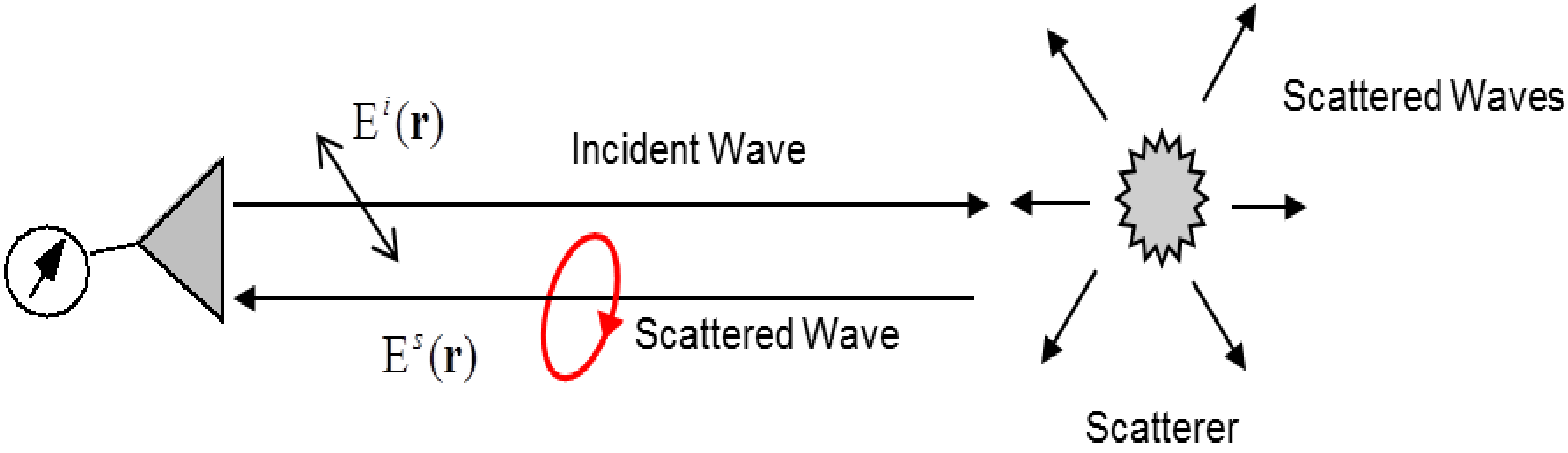

$$E^s(r) = \begin{bmatrix} E_X^s \\ E_Y^s \end{bmatrix} = \frac{e^{jkr}}{r} \begin{bmatrix} S_{XX} & S_{XY} \\ S_{YX} & S_{YY} \end{bmatrix} \begin{bmatrix} E_X^i \\ E_Y^i \end{bmatrix} = [S]E^i(r)$$

Scattering Matrix

SCATTERING MATRIX

BISTATIC CASE

SCATTERING MATRIX or JONES MATRIX

$$\begin{bmatrix} E_X^s \\ E_Y^s \end{bmatrix} = \frac{e^{jkr}}{r} \begin{bmatrix} S_{XX} & S_{XY} \\ S_{YX} & S_{YY} \end{bmatrix} \begin{bmatrix} E_X^i \\ E_Y^i \end{bmatrix}$$

DEFINED IN THE LOCAL COORDINATES SYSTEM

$[S]$ IS INDEPENDENT OF THE POLARISATION STATE OF THE INCIDENCE WAVE

$[S]$ IS DEPENDENT ON THE FREQUENCY AND THE GEOMETRICAL AND ELECTRICAL PROPERTIES OF THE SCATTERER

TOTAL SCATTERED POWER

$$Span([S]) = Trace\left([S][S]^{T*}\right) = |S_{XX}|^2 + |S_{XY}|^2 + |S_{YX}|^2 + |S_{YY}|^2$$

Backscattering Matrix

MONOSTATIC CASE

BACKSCATTERING MATRIX or SINCLAIR MATRIX

$\Downarrow$

In the case of Backscattering from Reciprocal Scatterers:

RECIPROCITY THEOREM $$S_{XY}^{BSA} = S_{YX}^{BSA} \Leftrightarrow S_{XY}^{FSA} = -S_{YX}^{FSA}$$

$\Downarrow$

$$\begin{bmatrix} E_X^s \\ E_Y^s \end{bmatrix} = \frac{e^{jkr}}{r} \begin{bmatrix} S_{XX} & S_{XY} \\ S_{XY} & S_{YY} \end{bmatrix} \begin{bmatrix} E_X^i \\ E_Y^i \end{bmatrix}$$

(BSA CONVENTION)

TOTAL SCATTERED POWER

$$Span([S]) = Trace\left([S][S]^{T*}\right) = |S_{XX}|^2 + 2|S_{XY}|^2 + |S_{YY}|^2$$

Polarimetric airborne SAR sensors

- There exist several airborne multi-modal SAR Imaging platforms that support fully polarimetric POLSAR systems – such as
- the NASA-JPL AIR/TOP-SAR
- the DLR ESAR – replaced by FSAR
- the ONERA RAMSES SAR
- And by today more than 12 airborne platforms, of which the FSAR is used here

POLARIMETRIC AIRBORNE SAR SENSORS

AES1
AeroSensing (D)
GulfStream Commander
X-Band (HH), P-Band (Quad)

AIRSAR
NASA / JPL (USA)
DC8
P, L, C-Band (Quad)

DOSAR
EADS / Dornier GmbH (D)
DO 228 (1989), C160 (1998), G222 (2000)
S, C, X-Band (Quad), Ka-Band (VV)

RENE
UVSQ / CETP (F)
Écureuil AS350
S, X-Band (Quad)

ESAR
DLR (D)
DO 228
P, L, S-Band (Quad)
C, X-Band (Sngl)

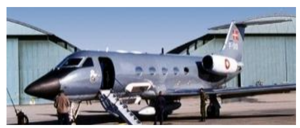

EMISAR
DCRS (DK)
G3 Aircraft
L, C-Band (Quad)

MEMPHIS / AER II-PAMIR
FGAN (D)
Transal C160
Ka, W-Band (Quad) / X-Band (Quad)

STORM
UVSQ / CETP (F)
Merlin IV
C-Band (Quad)

PHARUS
TNO - FEL (NL)
CESSNA – Citation II
C-Band (Quad)

PISAR
NASDA / CRL (J)
GulfStream
L, X-Band (Quad)

RAMSES
ONERA (F)
Transal C160
P, L, S, C, X, Ku, Ka, W-Band (Quad)

SAR580
CCRS (CA)
Convair CV-580
C, X-Band (Quad)

+ *CASSAR (China), MIT/Lincoln Lab (USA), P3-SAR (NADC / ERIM -USA), Military Systems …*

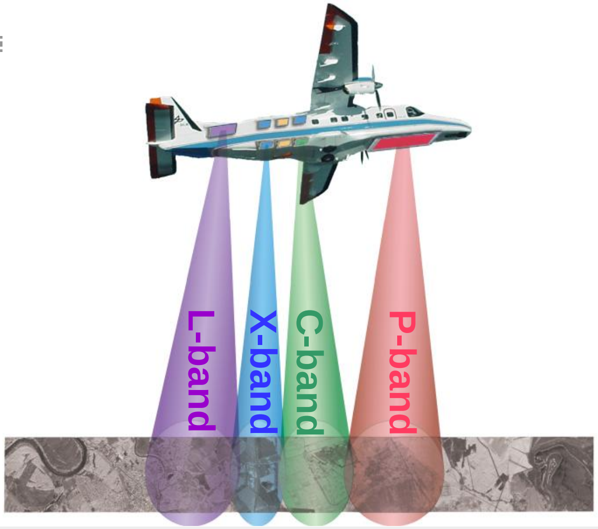

New features:
- significantly enhanced resolution and image quality
- simultaneous data recording in up to four frequency bands
- modular design for easy reconfiguration
- single-pass polarimetric interferometry in X- and S-band
- fully polarimetric capability in all frequencies

E-SAR technical characteristics

	X	C	L	P
RF [GHz]	9.6	5.3	1.3	0.35
BW [MHz]	50-100 (selectable)			
PRF [kHz]	up to 2			
Rg res. [m]	1.5	1.5	2.0	3.0
Az res. [m]	0.2	0.3	0.4	1.5
Pol/InSAR	-/+	-/-	+/o	+/o
Rg cov [km]	3-5			
Sampling	6-8 Bit complex; 100MHz; max number of samples 4 K per range line; 1 recording channel.			

F-SAR technical characteristics

	X	C	S	L	P
RF [GHz]	9.6	5.3	3.2	1.3	0.35
BW [MHz]	800	400	300	150	100
PRF [kHz]	up to 12				
Rg res. [m]	0.3	0.6	0.75	1.5	2.25
Az res. [m]	0.2	0.3	0.35	0.4	1.5
Pol/InSAR	+/+	+/o	+/+	+/o	+/o
Rg cov [km]	12.5 (at max.bandwith)				
Sampling	8 Bit real; 1000MHz; max number of samples 64 K per range line; 4 recording channels.				

E-SAR and F-SAR

- The E-SAR and F-SAR are operated onboard DLR’s DO228-212 D-CFFU by the Microwaves and Radar Institute in cooperation with DLR’s Flight Facilities based in Oberpfaffenhofen

  The F-SAR is currently in development and is planned to fully replace the E-SAR until middle of 2011

F-SAR X-Band Quad-Pol

DLR
F-SAR
S-band
Quad-Pol

Zoom

Main Satellite POLSAR sensors

- **L-Band:** ALOS-PALSAR JAXA/Japan in Jan 2006 – followed by ALOS-PALSAR-2
- **C-Band:** RADARSAT-2 CSA-MDA in Dec 2007 – followed by RADARSAT-3 & 4
- **X-Band:** TerraSAR-X DLR-Astrium in July 2007 with follow-on tandem mission Tan-DEM-X (Fig. 2) launched in June 2010
- **Tandem L-Band:** All of these efforts will be topped by joint DLR-JAXA TanDEM-L wide-swath, high-resolution fully polarimetric sensor implementation,

Table 1. Comparison of High-Level Parameters			
Parameter	**PALSAR**	**RADARSAT-2**	**TerraSAR-X**
Orbit: LEO, circular	Sun-synchronous	Sun-synchronous	Sun-synchronous
Repeat Period (*days*)	46	24	11
Equatorial Crossing time (*hrs*)	22:30 (ascending)	18:00 (ascending)	18.00 (ascending)
Inclination (*degrees*)	98.16	98.6	97.44
Equatorial Altitude (*km*)	692	798	515
Wavelength (*Band*)	23 cm (*L*)	5.6 cm (*C*)	3 cm (*X*)
Fully polarimetric mode	Yes	Yes	Yes

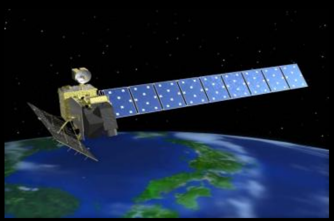

ALOS / PALSAR
Japanese Space Agency (JAXA)
L-Band (quad), 2006

RadarSAT-II
Canadian Space Agency (CSA)
C-Band (quad), 2007

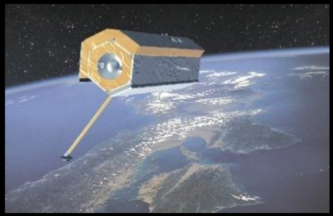

TerraSAR-X
German Aerospace Center (DLR) / Astirum
X-Band (quad), 2007

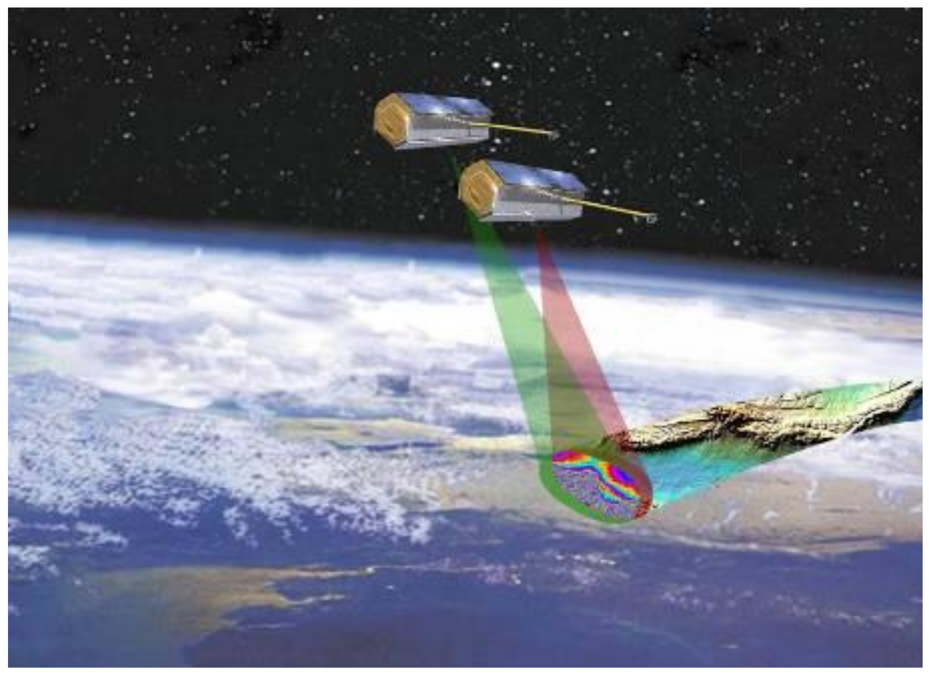

TerraSAR – X (1 & 2)
(2010)

Pol – InSAR Sensors

TanDEM-X

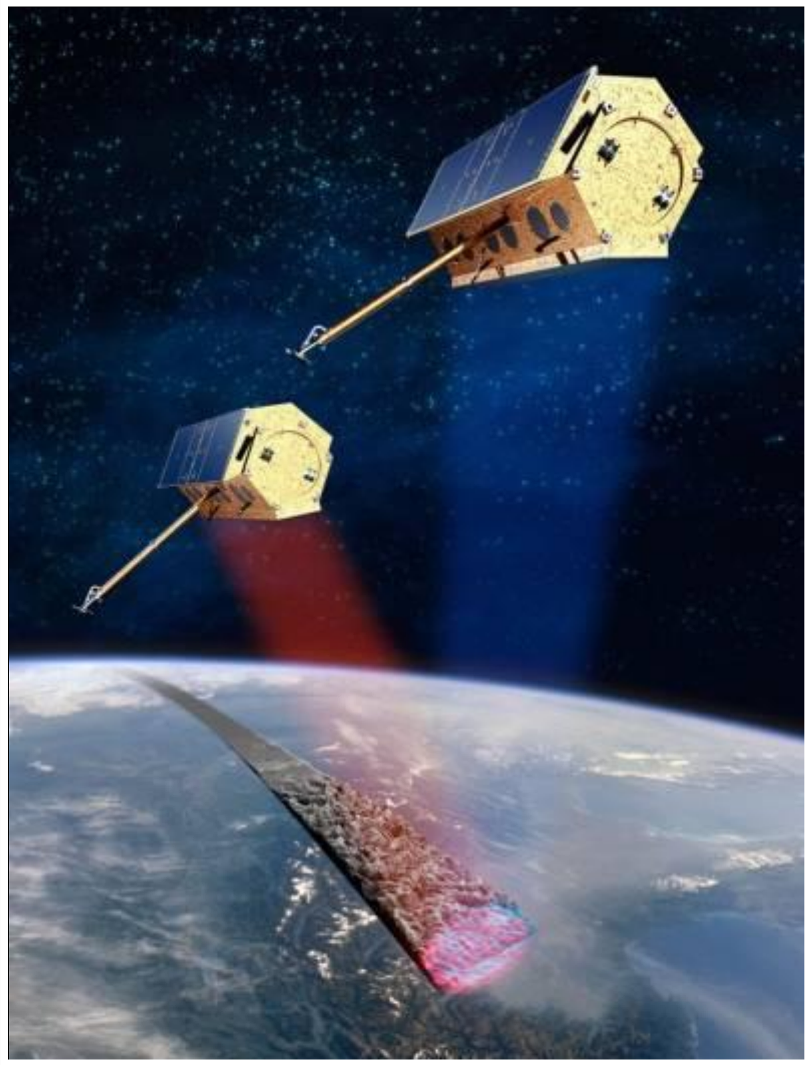

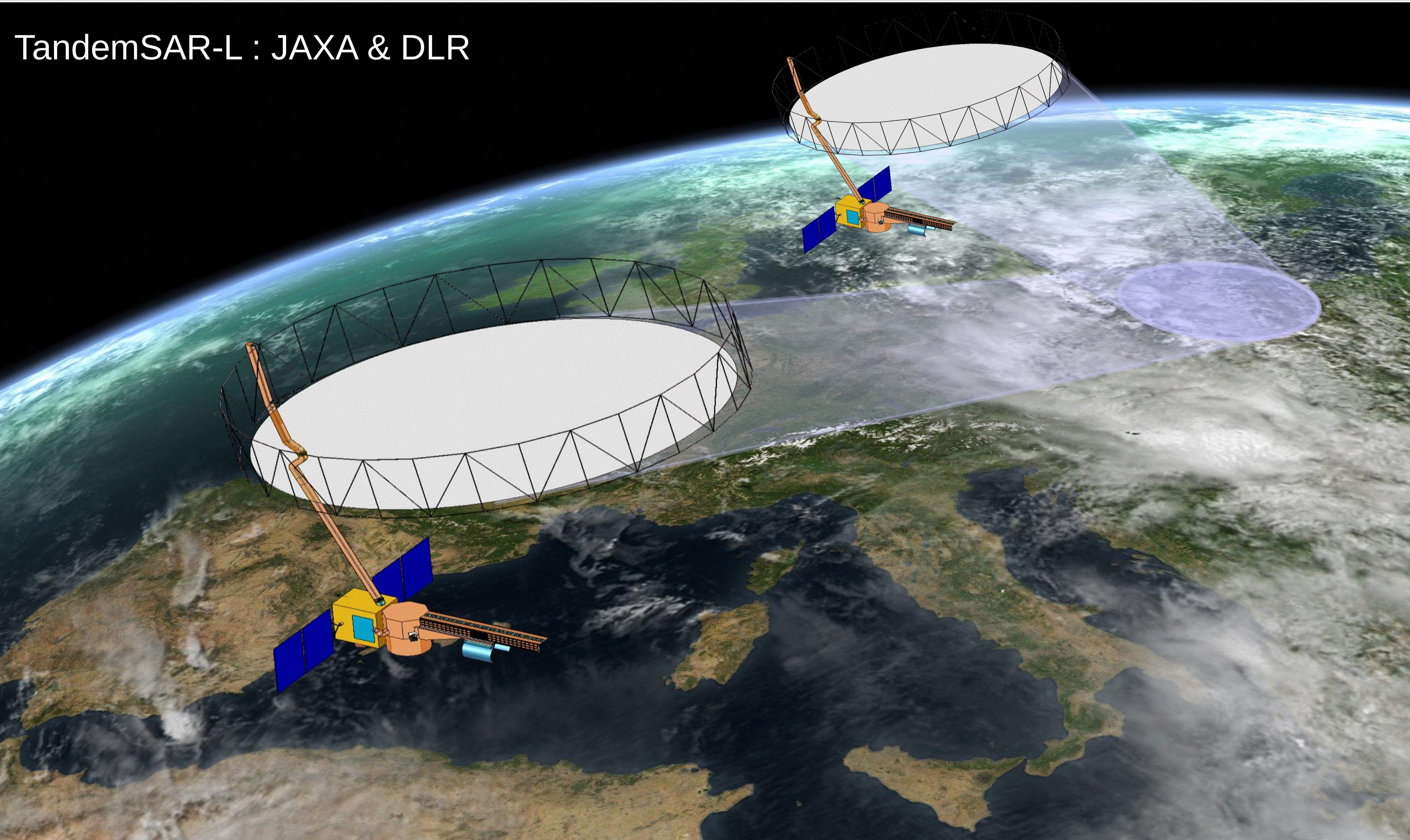
TandemSAR-L : JAXA & DLR

The TerraSAR-X satellite bus claims heritage from the successful Champ and Grace Missions. The spacecraft bus features a primary structure with a hexagonal cross section. The active phased array SAR antenna is attached on the Earth-facing panel in the figure. The solar array is body-mounted, a satisfactory scheme for the sun-synchronous orbit plan. The X-Band down link antenna is mounted on a 3.3 m long deployable boom in order to prevent interference with the X-Band SAR instrument. This concept enables simultaneous data acquisition and data down link.

Table 1. Selected Mode Parameters

Mode (selected)	Resolution (m)	Swath (km)	Looks	Polarization
Standard, stripmap	3	30	1	HH or VV
High-resolution Spotlight	1	10	1	HH or VV
ScanSAR	16	100	1	HH or VV
Quad-pol (experimental)	3	15	1	Full polarization

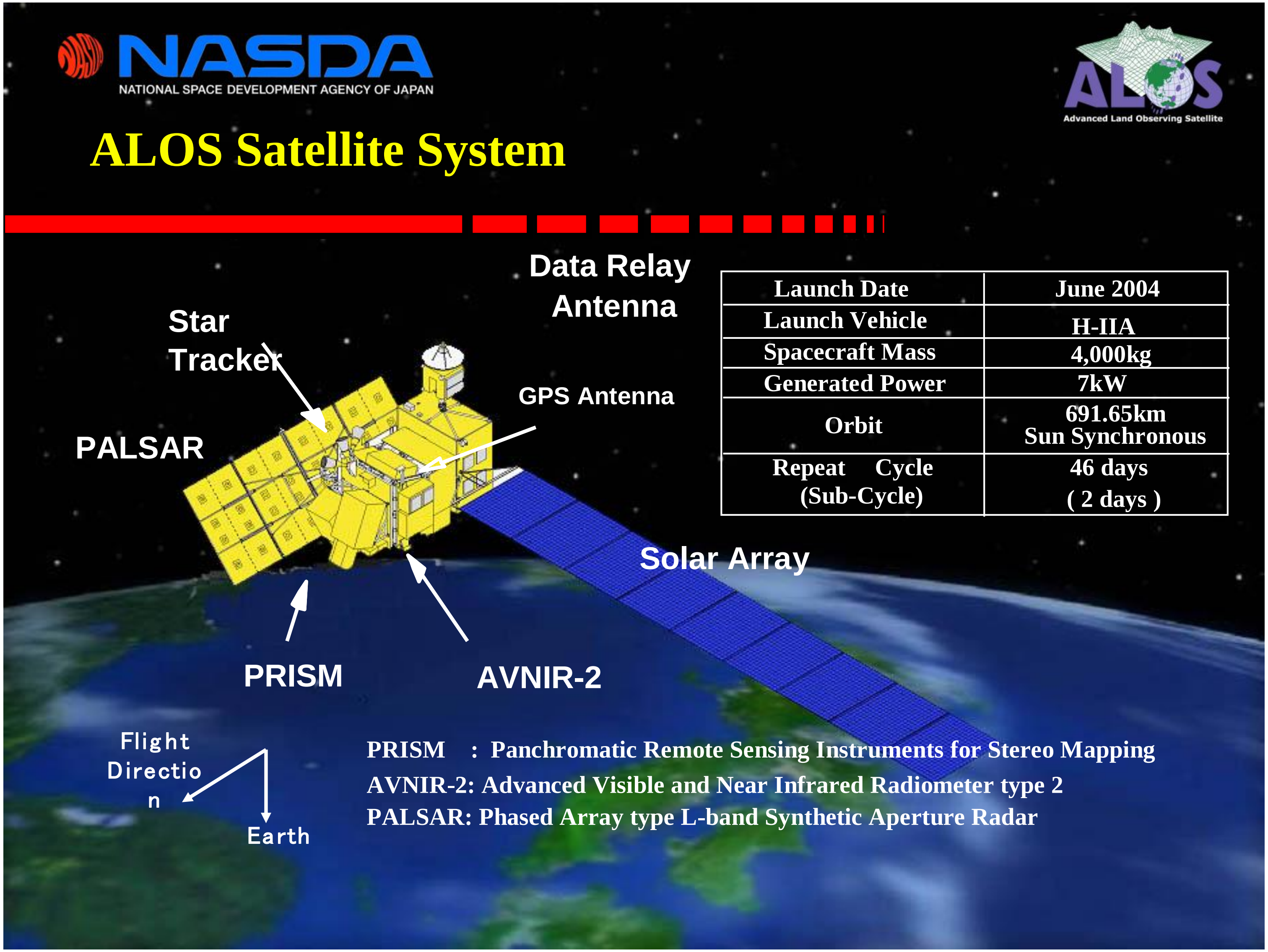
NASDA
NATIONAL SPACE DEVELOPMENT AGENCY OF JAPAN
ALOS
Advanced Land Observing Satellite
ALOS Satellite System
Data Relay Antenna
Star Tracker
GPS Antenna
PALSAR
Solar Array
PRISM
AVNIR-2
Flight Directio n
Earth

Launch Date	June 2004
Launch Vehicle	H-IIA
Spacecraft Mass	4,000kg
Generated Power	7kW
Orbit	691.65km Sun Synchronous
Repeat Cycle (Sub-Cycle)	46 days (2 days)

PRISM : Panchromatic Remote Sensing Instruments for Stereo Mapping
AVNIR-2: Advanced Visible and Near Infrared Radiometer type 2
PALSAR: Phased Array type L-band Synthetic Aperture Radar

	ALOS	ALOS-2
Launch	Jan. 24, 2006	**May 24, 2014**
Orbit type	Sun-synchronous	
Altitude	690 km	628 km +/- 500 m (for reference orbit)
Revisit time	46 days	14 days
LSDN	10:30	12:00 +/- 15 min
Sensor	PALSAR, PRISM, AVNIR-2	PALSAR-2

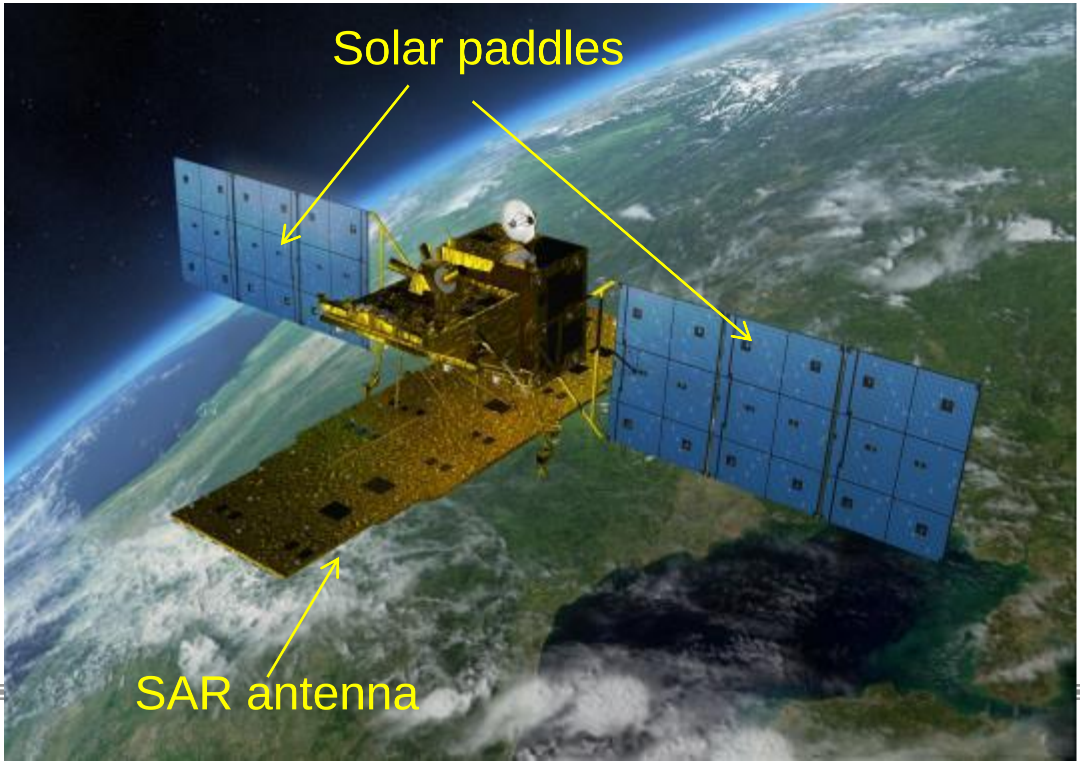

	PALSAR	PALSAR-2
Band	L-band Synthetic Aperture Radar	
Antenna	Active Phased Array Antenna type **one** dimensions scan (range)	Active Phased Array Antenna type **two** dimensions scan (range and azimuth)
Antenna size	3m(El) x 9m(Az)	3m(El) x 10m(Az)
Bandwidth	14/**28** MHz	14 – **84**MHz
Peak transmit Power	≥ 2000 W	5100W
Observation swath	35– **350**km	25 – **490**km
Resolution	Range : 10 m to 100 m Azimuth: 10 m to 100 m	Range : 3 m to 100 m Azimuth: 1 m to 100 m

PALSAR-2 Specifications

<table>
<tr><th colspan="2"></th><th>Spotlight</th><th>Ultra Fine</th><th>High sensitive</th><th>Fine</th><th colspan="2">ScanSAR nominal</th><th>ScanSAR wide</th></tr>
<tr><td colspan="2">Bandwidth</td><td>84MHz</td><td>84MHz</td><td>42MHz</td><td>28MHz</td><td>14MHz</td><td>28MHz</td><td>14MHz</td></tr>
<tr><td colspan="2">Resolution</td><td>Rg×Az:
3×1m</td><td>3m</td><td>6m</td><td>10m</td><td colspan="2">100m</td><td>60m</td></tr>
<tr><td colspan="2">Swath</td><td>Rg×Az:
25×25km</td><td>50km</td><td>50km</td><td>70km</td><td colspan="2">350km
(5-scan)</td><td>490km
(7-scan)</td></tr>
<tr><td colspan="2">Polarization</td><td>SP</td><td>SP/DP</td><td colspan="2">SP/DP/QP/CP</td><td colspan="3">SP/DP</td></tr>
<tr><td colspan="2">NESZ</td><td>-24dB</td><td>-24dB</td><td>-28dB</td><td>-26dB</td><td>-26dB</td><td>-23dB</td><td>-23dB</td></tr>
<tr><td rowspan="2">S/A</td><td>Rg</td><td>25dB</td><td>25dB</td><td>23dB</td><td>25dB</td><td colspan="2">25dB</td><td>20dB</td></tr>
<tr><td>Az</td><td>20dB</td><td>25dB</td><td>20dB</td><td>23dB</td><td colspan="2">20dB</td><td>20dB</td></tr>
</table>

SP : HH or VV or HV , DP : HH+HV or VV+VH , FP : HH+HV+VH+VV , CP : Compact pol (Experimental mode)

Main applications:

Fine beam (DP) : Forest and land cover monitoring / DinSAR
ScanSAR (DP) : Rapid deforestation / wetlands / (ScanSAR)InSAR
Spotlight (SP) : Emergency observations
Ultra Fine (SP) : Global map, InSAR base mapping
High sensitive (QP) : Global map
ScanSAR wide (SP) : Polar ice

ALOS is one of the largest Earth observing satellites ever developed, at 3850 kg. It is in a near-exact 45-day repeat sun-synchronous orbit, 690 km altitude above the equator. The active phased array SAR antenna is obliquely Earth-facing, aligned with the spacecraft velocity vector. The solar array is arranged at right angles to the orbit plane, consistent with the near-mid-day orbit phasing. The X-band down-link must be shared with optical instruments, which constrains SAR operation times.

Table 1. Selected PALSAR Mode Parameters

Mode (selected)	Resolution (m)	Swath (km)	Looks	Polarization
Standard, stripmap	20 x 10	70	2	HH or VV
Fine	10	70	1	HH or VV
ScanSAR (5-beam)	~ 100	350	8	HH or VV
Dual polarization	(as above)	(as above)	(as above)	(HH, HV), (VV, VH)
Quad-pol	30 x 10	30	2	Full polarization

Scattering matrix decomposition theories and algorithms

- In order to relate polarimetric properties to scatterer characteristics, attempts were made first by Kennaugh, then Huynen to make use of the coherent Kennaugh matrix decomposition, which for the partially coherent case was then explored among others by Barnes & Holm, Durden & Freeman, and more recently by Yamaguchi & Singh.
- However, the full decompositions of Huynen & Kennaugh may still be superior (Touzi)

VECTORIAL FORMULATION OF THE SCATTERING PROBLEM

SCATTERING MATRIX

$$[S] = \begin{bmatrix} S_{XX} & S_{XY} \\ S_{YX} & S_{YY} \end{bmatrix}$$

$$\Downarrow$$

SCATTERING VECTOR

$$\vec{S} := V([S]) = \frac{1}{2} Trace([S][\Psi]) = \begin{bmatrix} S1 \\ S2 \\ S3 \\ S4 \end{bmatrix} \in C_4$$

With: $V([S])$ MATRIX VECTORISATION OPERATOR

$[\Psi]$ SET OF ORTHOGONAL 2x2 MATRICES

FROBENIOUS NORM OF $\vec{S}$

$$\begin{aligned} \|\vec{S}\|^2 &= \vec{S}^{T*} \cdot \vec{S} = |S_1|^2 + |S_2|^2 + |S_3|^2 + |S_4|^2 \\ &= Span([S]) = |S_{XX}|^2 + |S_{YX}|^2 + |S_{XY}|^2 + |S_{YY}|^2 \end{aligned}$$

PAULI SCATTERING VECTOR

$$\underline{k} = V([S]) = \frac{1}{2} Trace([S][\psi_P])$$

SET OF 2x2 COMPLEX MATRICES FROM THE PAULI MATRICES GROUP

$$[\psi_P] = \left\{ \sqrt{2}\begin{bmatrix} 1 & 0 \\ 0 & 1 \end{bmatrix}, \sqrt{2}\begin{bmatrix} 1 & 0 \\ 0 & -1 \end{bmatrix}, \sqrt{2}\begin{bmatrix} 0 & 1 \\ 1 & 0 \end{bmatrix}, \sqrt{2}\begin{bmatrix} 0 & -j \\ j & 0 \end{bmatrix} \right\}$$

$$\boxed{\underline{k} = \frac{1}{\sqrt{2}}\left[S_{XX} + S_{YY} \quad S_{XX} - S_{YY} \quad S_{XY} + S_{YX} \quad j(S_{XY} - S_{YX})\right]^T}$$

Advantage: Closer related to physical properties of the scatterer

LEXICOGRAPHIC SCATTERING VECTOR $\underline{\Omega} = V([S]) = \frac{1}{2} Trace([S][\psi_L])$

SET OF 2x2 COMPLEX MATRICES
FROM THE LEXICOGRAPHIC MATRICES GROUP

$$[\psi_L] = \left\{ 2\begin{bmatrix} 1 & 0 \\ 0 & 0 \end{bmatrix}, 2\begin{bmatrix} 0 & 1 \\ 0 & 0 \end{bmatrix}, 2\begin{bmatrix} 0 & 0 \\ 1 & 0 \end{bmatrix}, 2\begin{bmatrix} 0 & 0 \\ 0 & 1 \end{bmatrix} \right\}$$

$$\Downarrow$$

$$\underline{\Omega} = \begin{bmatrix} S_{XX} & S_{XY} & S_{YX} & S_{YY} \end{bmatrix}^T$$

Advantage: Directly related to the system measurables

SCATTERING VECTOR TRANSFORMATIONS

Pauli Scattering Vector:

$$\underline{k} = \frac{1}{\sqrt{2}}\begin{bmatrix} S_{XX} + S_{YY} \\ S_{XX} - S_{YY} \\ S_{XY} + S_{YX} \\ j\left(S_{XY} - S_{YX}\right) \end{bmatrix}$$

Lexicographic Scattering Vector:

$$\underline{\Omega} = \begin{bmatrix} S_{XX} \\ S_{XY} \\ S_{YX} \\ S_{YY} \end{bmatrix}$$

UNITARY TRANSFORMATION

$$\underline{k} = [D_4]\underline{\Omega} \quad and \quad \underline{\Omega} = [D_4]^{-1}\underline{k} = [D_4]^{T*}\underline{k}$$

WHERE $[D_4]$ IS A SU(4) MATRIX IN ORDER TO PRESERVE THE NORM OF THE SCATTERING VECTOR

$$[D_4] = \frac{1}{\sqrt{2}}\begin{bmatrix} 1 & 0 & 0 & 1 \\ 1 & 0 & 0 & -1 \\ 0 & 1 & 1 & 0 \\ 0 & j & -j & 0 \end{bmatrix}$$

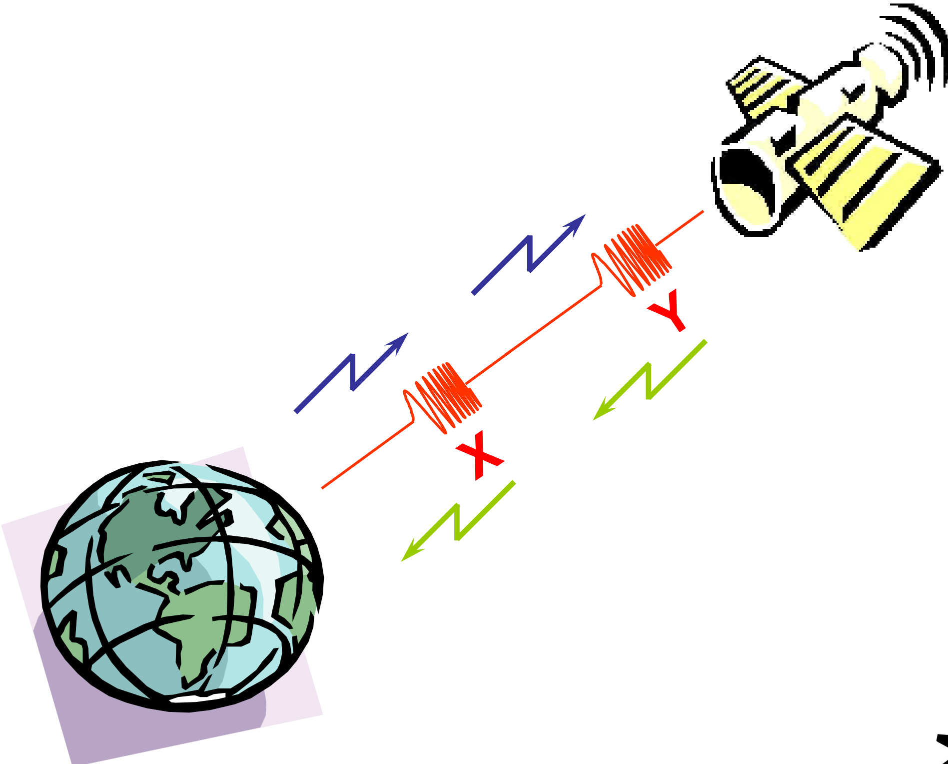

THE DIFFERENT
TARGET POLARIMETRIC
DESCRIPTORS

[S] SINCLAIR Matrix
k, W Target Vectors
[K] KENNAUGH Matrix
[T] Coherency Matrix
[C] Covariance Matrix

TRANSMITTER: X & Y
RECEIVERS: X & Y

STATISTICAL DESCRIPTION

PARTIAL SCATTERING POLARIMETRY

Incoherent decomposition of FULL-POL-SAR data

- Eigenvalue analysis — H/alpha/Anisotropy (1997)
- Model-based scattering power decomposition
  - FDD: Freeman & Durden: 3-component (1998)
  - Y40: 3-comp. + helix scattering = 4-comp. (2005)
  - Y4R: 4-comp. with rotation (2011)
  - S4R: Y4R + extended volume scattering (2012)
  - G4U: S4R with additional unitary transform (2013)
- Hybrid Model-based/Eigenvalue decomposition
  - Hybrid Freeman/Eigenvalue Decomposition (2009)
  - General Hybrid Decomposition (2013)

Polarization matrices and their relations

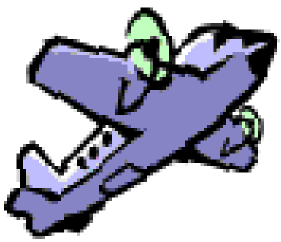

Data acquisition

$$[\,S\,(HV)\,] = \begin{bmatrix} S_{HH} & S_{HV} \\ S_{VH} & S_{VV} \end{bmatrix}$$

Scattering matrix
(HV, LR basis)

2nd order statistics

3 x 3 polarization matrix

$\langle [C] \rangle$ Covariance (HV, LR basis)

$\langle [T] \rangle$ Coherency

4 x 4 polarization matrix
real valued elements

$\langle [K] \rangle$ Kennaugh

$\langle [M] \rangle$ Mueller

Full-Pol-SAR Data

Space-borne

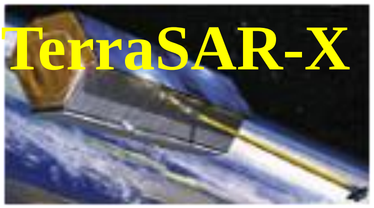

Air-borne

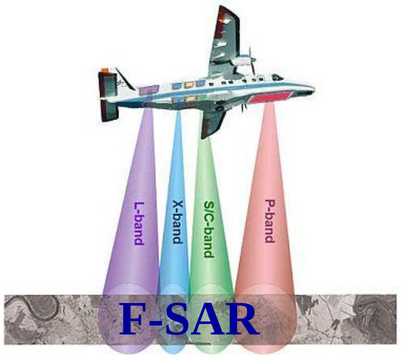

Polarimetric Radar measures

Scattering Matrix

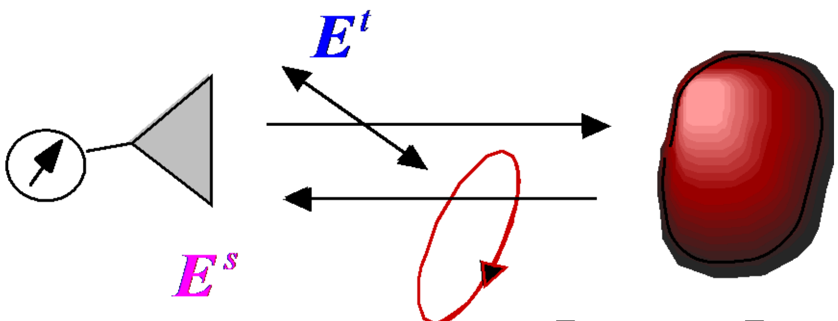

$$\boldsymbol{E}^s = \begin{bmatrix} E_H^s \\ E_V^s \end{bmatrix} = \begin{bmatrix} S_{HH} & S_{HV} \\ S_{VH} & S_{VV} \end{bmatrix} \begin{vmatrix} E_H^t \\ E_V^t \end{vmatrix} = [S]\,\boldsymbol{E}^t$$

Scattering Matrix

POLSAR image analysis

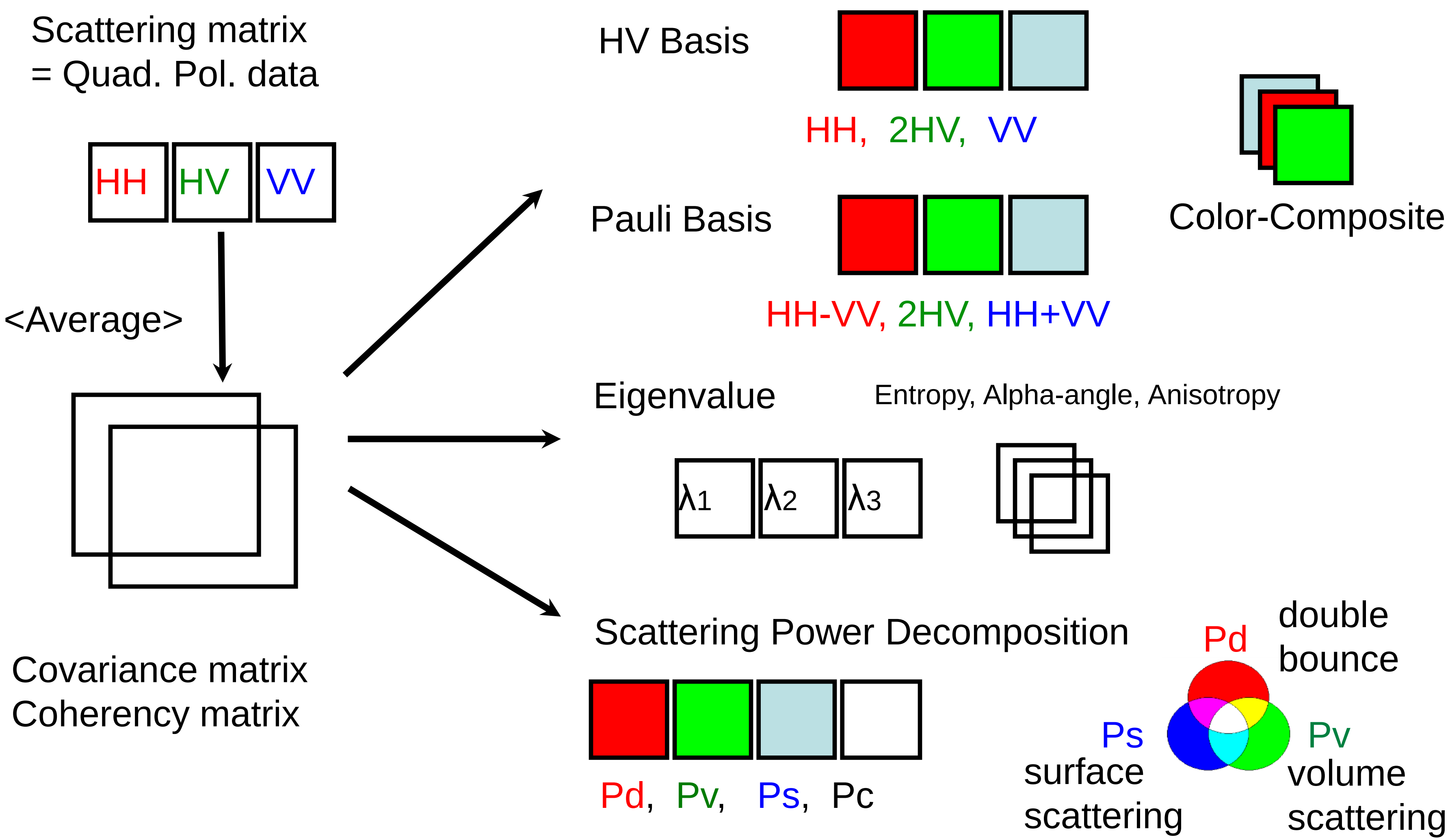

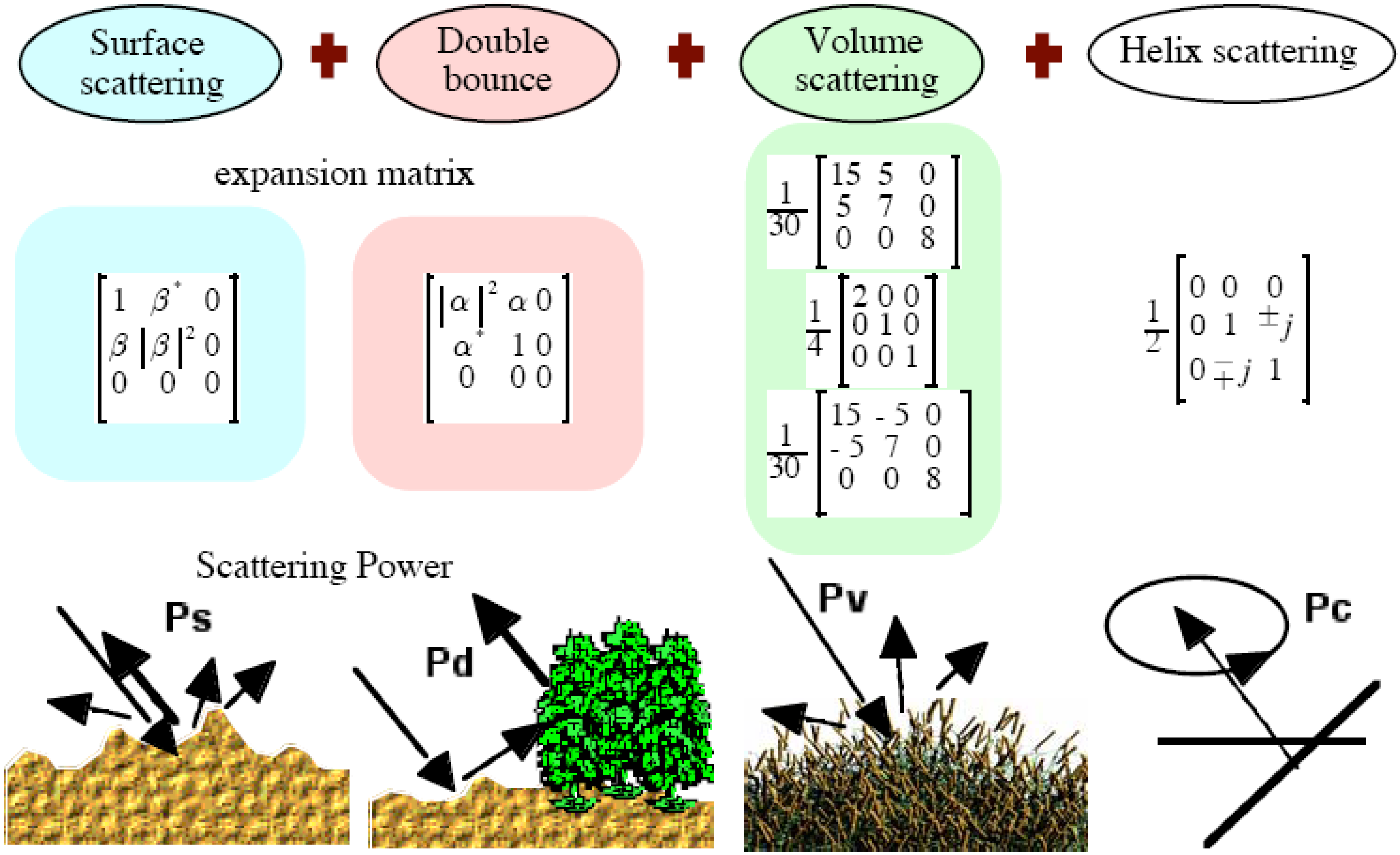

The four-component decomposition of scattering powers Ps, Pd, Pv, and Pc *under the condition of mono-static radar* $S_{HV} = S_{VH}$

Coherent

5

$$[S]_{relative} = \begin{bmatrix} |S_{HH}| & |S_{HV}| e^{j(\varphi_{HV} - \varphi_{HH})} \\ |S_{VH}| e^{j(\varphi_{VH} - \varphi_{HH})} & |S_{VV}| e^{j(\varphi_{VV} - \varphi_{HH})} \end{bmatrix}$$

Scattering matrix

$$\boldsymbol{k}_p = (1/2)\ \mathrm{Trace}\ \{S[\psi]\} = \frac{1}{\sqrt{2}} \begin{bmatrix} S_{HH} + S_{VV} \\ S_{HH} - S_{VV} \\ 2S_{HV} \end{bmatrix}$$

Scattering vector

$$\Psi = \left\{ \sqrt{2}\begin{bmatrix} 1 & 0 \\ 0 & 1 \end{bmatrix}, \sqrt{2}\begin{bmatrix} 1 & 0 \\ 0 & -1 \end{bmatrix}, \sqrt{2}\begin{bmatrix} 0 & 1 \\ 1 & 0 \end{bmatrix} \right\}$$

Incoherent

Coherency or Covariance matrix

9

$$\langle [T] \rangle = \frac{1}{n} \sum^{n} \boldsymbol{k}_P \boldsymbol{k}_P^{\dagger} = \frac{1}{2}$$

Re Im Re Im

$$\begin{bmatrix} \langle |S_{HH} + S_{VV}|^2 \rangle & \langle (S_{HH} + S_{VV})(S_{HH} - S_{VV})^* \rangle & \langle 2 S_{HV}^* (S_{HH} + S_{VV}) \rangle \\ \langle (S_{HH} - S_{VV})(S_{HH} + S_{VV})^* \rangle & \langle |S_{HH} - S_{VV}|^2 \rangle & \langle 2 S_{HV}^* (S_{HH} - S_{VV}) \rangle \\ \langle 2 S_{HV} (S_{HH} + S_{VV})^* \rangle & \langle 2 S_{HV} (S_{HH} - S_{VV})^* \rangle & \langle 4 |S_{HV}|^2 \rangle \end{bmatrix}$$

How many independent polarimetric information ?

Advantages of Coherency Matrix

$$\langle [\,T\,] \rangle = \begin{bmatrix} T_{11} & T_{12} & T_{13} \\ T_{12}^{*} & T_{22} & T_{23} \\ T_{13}^{*} & T_{23}^{*} & T_{33} \end{bmatrix}$$

Elements are related to physical scattering nature

The second order statistics of polarimetric information

All the information contained is the same as those of 3x3 covariance matrix

Easy to formulate and unitary transform

FDD

Freeman and Durden 3-Component Scattering Power Decomposition [1]

$$[T] = f_s[T_s] + f_d[T_d] + f_v[T_v]$$

$$[T] = f_s \begin{bmatrix} 1 & \beta^* & 0 \\ \beta & |\beta|^2 & 0 \\ 0 & 0 & 0 \end{bmatrix} + f_d \begin{bmatrix} |\alpha|^2 & \alpha & 0 \\ \alpha^* & 1 & 0 \\ 0 & 0 & 0 \end{bmatrix} + f_v \cdot \frac{1}{4} \begin{bmatrix} 2 & 0 & 0 \\ 0 & 1 & 0 \\ 0 & 0 & 1 \end{bmatrix}$$

with reflection symmetry $\langle S_{HH} S_{HV}^* \rangle \approx 0, \ \langle S_{VV} S_{HV}^* \rangle \approx 0$ for natural distributed targets

Total Power (TP)=

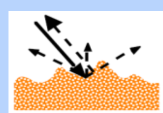

Surface Scattering

Ps

+

Double Bounce Scattering

Pd

+

Volume scattering

Pv

[1] A. Freeman and S. L. Durden, ``A Three-component scattering model for polarimetric SAR data,`` IEEE TGRS, Vol.36, No. 3, pp. 963-973, May 1998.

FDD ⇨ Y4O Component Scattering power decomposition

$$\langle [T] \rangle = f_s \langle [T] \rangle_{surface} + f_d \langle [T] \rangle_{double} + f_v \langle [T] \rangle_{vol} + f_c \langle [T] \rangle_{helix}$$

for general case $\langle S_{HH} S_{HV}^* \rangle \neq 0, \ \langle S_{VV} S_{HV}^* \rangle \neq 0$

$$= f_s \begin{bmatrix} 1 & \beta^* & 0 \\ \beta & |\beta|^2 & 0 \\ 0 & 0 & 0 \end{bmatrix} + f_d \begin{bmatrix} |\alpha|^2 & \alpha & 0 \\ \alpha^* & 1 & 0 \\ 0 & 0 & 0 \end{bmatrix} + \frac{f_v}{4} \begin{bmatrix} 2 & 0 & 0 \\ 0 & 1 & 0 \\ 0 & 0 & 1 \end{bmatrix} + \frac{f_c}{2} \begin{bmatrix} 0 & 0 & 0 \\ 0 & 1 & \pm j \\ 0 & \mp j & 1 \end{bmatrix}$$

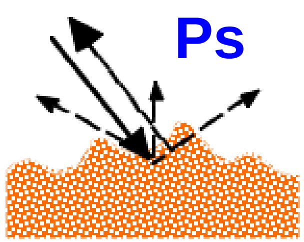

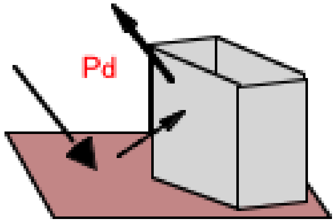

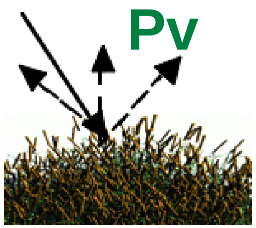

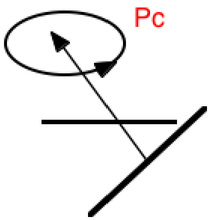

$$\langle [T] \rangle = \begin{bmatrix} T_{11} & T_{12} & T_{13} \\ T_{12}^* & T_{22} & T_{23} \\ T_{13}^* & T_{23}^* & T_{33} \end{bmatrix}$$

6 parameters out of 9 are counted in the expansion

3-component decomposition counts 5 out of 9 [Freeman and Durden Decomposition, FDD]

Y4R

How can be reduced the effects of the polarization orientation shifts from the decomposition results?

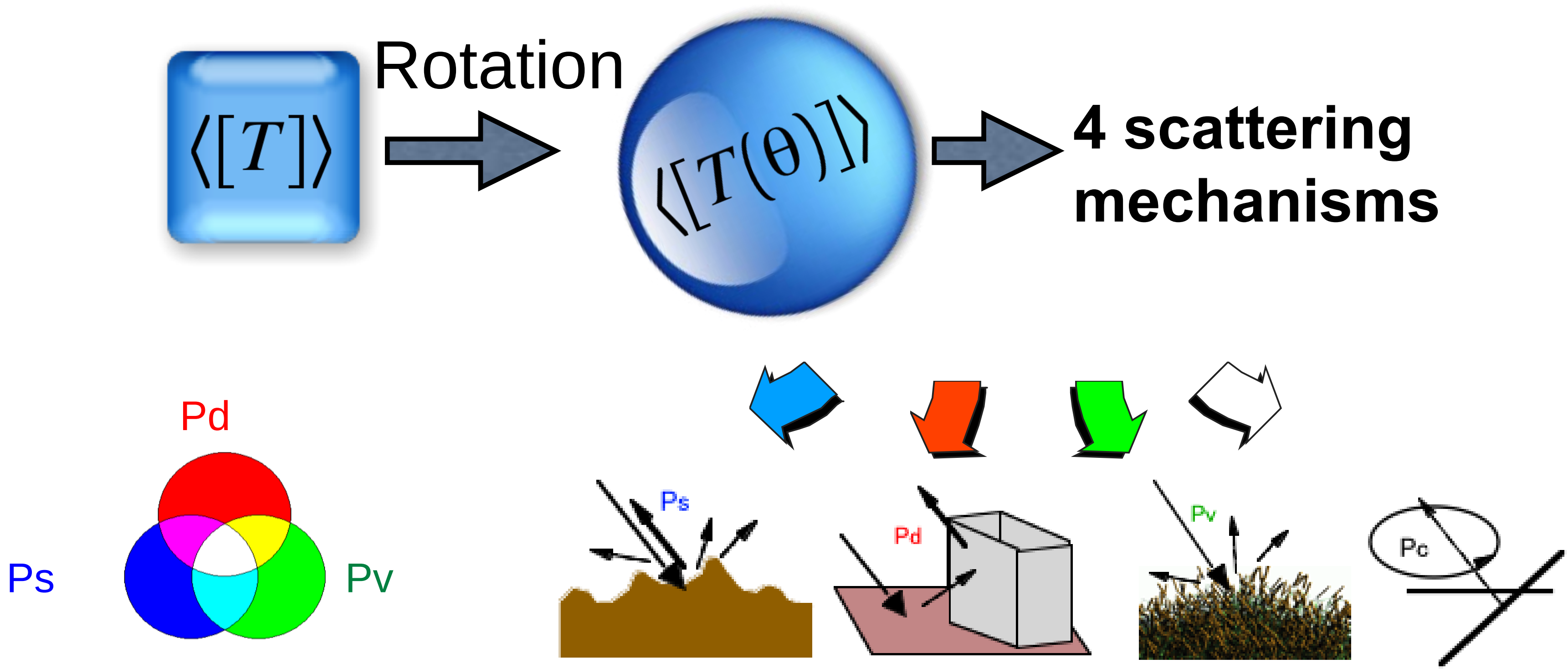

University of Illinois at Chicago

Electrical and Computer Engineering

Y4R

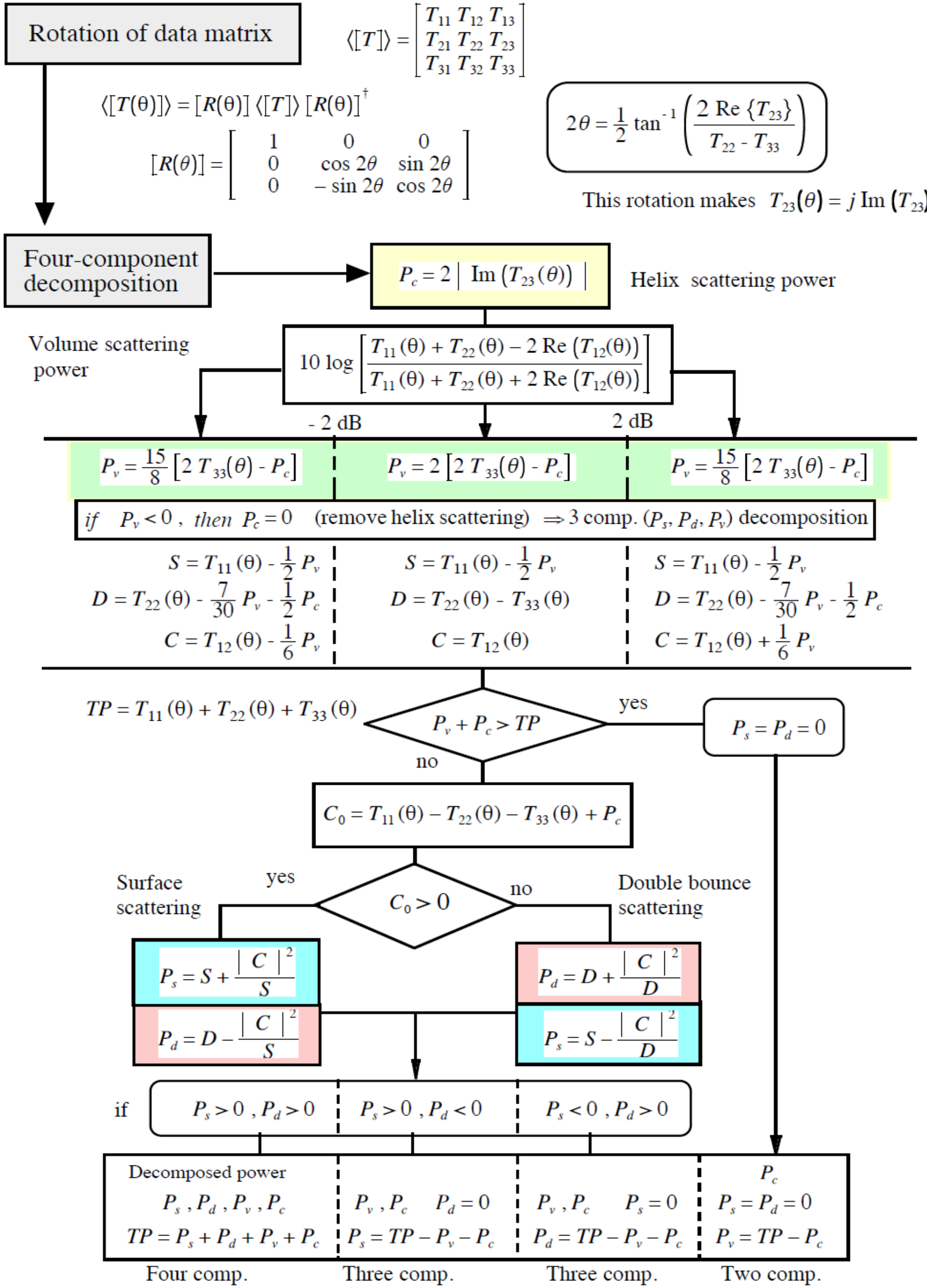

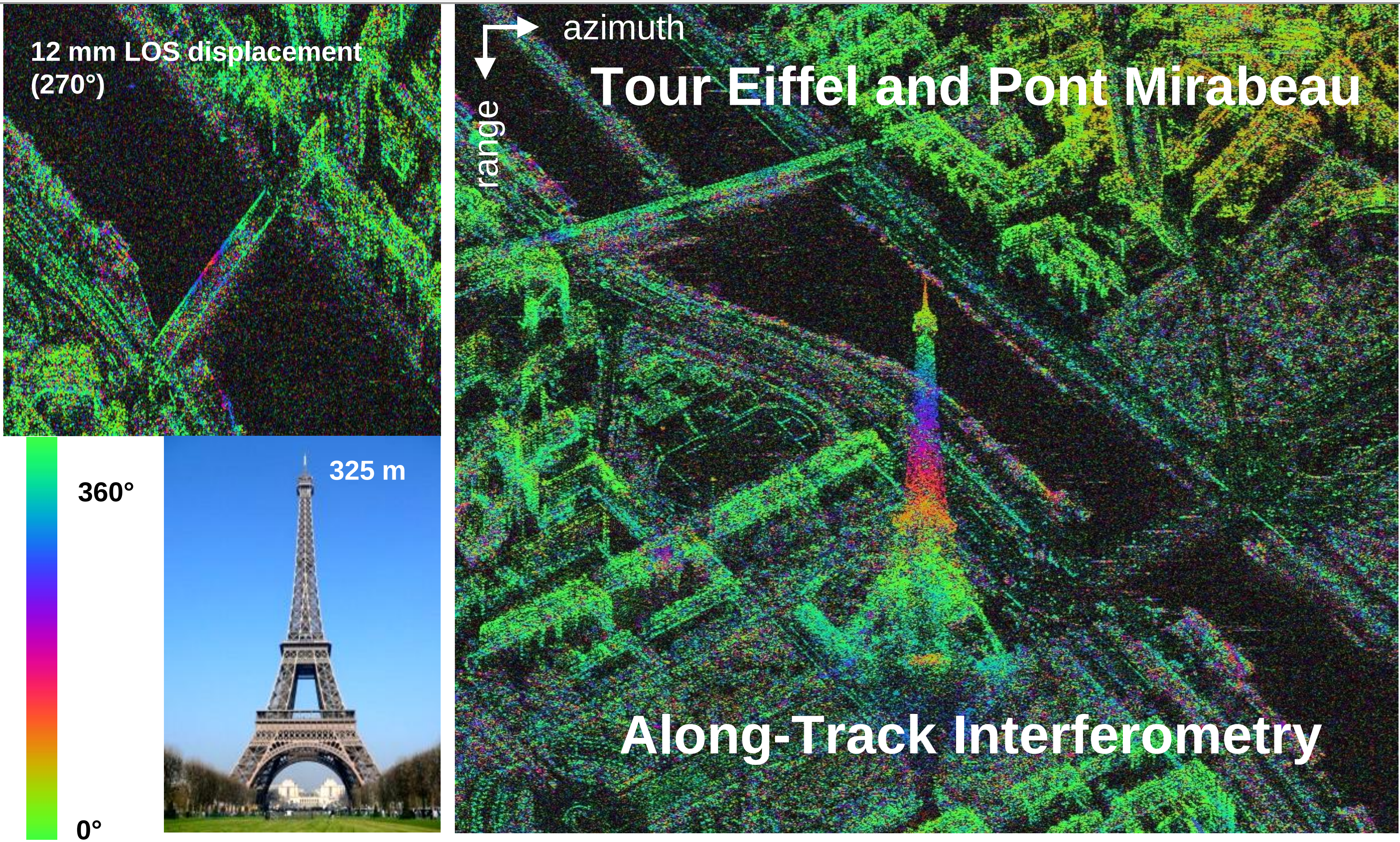
12 mm LOS displacement
(270°)
360°
0°
325 m
azimuth
range
Tour Eiffel and Pont Mirabeau
Along-Track Interferometry

4-component scattering power decomposition algorithm using rotated coherency matrix

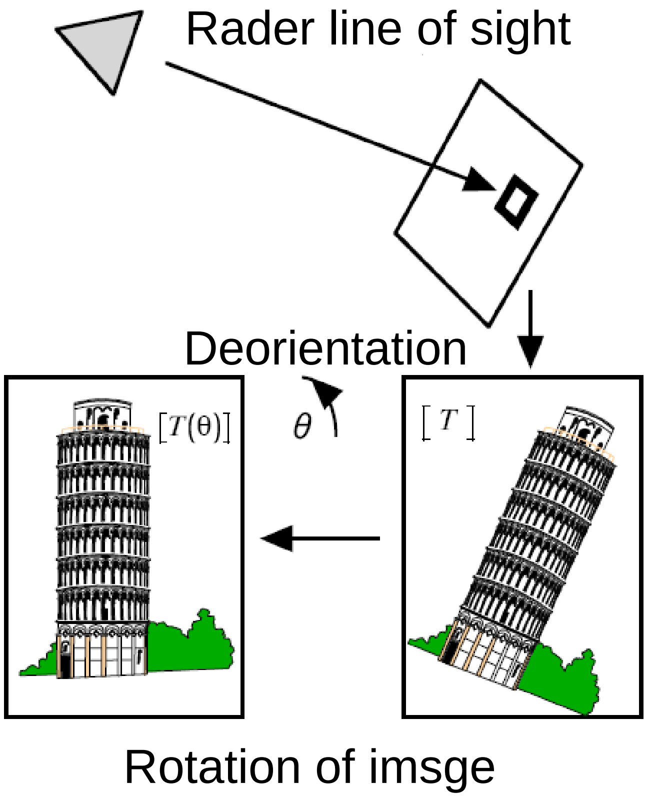

S4R

Volume scattering matrix for the HV component $\langle [T] \rangle = \int [T(\theta)]\, p(\theta)\, d\theta$

$[S] = \begin{bmatrix} 1 & 0 \\ 0 & 0 \end{bmatrix}, \begin{bmatrix} 0 & 0 \\ 0 & 1 \end{bmatrix}$

Re-polarization

De-polarization

HV from dipoles $\mathrm{Re}\,(S_{HH} S_{VV}^*) > 0$

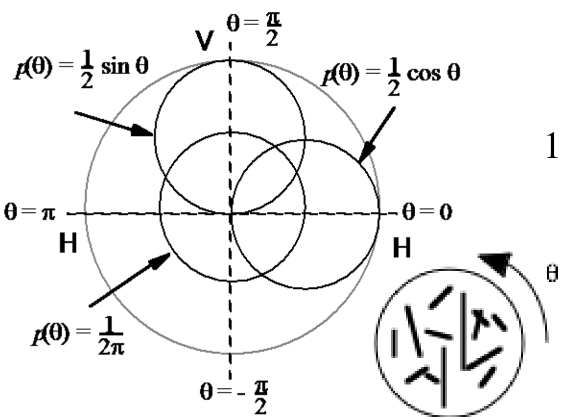

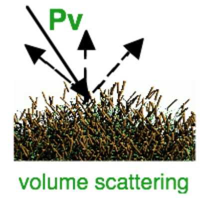

$10 \log \dfrac{\langle |S_{VV}|^2 \rangle}{\langle |S_{HH}|^2 \rangle}$: - 4 dB, - 2 dB, 0 dB, 2 dB, 4 dB

$$\langle [T] \rangle_{vol} = \frac{1}{30}\begin{bmatrix} 15 & 5 & 0 \\ 5 & 7 & 0 \\ 0 & 0 & 8 \end{bmatrix} \qquad \frac{1}{4}\begin{bmatrix} 2 & 0 & 0 \\ 0 & 1 & 0 \\ 0 & 0 & 1 \end{bmatrix} \qquad \frac{1}{30}\begin{bmatrix} 15 & -5 & 0 \\ -5 & 7 & 0 \\ 0 & 0 & 8 \end{bmatrix}$$

$$p(\theta) = \frac{1}{2}\sin\theta \qquad p(\theta) = \frac{1}{2\pi} \qquad p(\theta) = \frac{1}{2}\cos\theta$$

HV from oriented dihedrals $\mathrm{Re}\,(S_{HH} S_{VV}^*) < 0$

$[S] = \begin{bmatrix} 1 & 0 \\ 0 & -1 \end{bmatrix}$

$p(\theta) = \frac{1}{2}\cos\theta \quad \text{for} \quad -\frac{\pi}{2} < \theta < \frac{\pi}{2}$

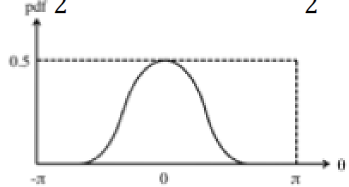

$$\frac{1}{15}\begin{bmatrix} 0 & 0 & 0 \\ 0 & 7 & 0 \\ 0 & 0 & 8 \end{bmatrix}$$

G4U

How can the complete Full-POLSAR information be utilised in decomposition models?

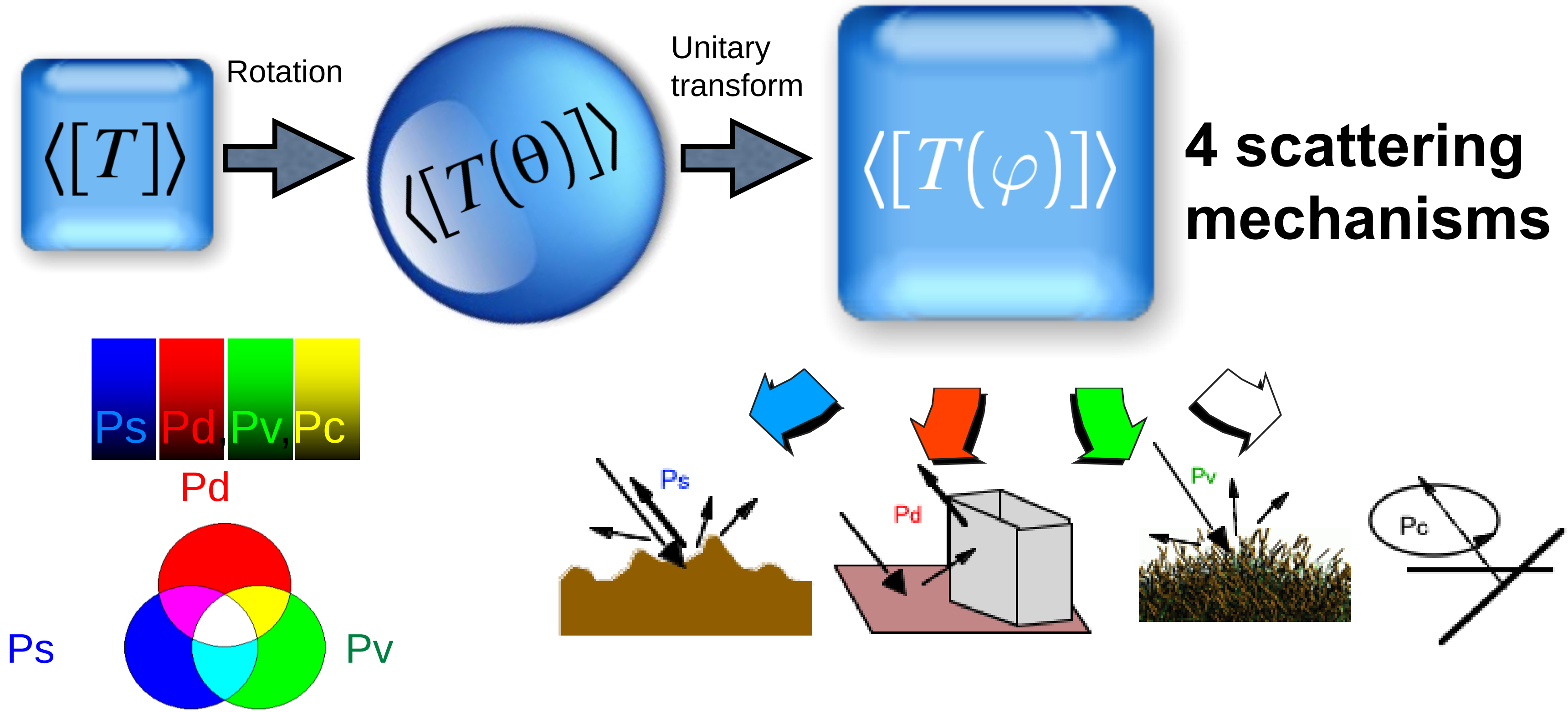

Gulab Singh, Y. Yamaguchi, and S.-E. Park, "General four-component scattering power decomposition with unitary transformation of coherency matrix," *IEEE Trans. Geoscie. Remote Sens.*, vol., no. , pp., Sept. 2012. online available

ni

G4U

HV from dipoles and dihedrals

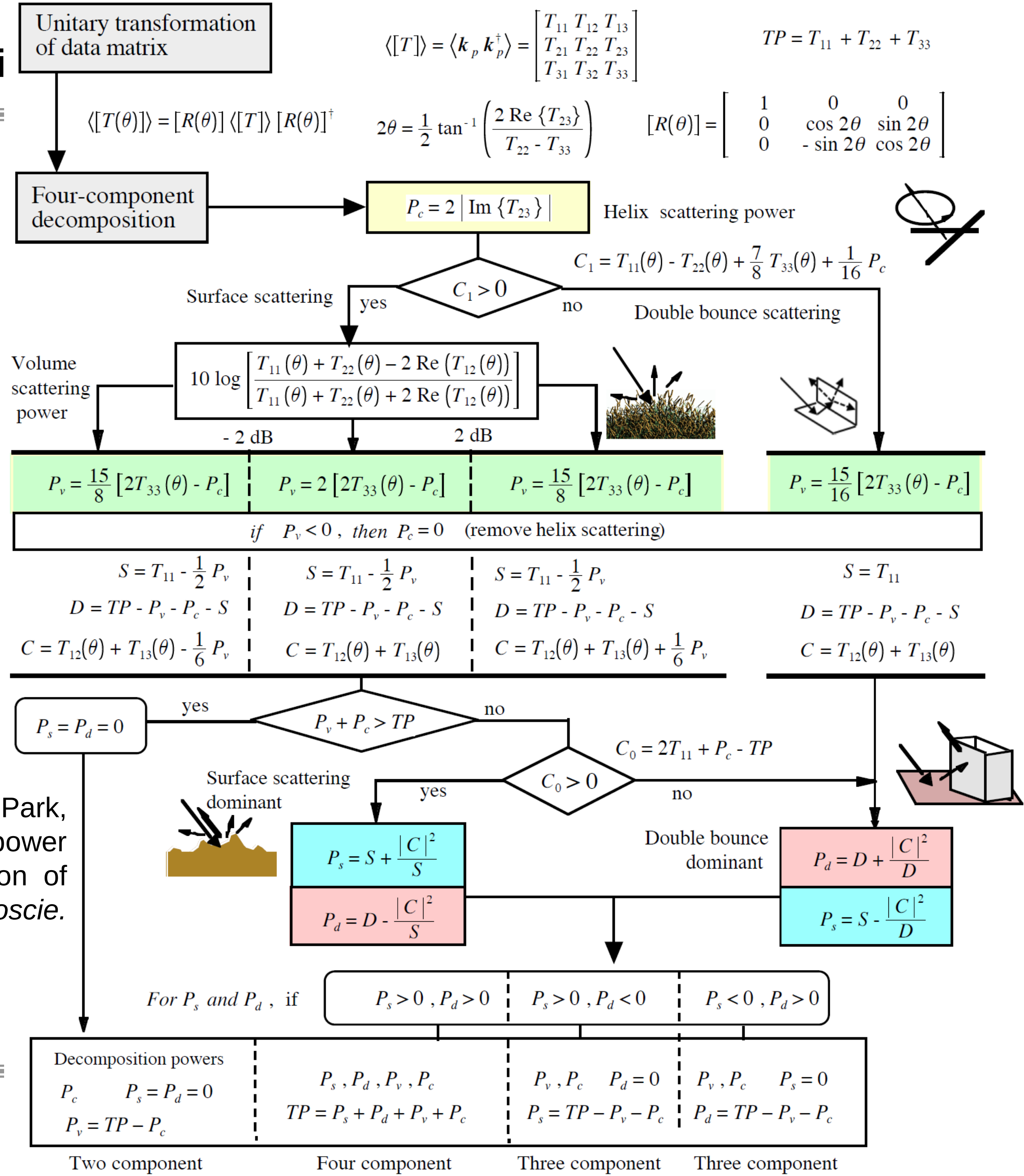

Gulab Singh, Y. Yamaguchi, and S.-E. Park, "General four-component scattering power decomposition with unitary transformation of coherency matrix," *IEEE Trans. Geoscie. Remote Sens.*, ***(in press)***

Four-component decomposition

New rotated decomposition

Scattering power decomposition by rotation of coherency matrix for Niigata City area in Niigata Prefecture of Japan

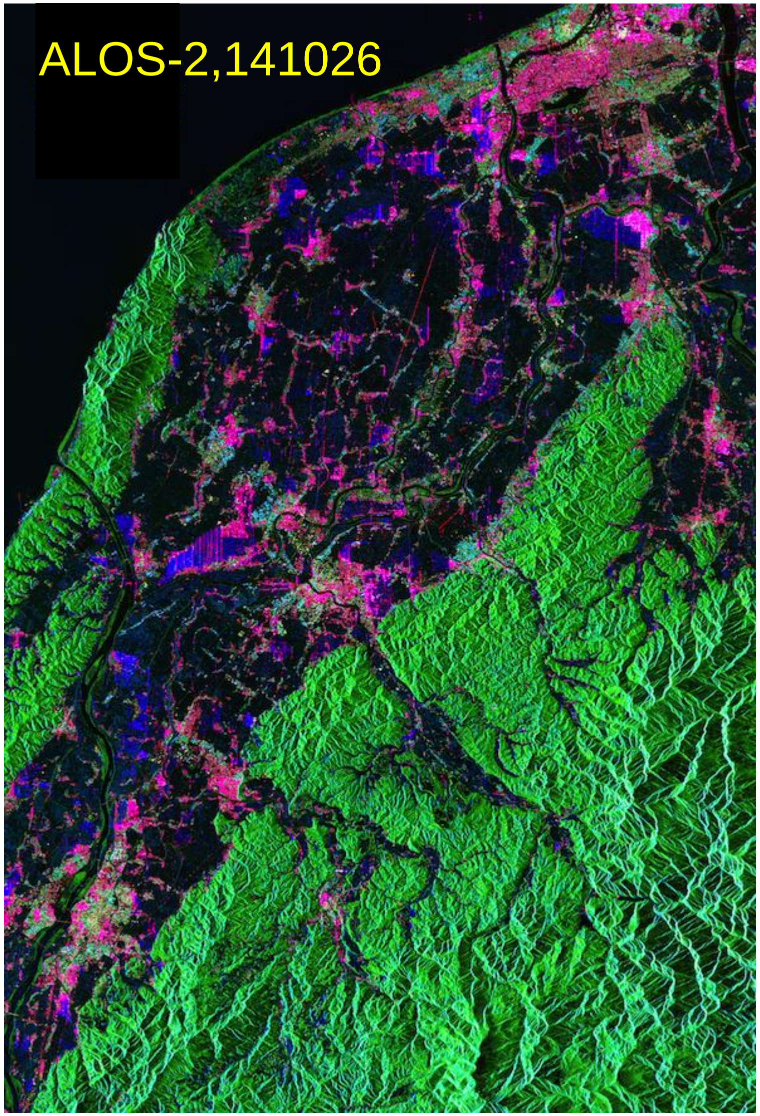

Quad-Pol
G4U

Yoshio Yamaguchi
&
Gulab Singh

2014 Dec. 10

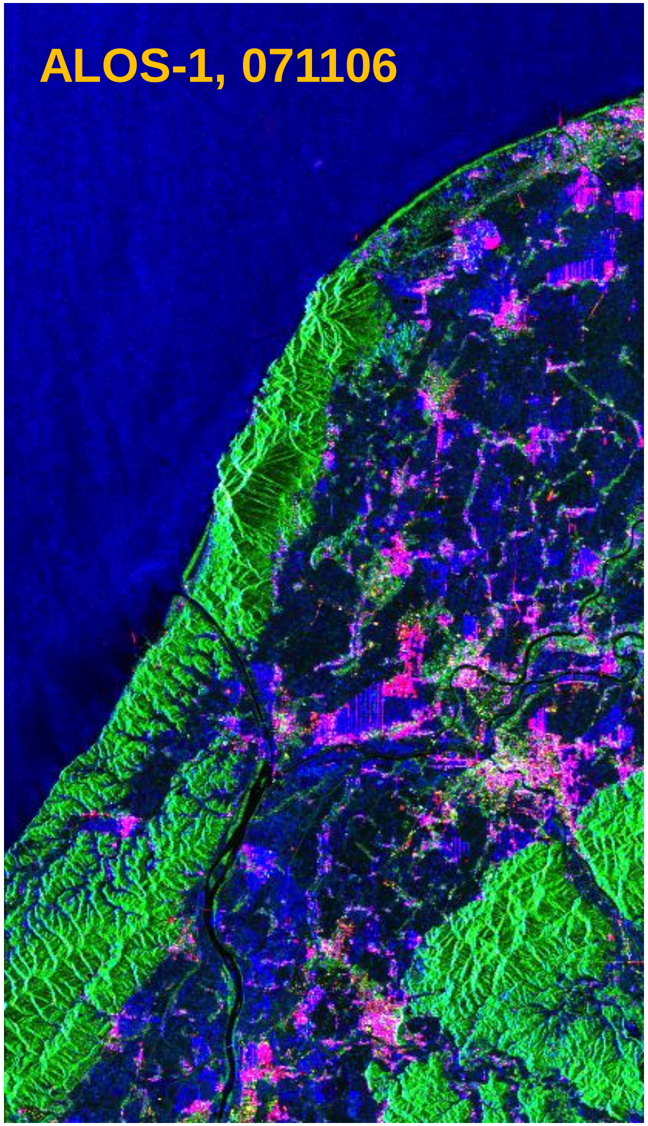

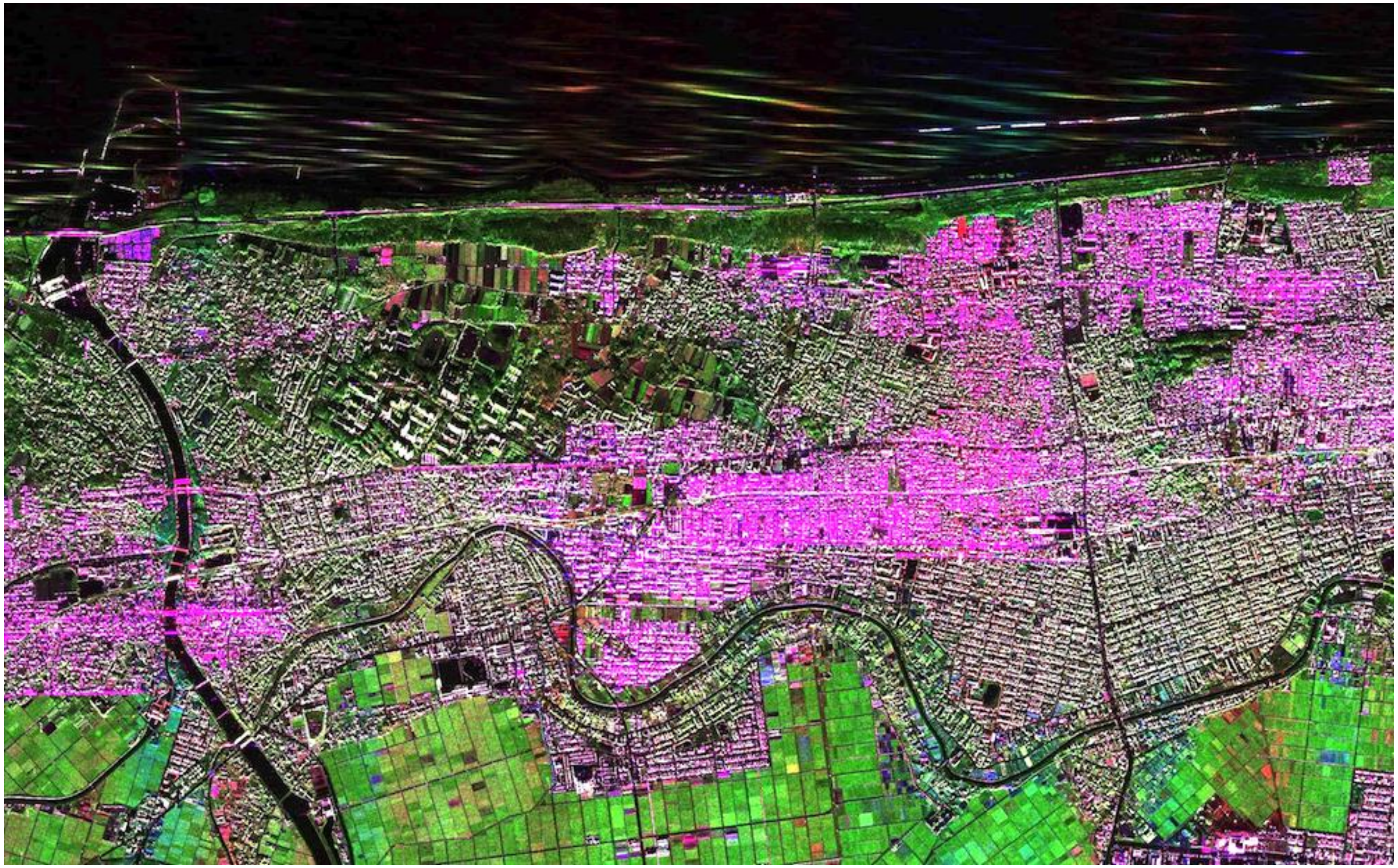

G4U   Rotated four component decomposition GU4/Yamaguchi

PART-III POLSAR Applications for environmental remote sensing and geophysical hazard detection and subsequent disaster assessment

9. Application to environmental remote sensing in agriculture, forestry & aquaculture\
10. Application to earthquake detection and damage assessment
11. Application to volcano eruption assessment
12. Application to Tsunami detection and disaster assessment
13. Application to Mega-cyclone disaster assessment

Monitoring of surface deformations using differential SAR interferometry and Polarimetry

- Application to Earthquake Detection
- Application to Volcano Eruption
- Application to Tsunami Detection and Disaster Assessment
- Application to Mega-Cyclone Disaster Assessment

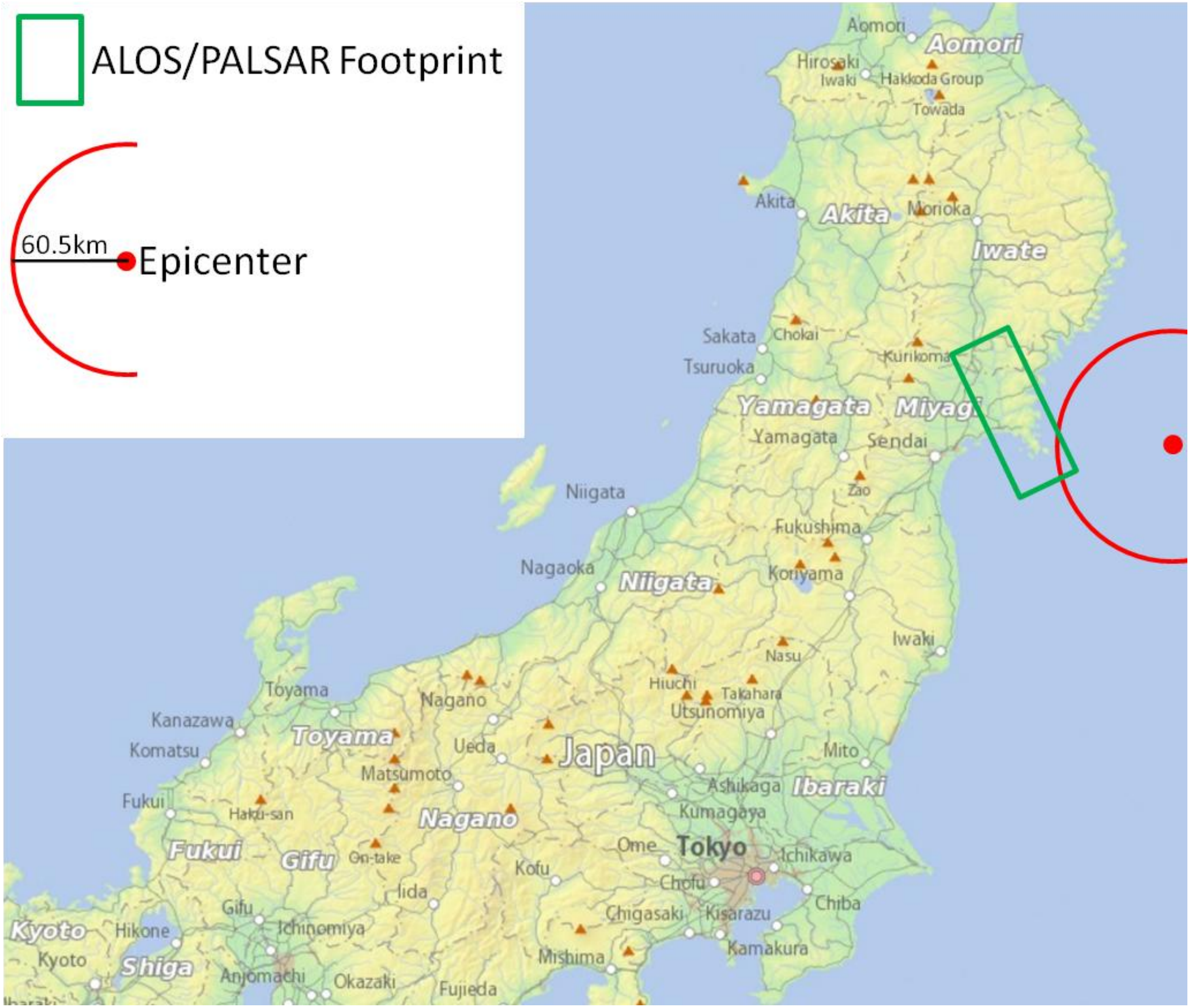

Off-Tohoku 9.0 Earthquake with Super-Tsunami

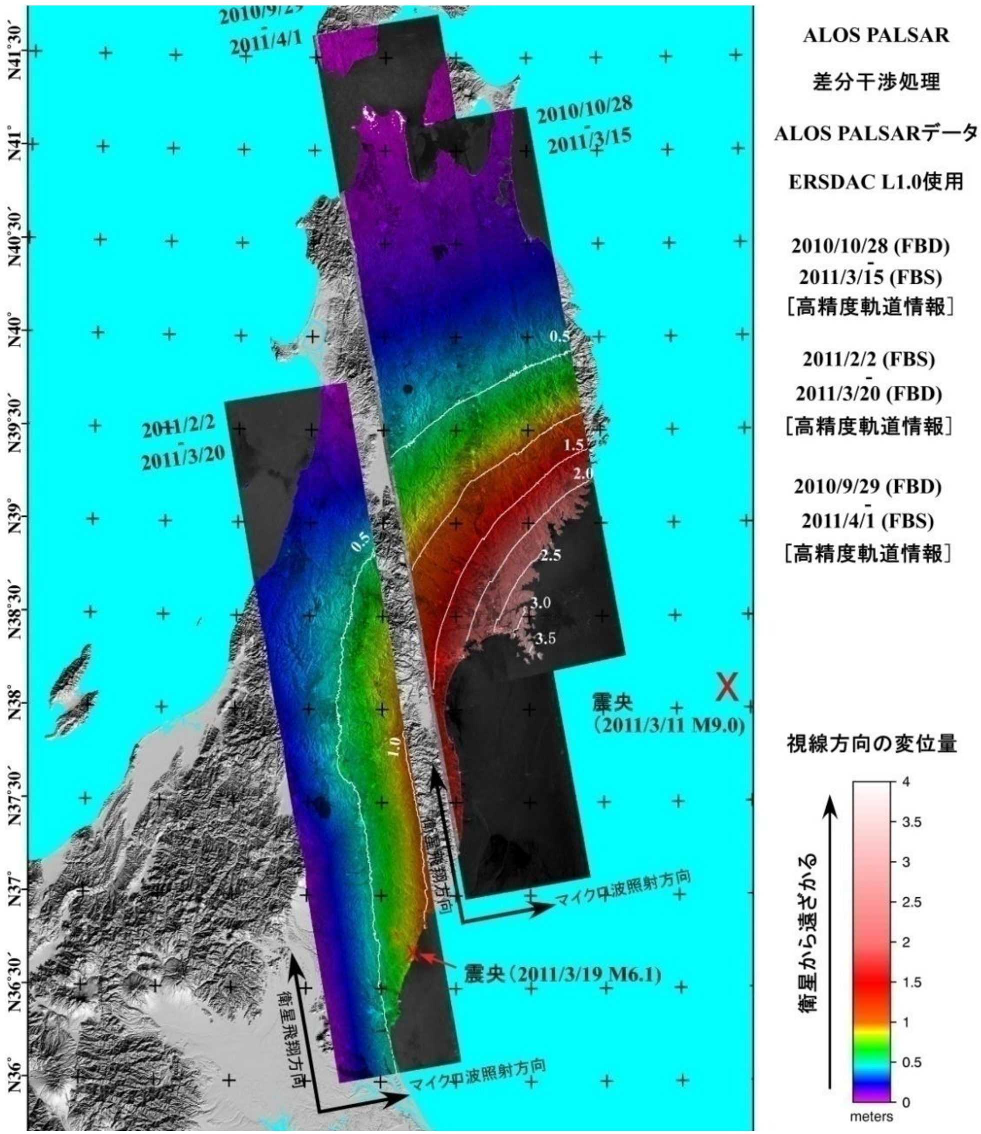
ALOS PALSAR
差分干渉処理
ALOS PALSARデータ
ERSDAC L1.0使用
2010/10/28 (FBD)
-
2011/3/15 (FBS)
[高精度軌道情報]
2011/2/2 (FBS)
-
2011/3/20 (FBD)
[高精度軌道情報]
2010/9/29 (FBD)
-
2011/4/1 (FBS)
[高精度軌道情報]
震央
(2011/3/11 M9.0)
震央（2011/3/19 M6.1）
視線方向の変位量
衛星から遠ざかる
meters
マイクロ波照射方向
衛星飛翔方向

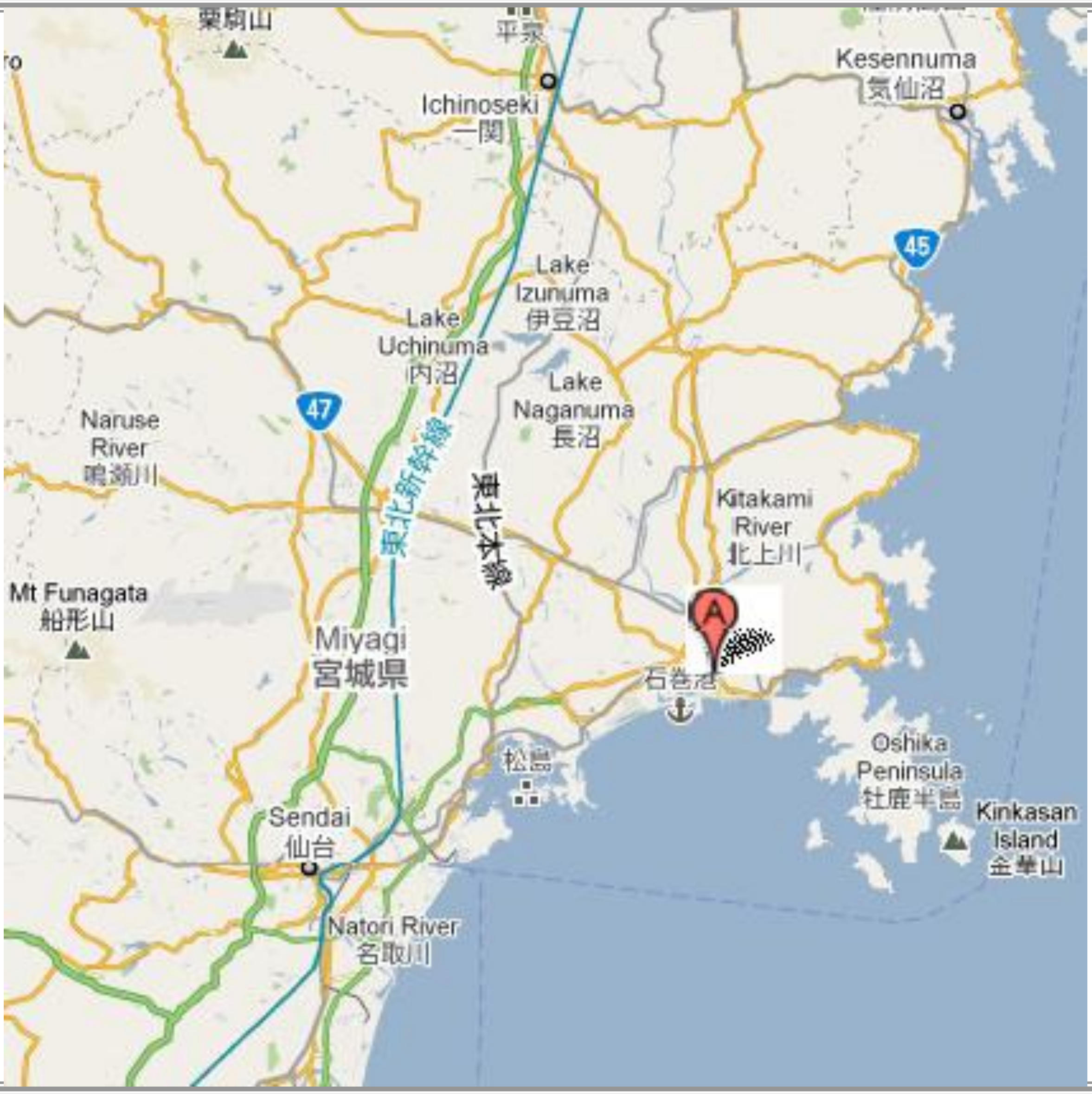

Ishinomaki harbor
38*25’N, 141*18’E

Destruction of City and Harbor of Ishinomaki by 110311 Tsu-nami (Harbor-Wave)


Before
Ishinomaki
Matsushima Air Field
After

Off-Tohoku M9 Seaquake & Tsunami 110311

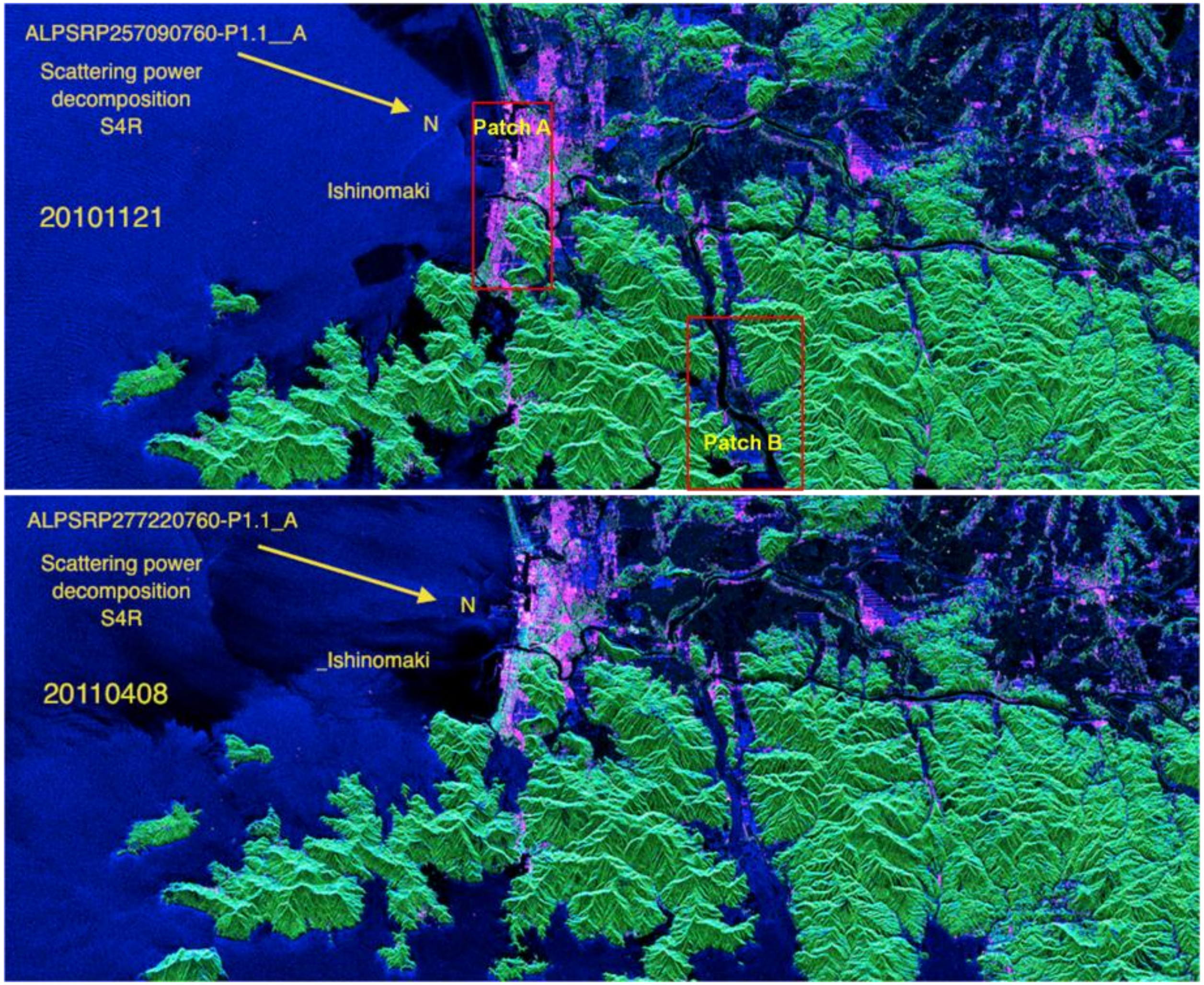

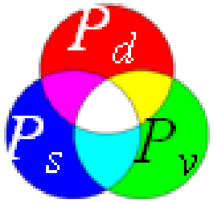

Off-Tohoku M9 Seaquake & Tsunami 110311

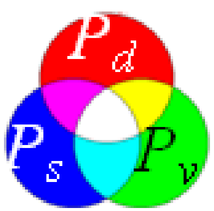

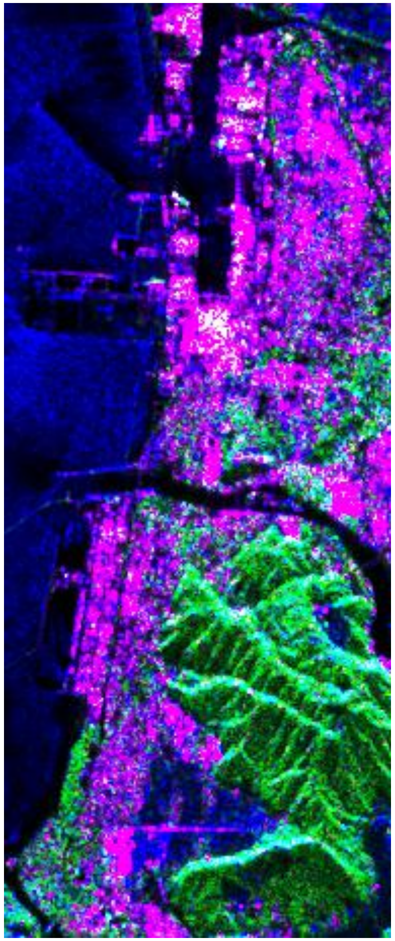

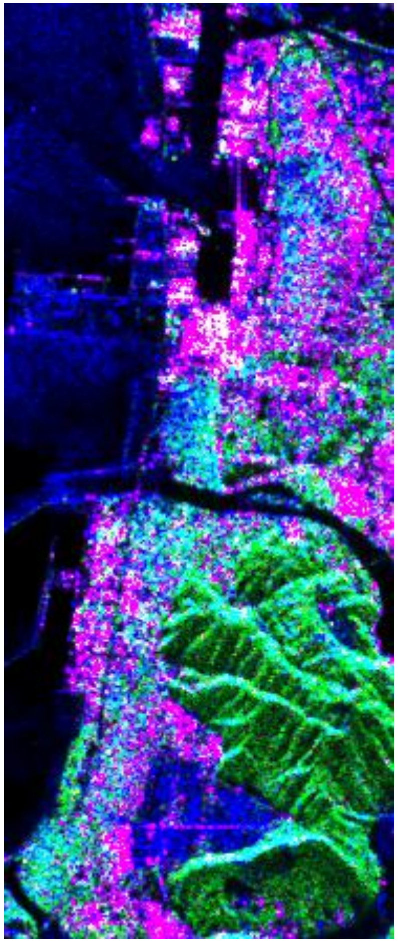

collapsed by tsunami

covered by tsunami

Off-Tohoku M9 Seaquake & Tsunami 110311

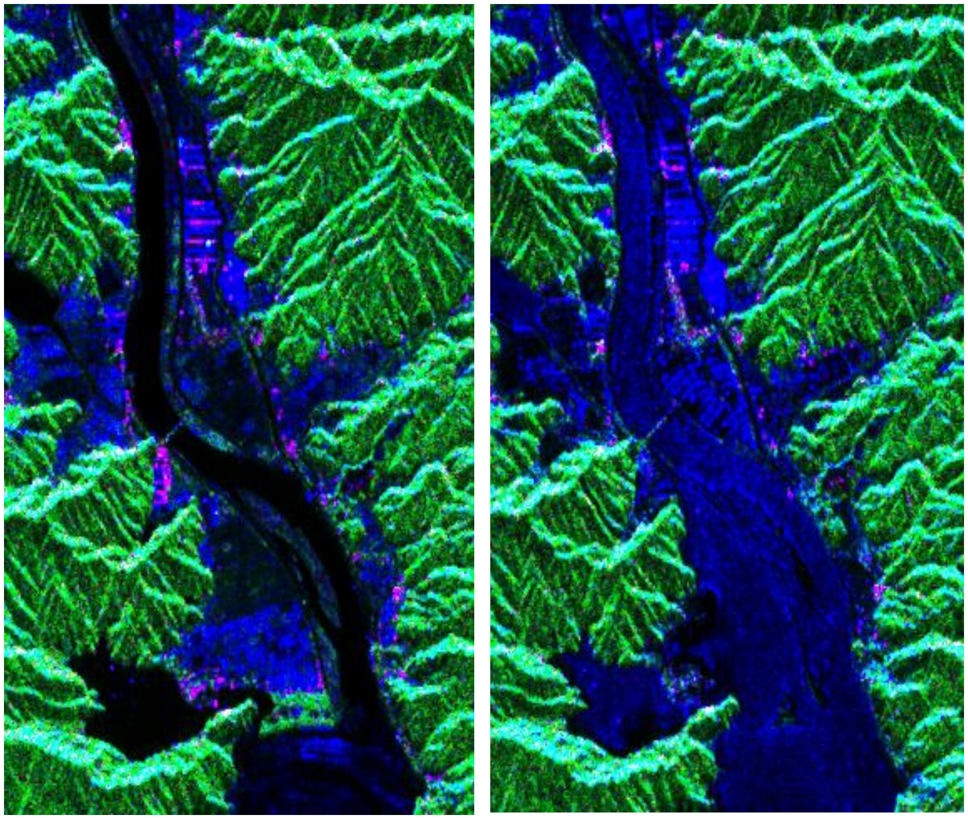

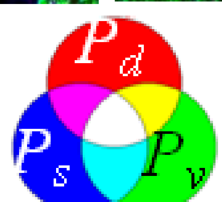

collapsed by tsunami

covered by tsunami

ALOS-PALSAR Polarimteric Mode

Ascending

Indonesia

2007/3/10

Data no.
ALPSRP059887030
ALPSRP059887040

2009/3/15

Data no.
ALPSRP167247030
ALPSRP167247040

Yoshio Yamaguchi
Niigata University

Indonesia

−7.942N
112.870E

2007/3/10

ALPSRP059887030-P1.1__A

Scattering power Decomposition

Pd

Ps

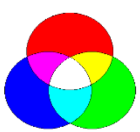

Pv

Niigata University

Google earth optical image

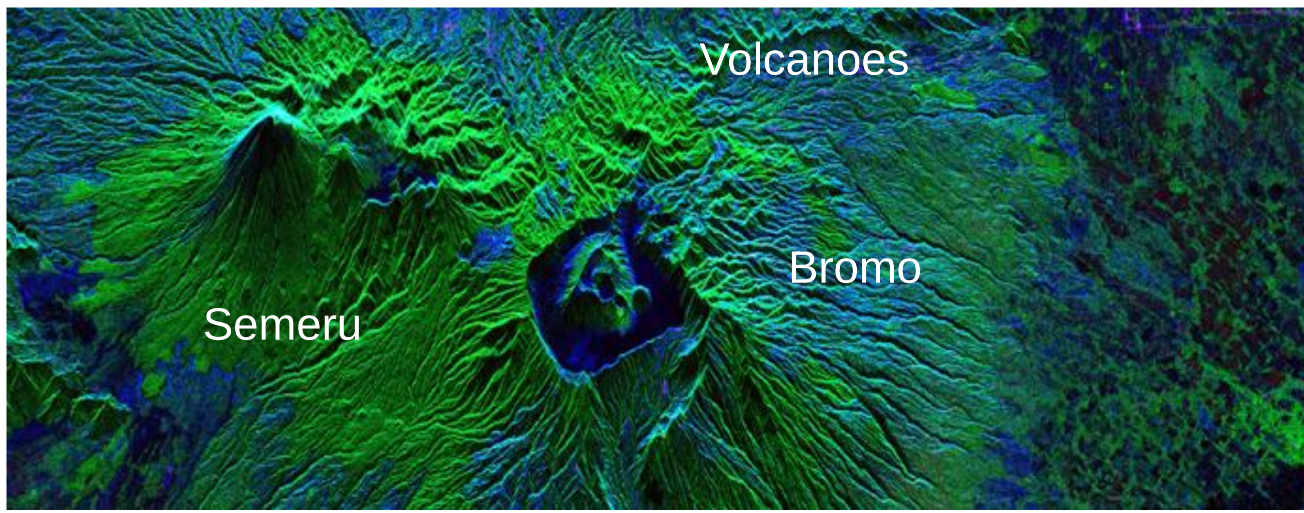

Decomposed image (Ps, Pd, Pv)

Mount Semeru puffs steam behind a cloud of sulphur gas from Mount Bromo in the Tengger caldera on Java.

Niigata University

2007/3/10 **Y4O**
-7.942N
112.870E
Indonesia

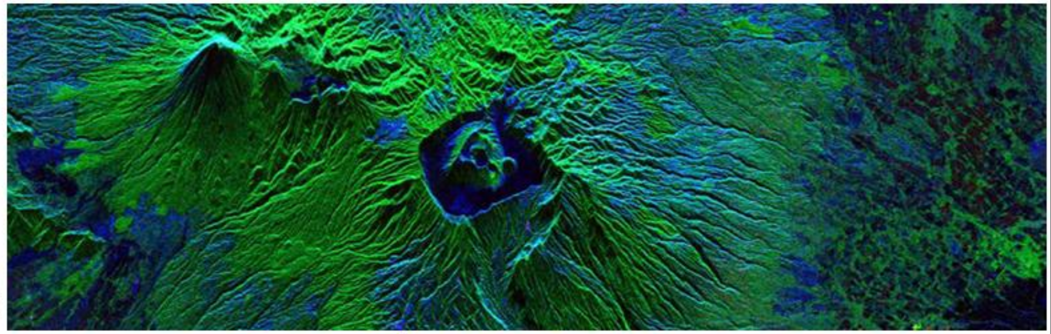

Pd, Pv, Ps

Pauli-basis

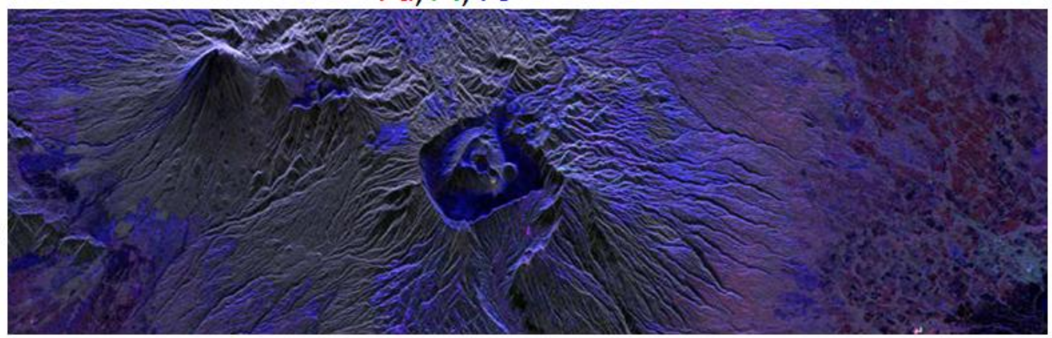

HH-VV, 2HV, HH+VV

HV-basis
(HH,2HV,VV)

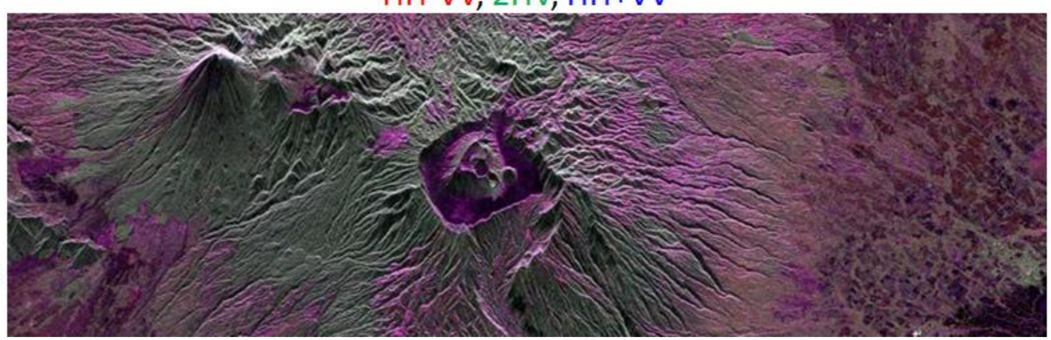

ALPSRP059887030-P1.1__A

Y4R

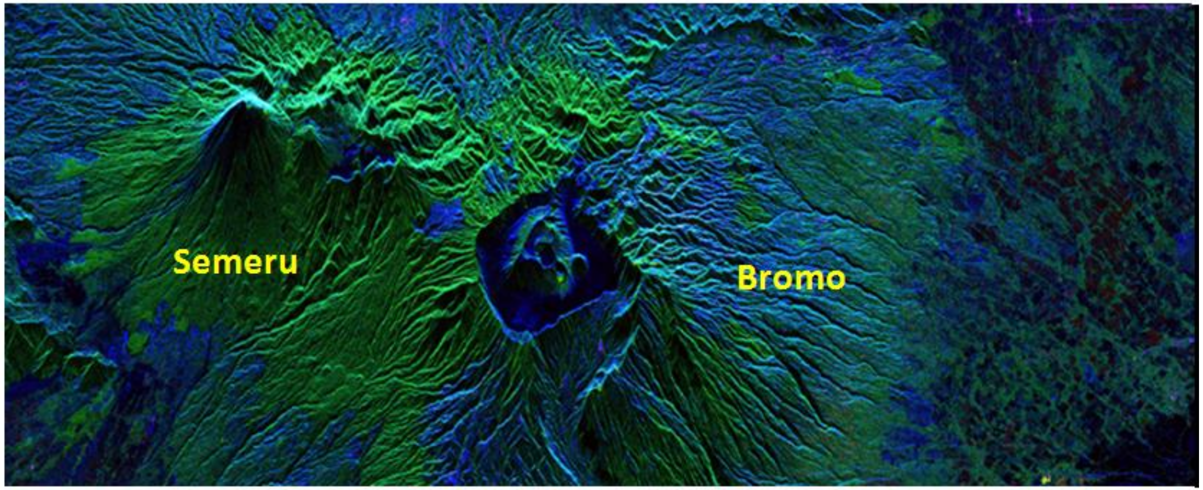

G4U

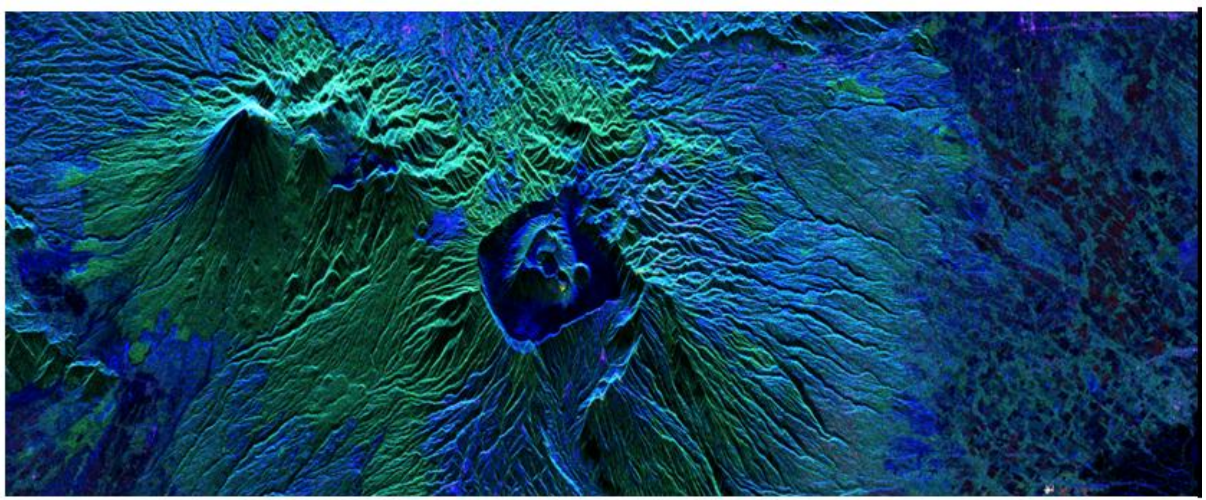

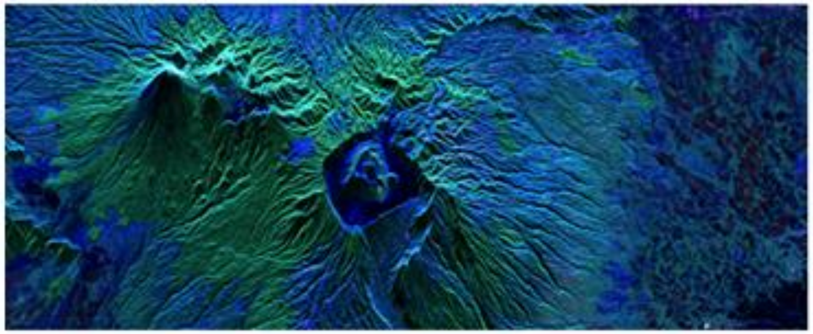

G4U

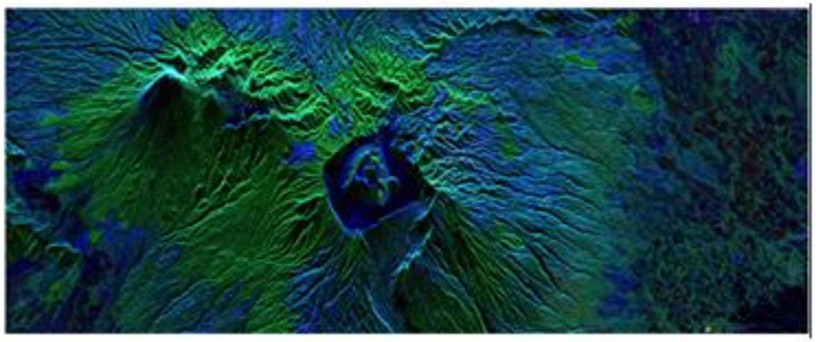

Y4R

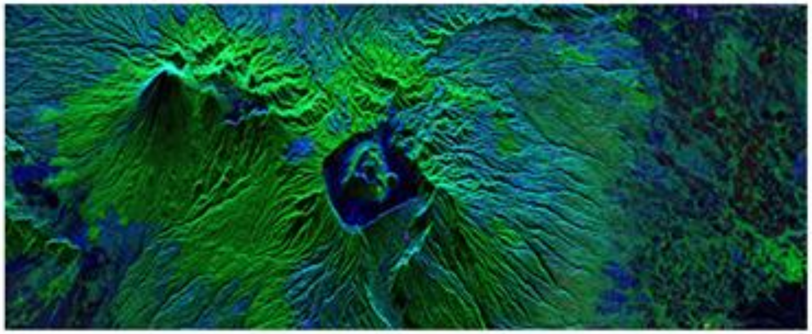

Y4O

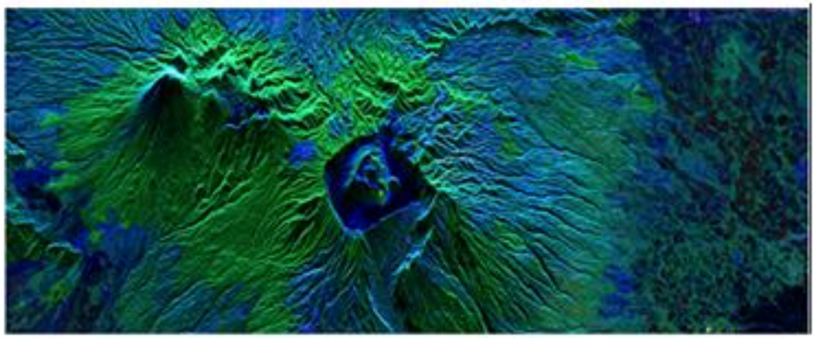

Y4R4C

Comparison of YAMAGUCHI & Gulab SINGH Decompositions

Mt. Merapi

7.400S
110.464E

ALPSRP262863760-P1.1__D

Google Earth Optical Image

N

2010/12/31

Polarimetric scattering power decomposition

Ps Pd Pv Pc

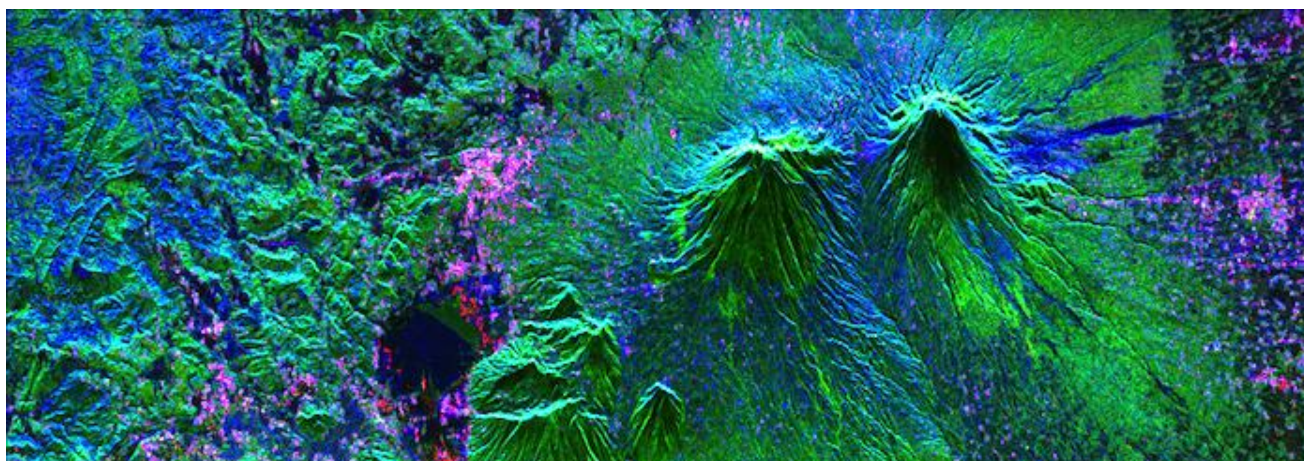

Scattering Power Decomposition G4U with 3x18 pixels

MERAPI Volcano viewed from Main Boulevard of UGM in YOGYAKARTA, JAVA/INDONESIA

Gunung Merbabu
&
Gunung Merapi

Y4R

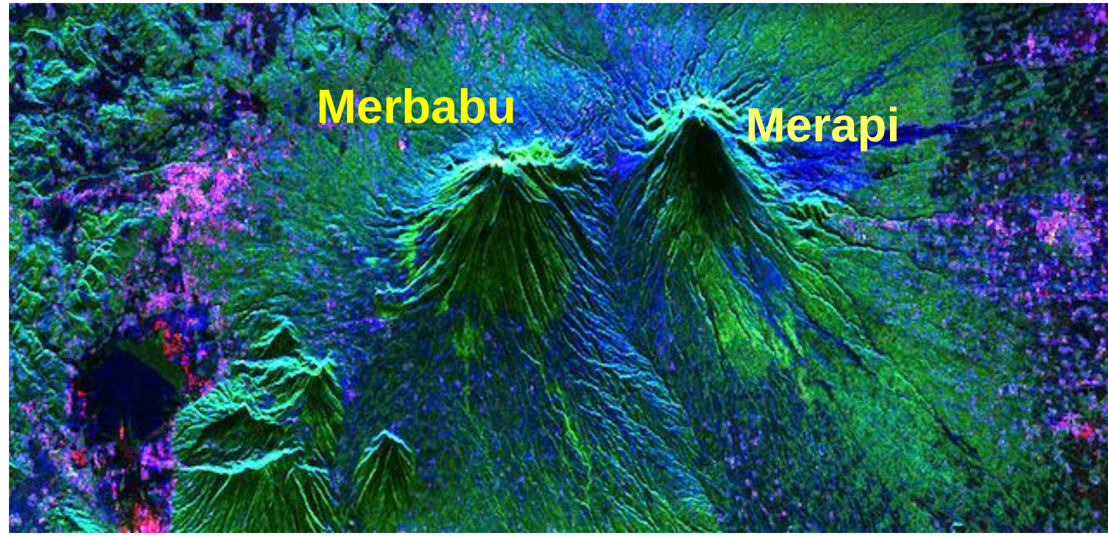

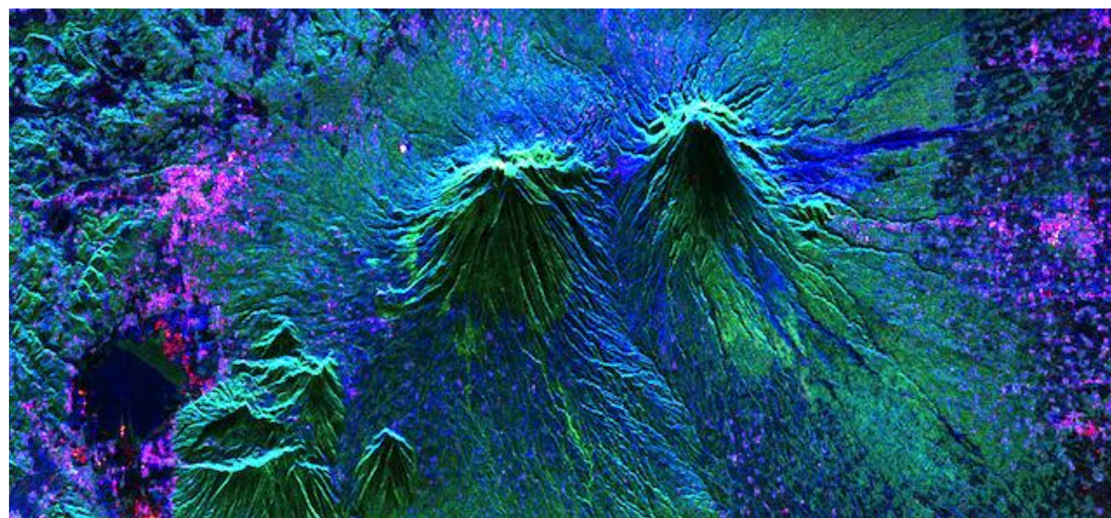

G4U

Pd

Ps

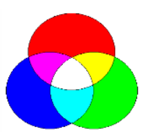

Pv

Niigata University

Tsunami Physics

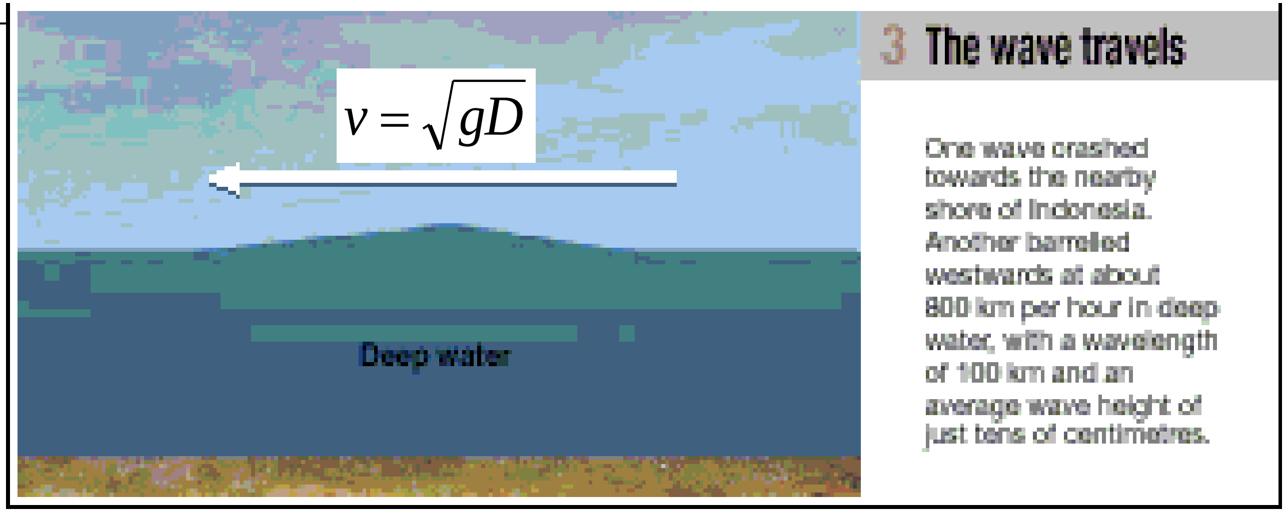

20 cm

100 km

800 km/h

[Nature, January 2005]

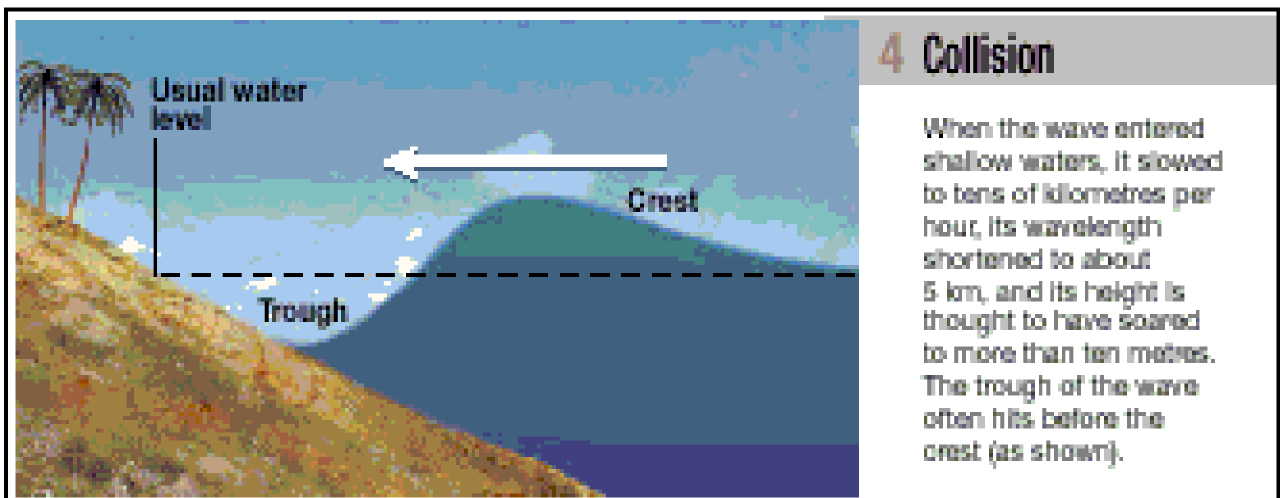

4 m

5 km

60 km/h

Tsunami Physics

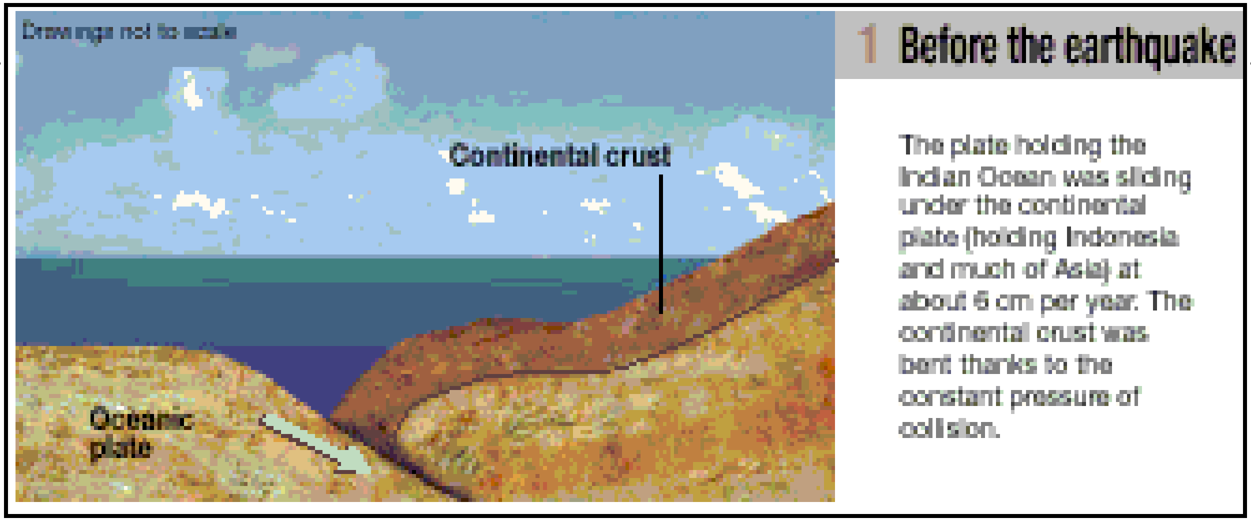

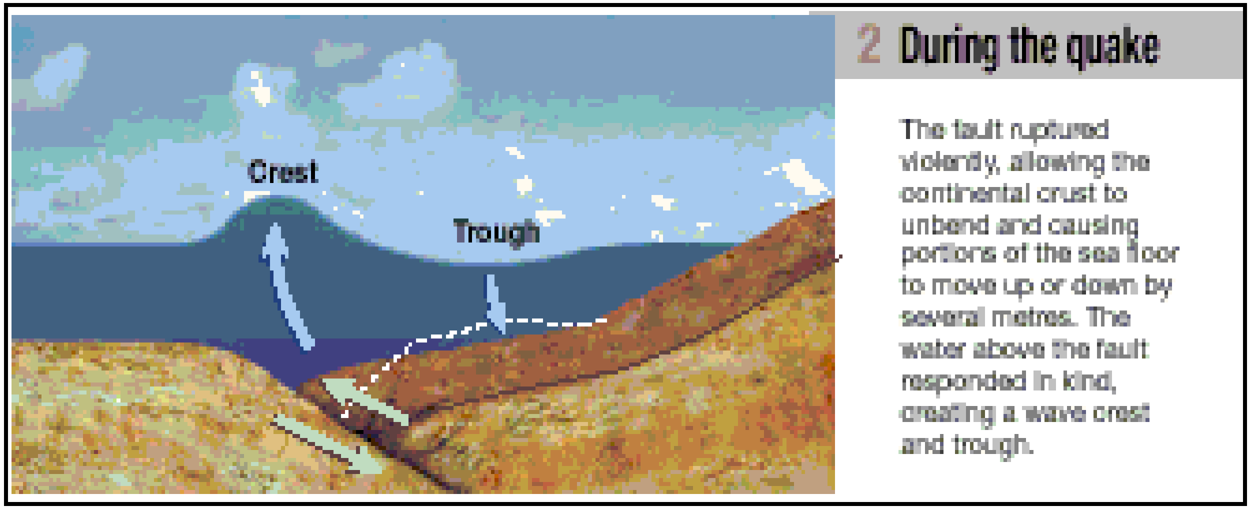

[Nature, January 2005]

Tsunami Wave Appearance

Source: www.waveofdestruction.org

- A tsunami wave crest has three general appearances from shore:
  - Fast-rising tide
  - Cresting wave
  - A step-like change in the water level that advances rapidly (called a bore)

- Series of waves
  - Most tsunamis come in a series of waves that may last for several hours
  - The outflow of water back to the sea between waves can cause more damage than the original incoming wave fronts
  - The first wave is rarely the largest

North-East Indian Ocean Tsunami, 2004 December 26

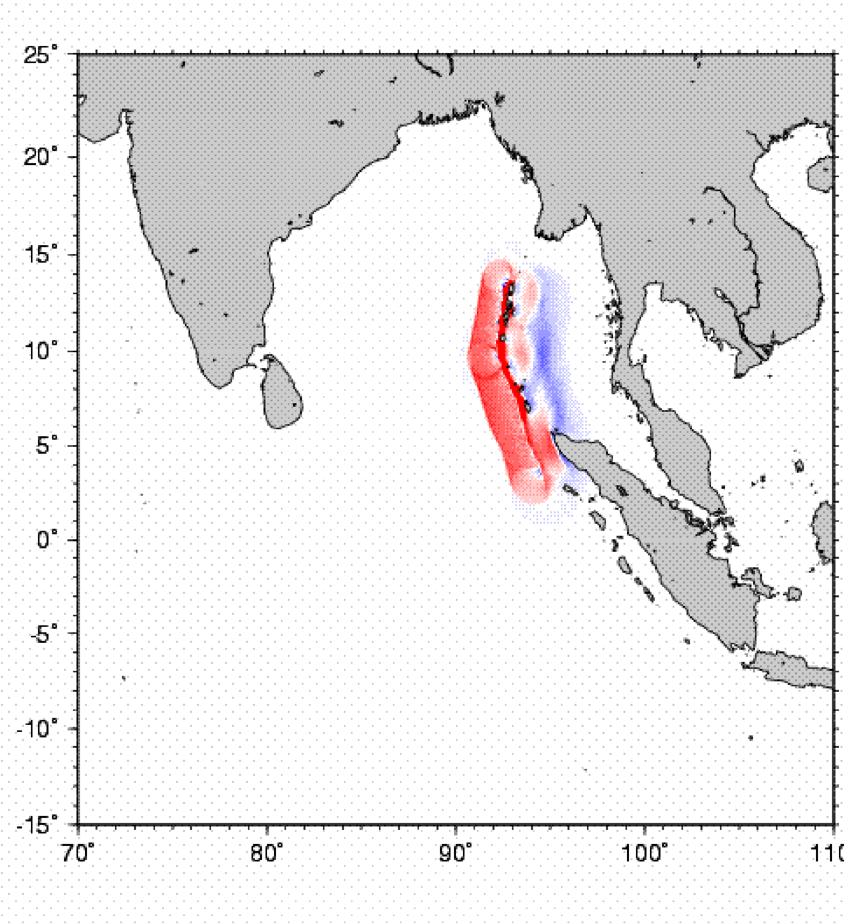

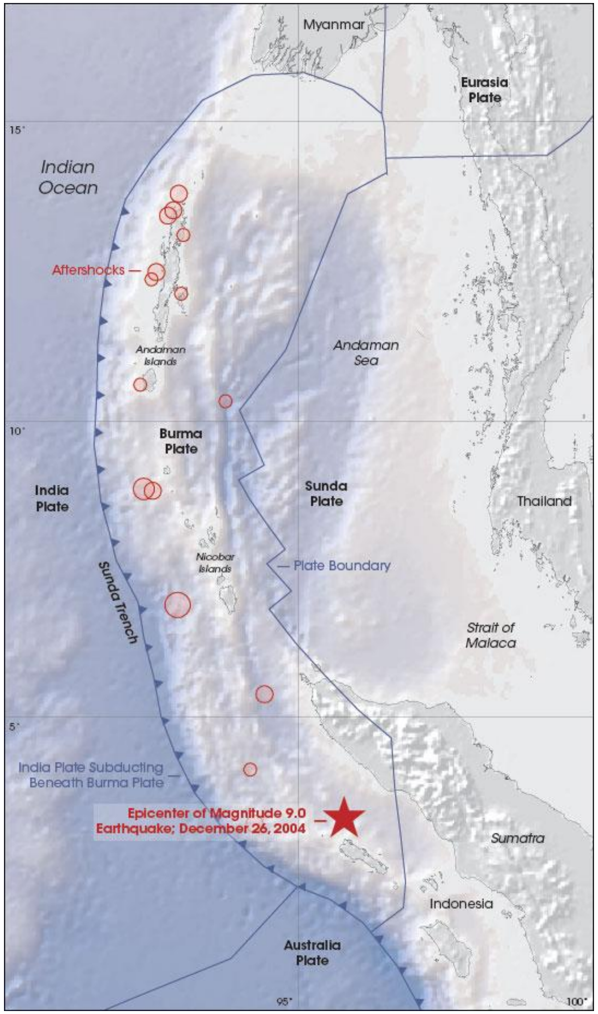

"Natural hazards are inevitable.
Natural disasters are not."

ALOS-PALSAR Polarimteric Mode: 2007 ~ 2010

Ascending

Indonesia

2007/3/10

Data no.
ALPSRP059887030
ALPSRP059887040

2009/3/15

Data no.
ALPSRP167247030
ALPSRP167247040

Yoshio Yamaguchi

Niigata University

Indian Ocean Tsunamis: 1833 & 2004

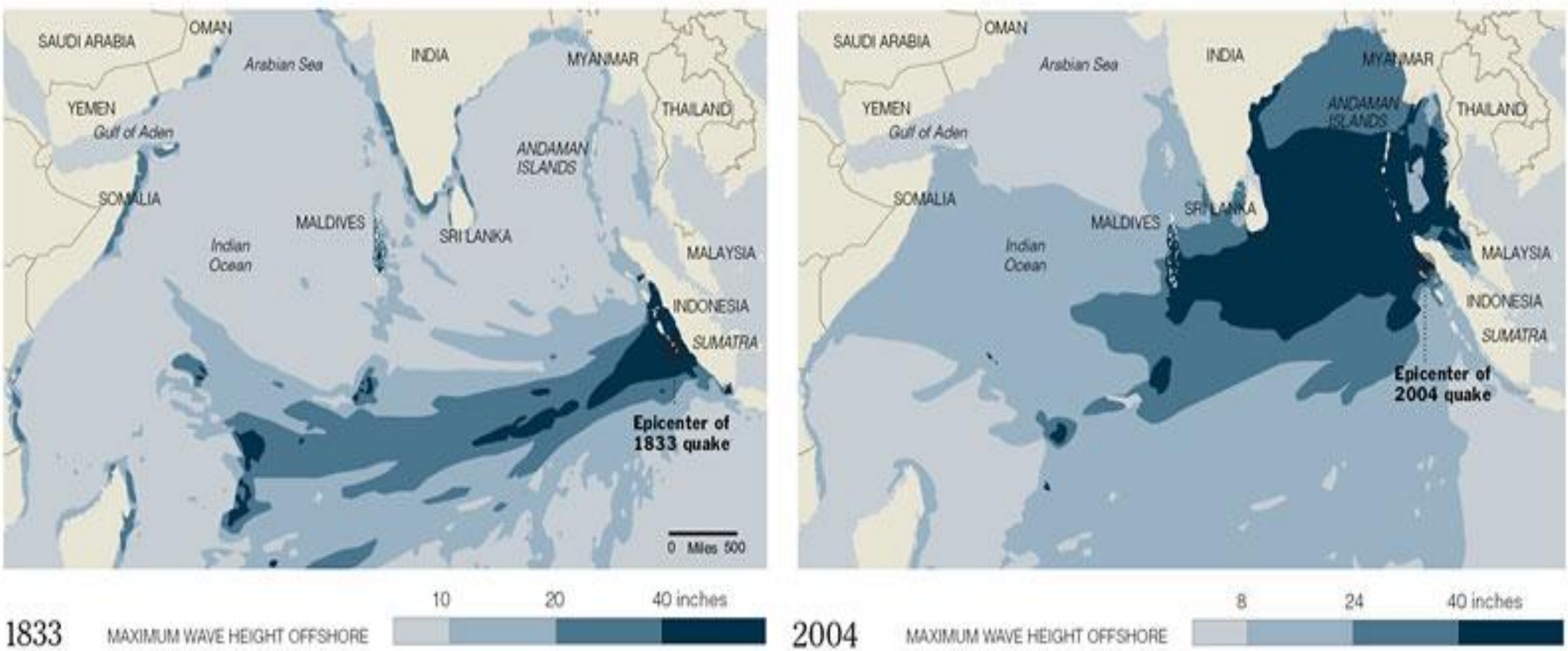

Hannah Fairfield/The New York Times, Science Section, January 4, 2005

The 26-Dec-2004 Tsunami

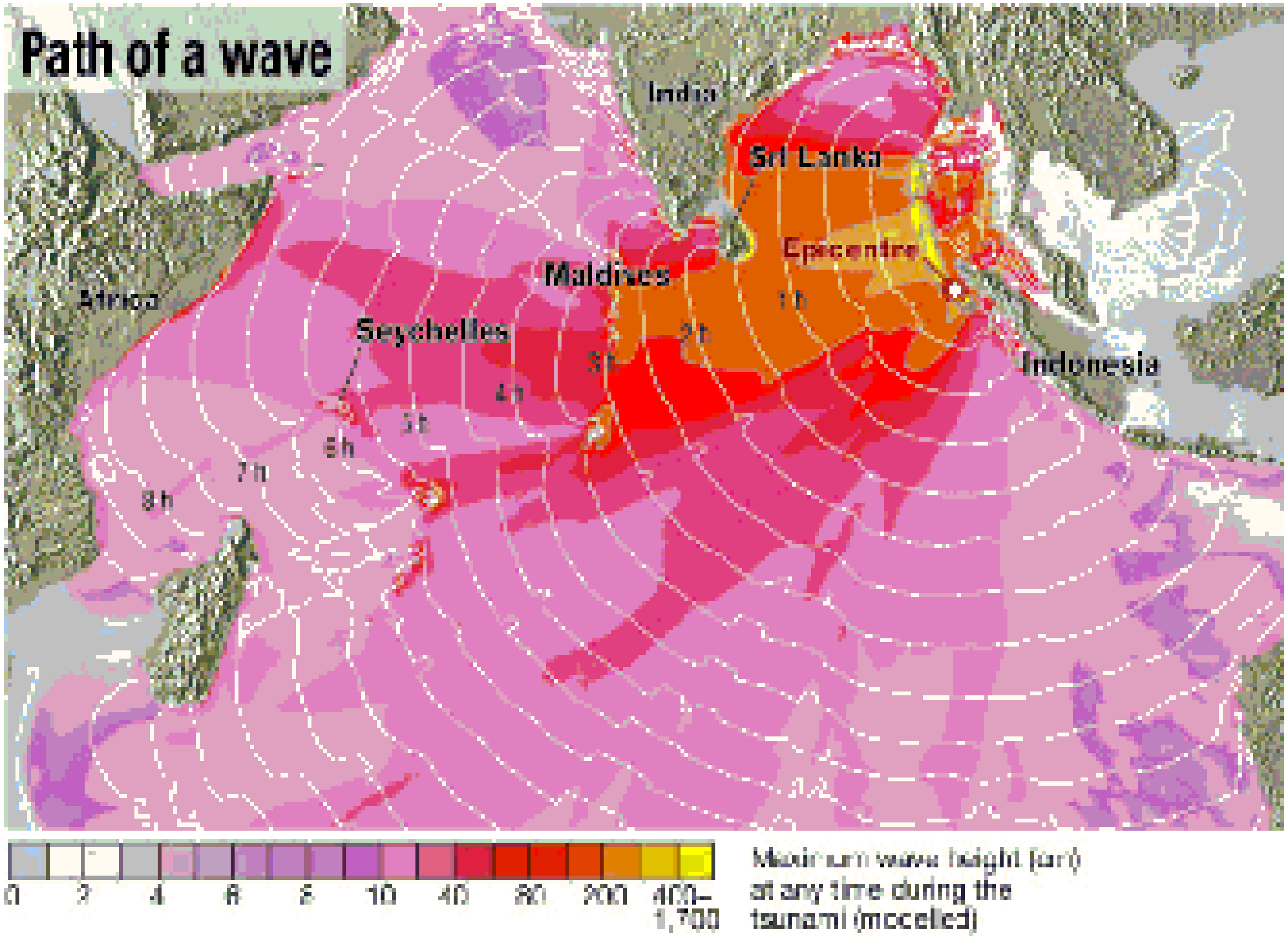

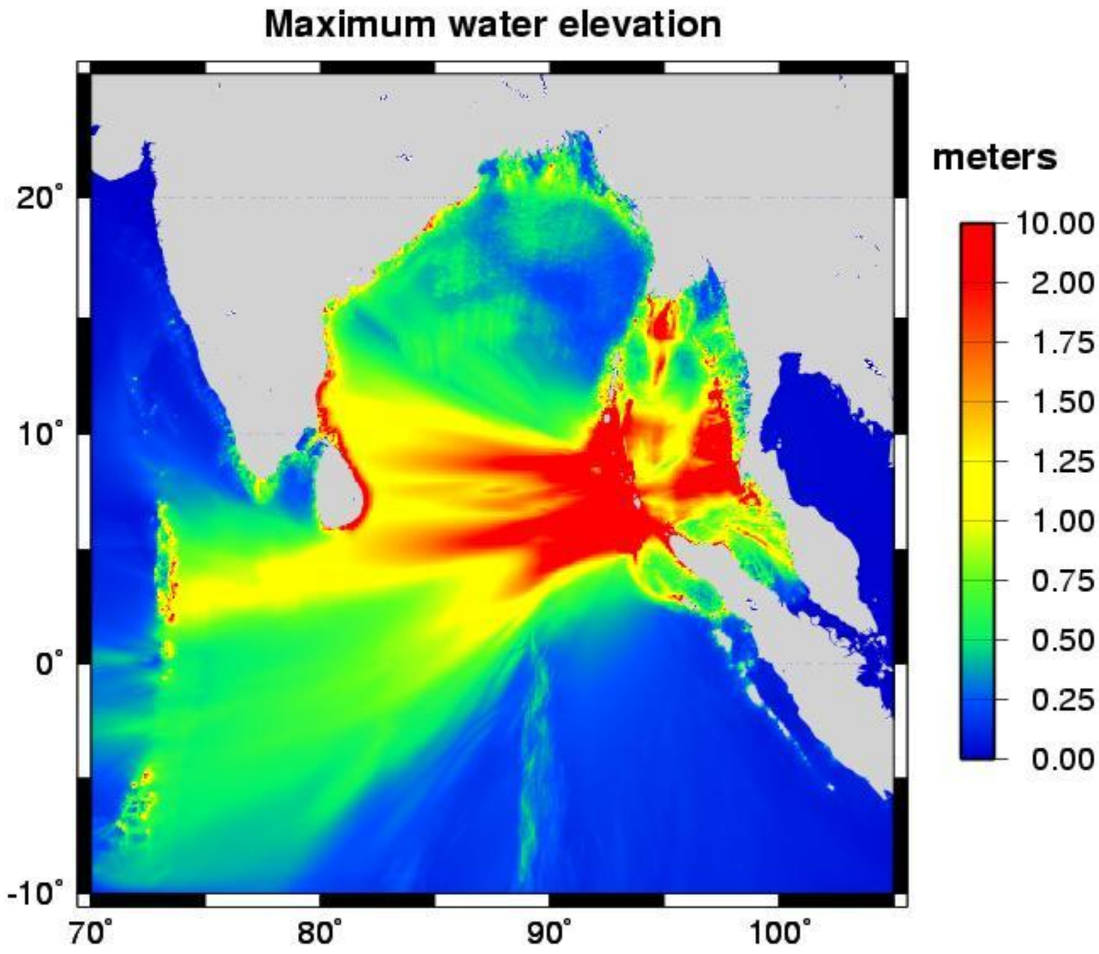

A.Piatanesi - INGV

Banda Aceh Overview

(Before Tsunami)
Imagery collected April 12, 2004
DigitalGlobe

(After Tsunami)
Imagery collected January 2, 2005
DigitalGlobe

South-East Asia

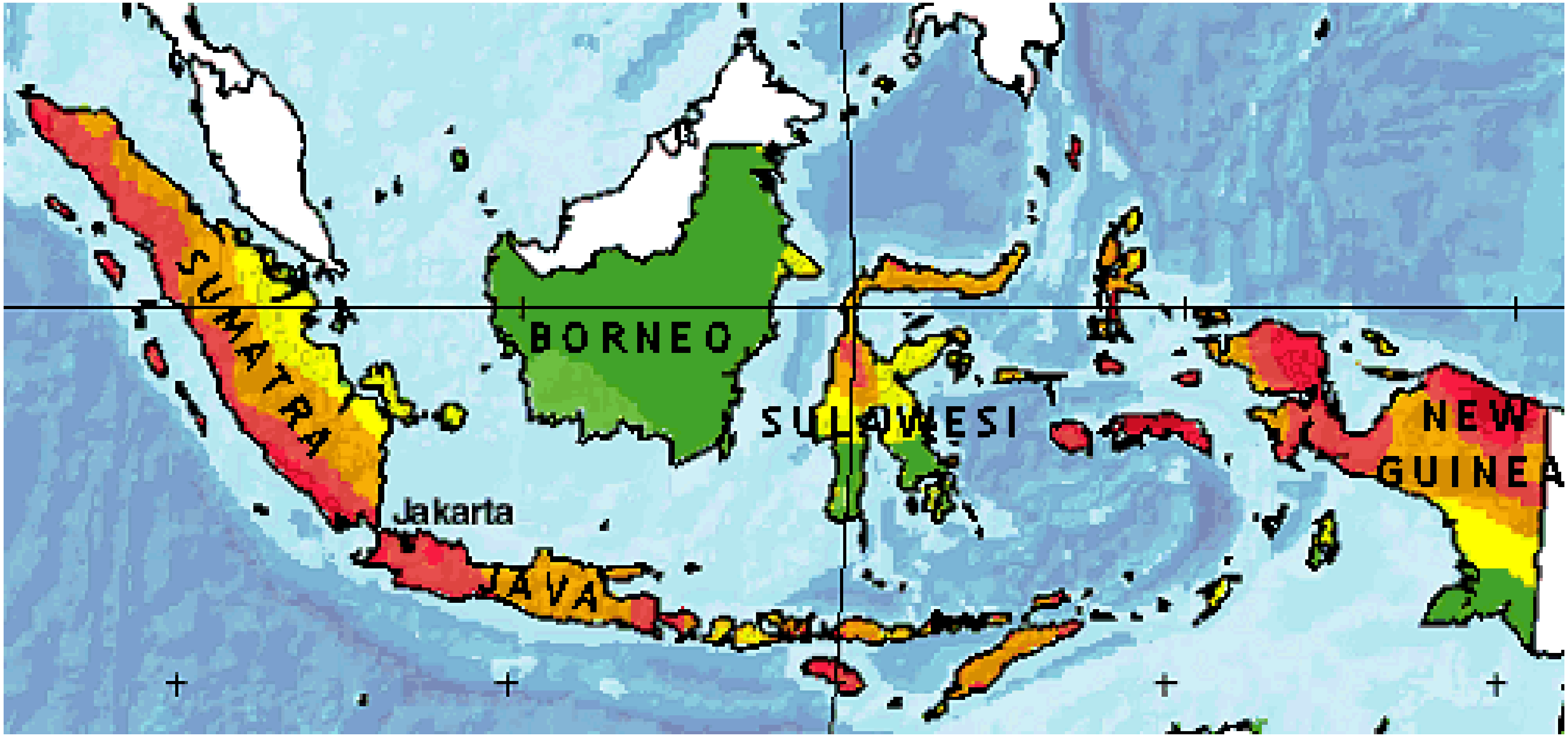

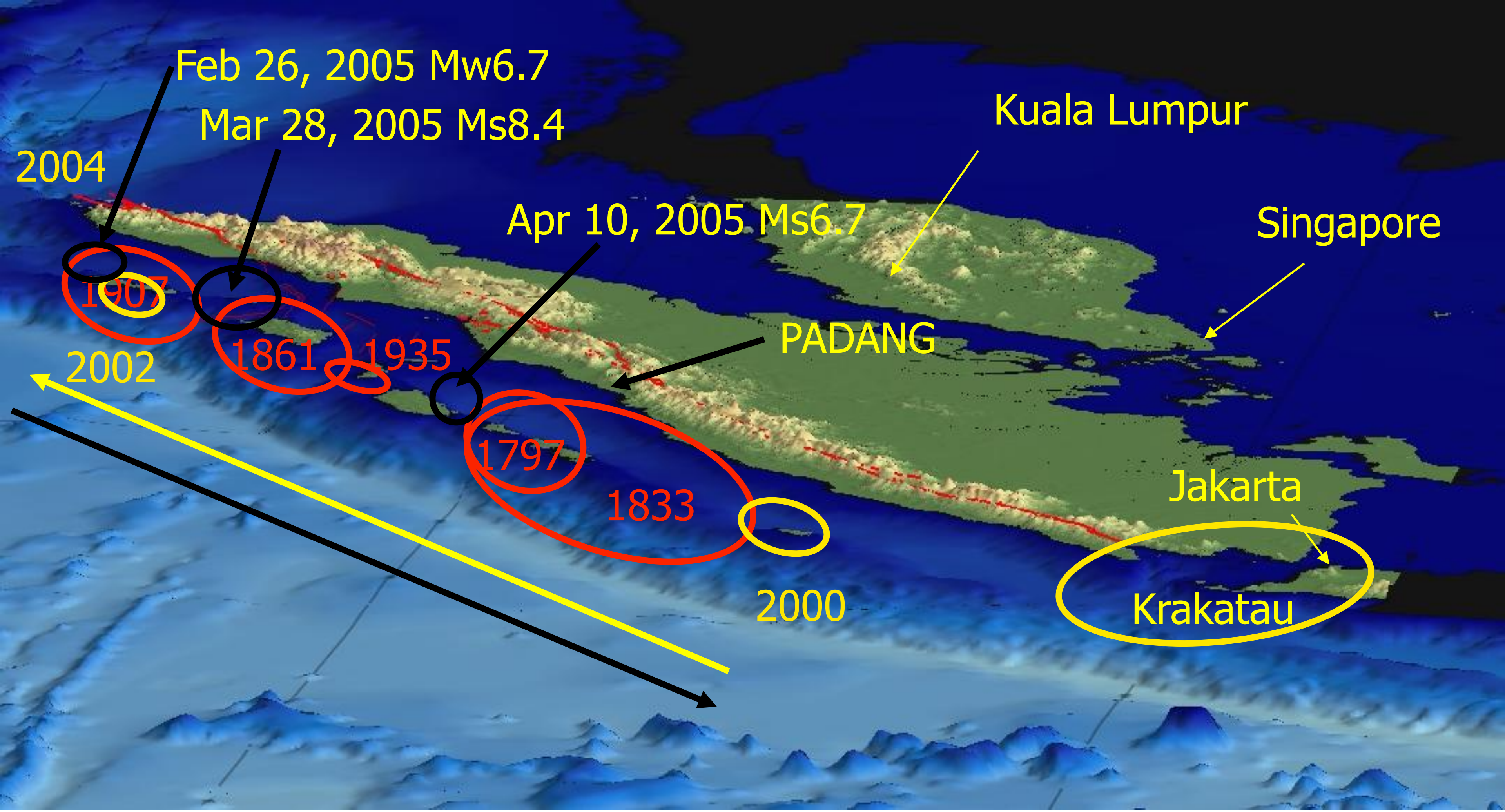

A flurry of ruptures have occurred since 2000

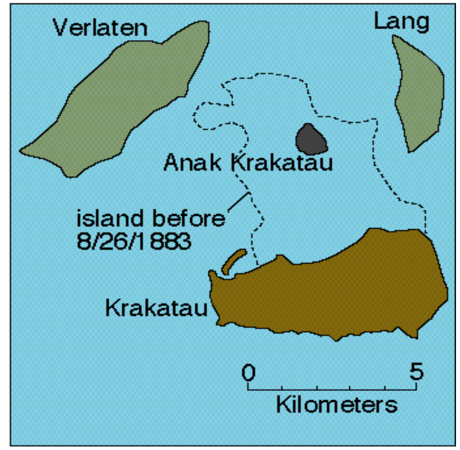

From Simkin and Fiske, 1983

Krakatau

1883 Aug 28/29

Next major eruption within 20 years

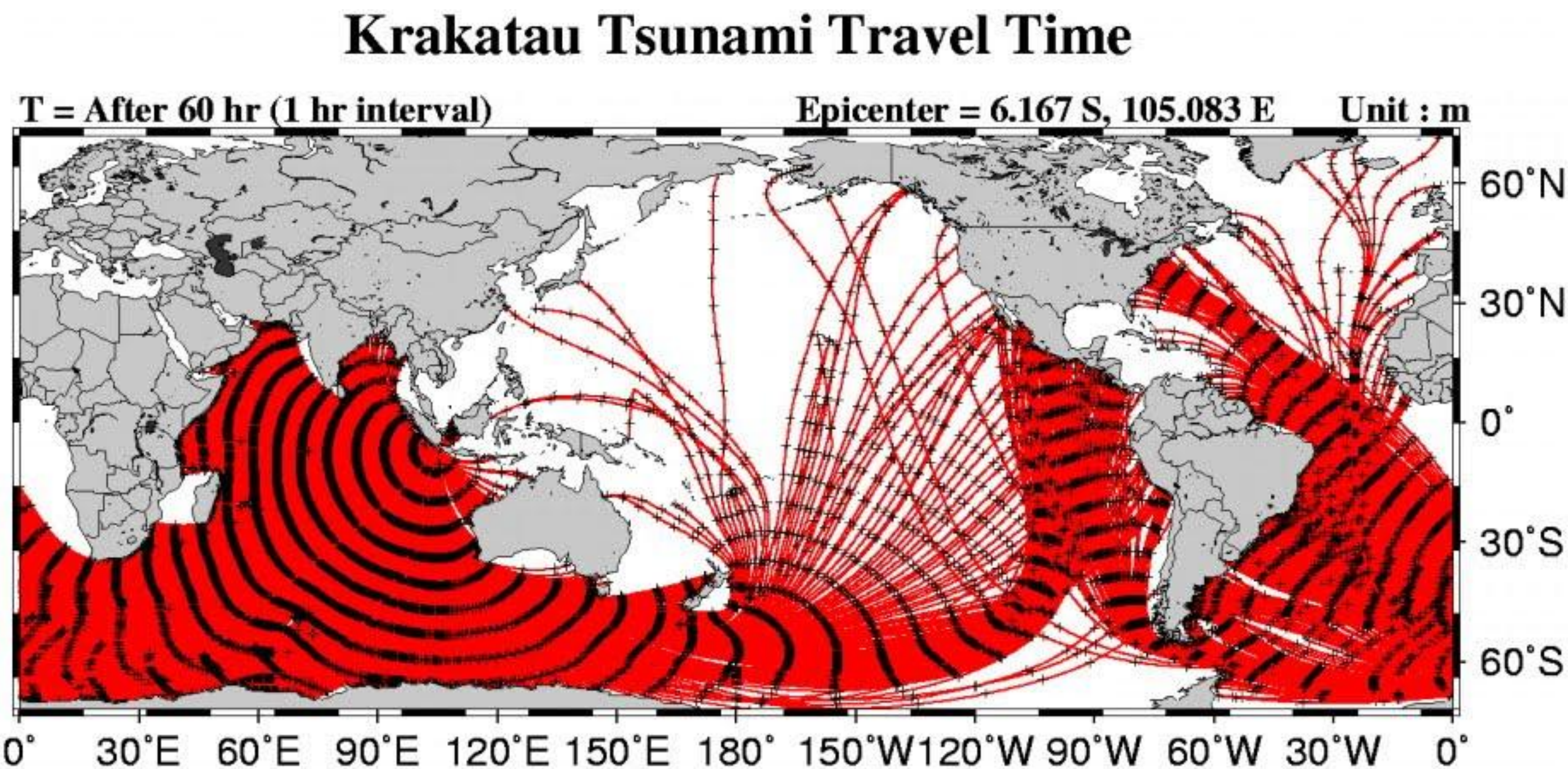
Krakatau Tsunami Travel Time
T = After 60 hr (1 hr interval)
Epicenter = 6.167 S, 105.083 E
Unit : m
60°N
30°N
0°
30°S
60°S
0°
30°E
60°E
90°E
120°E
150°E
180°
150°W
120°W
90°W
60°W
30°W
0°

Krakatau Volcanic eruption 1883 Aug.28/29

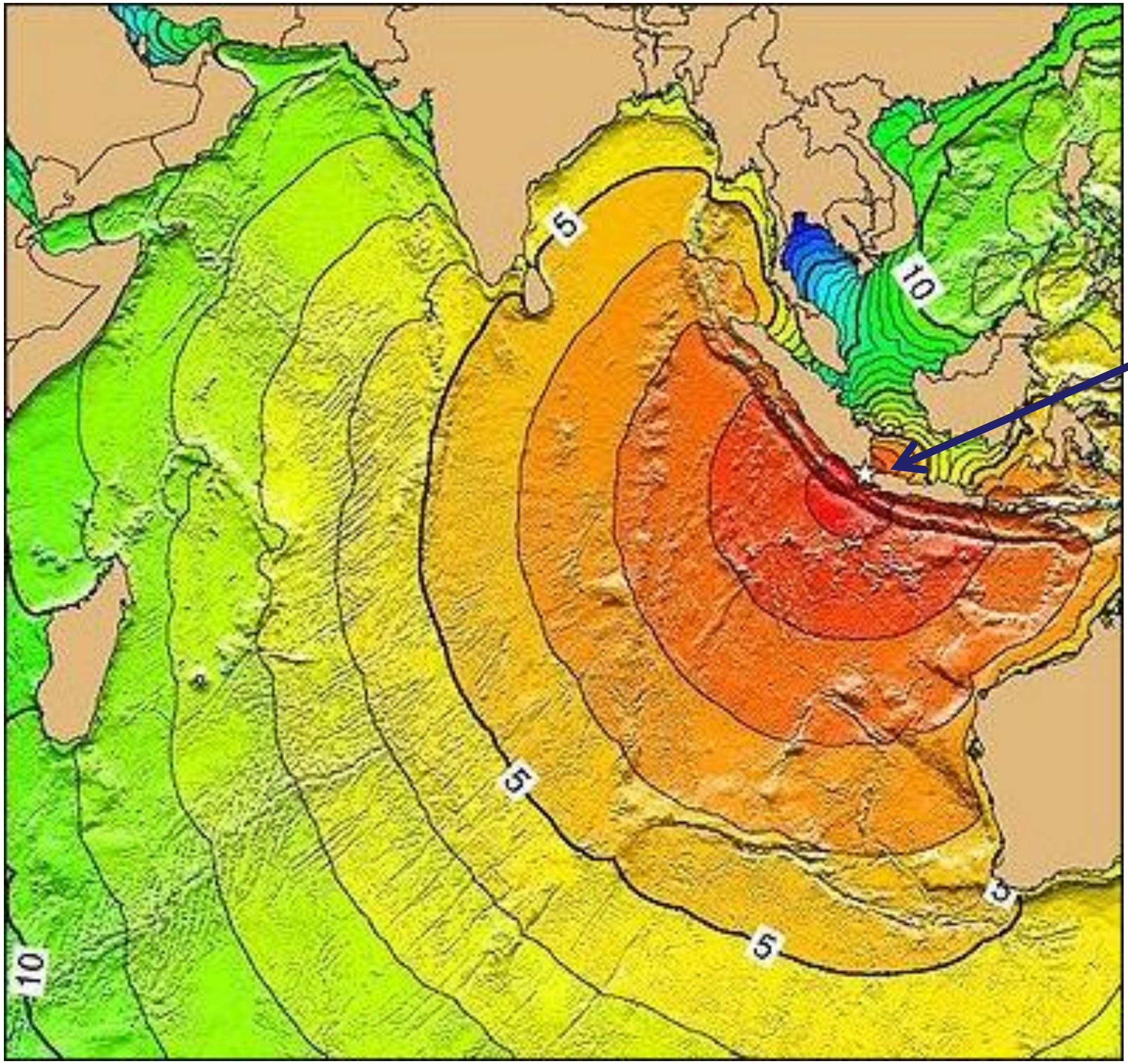

Krakatau

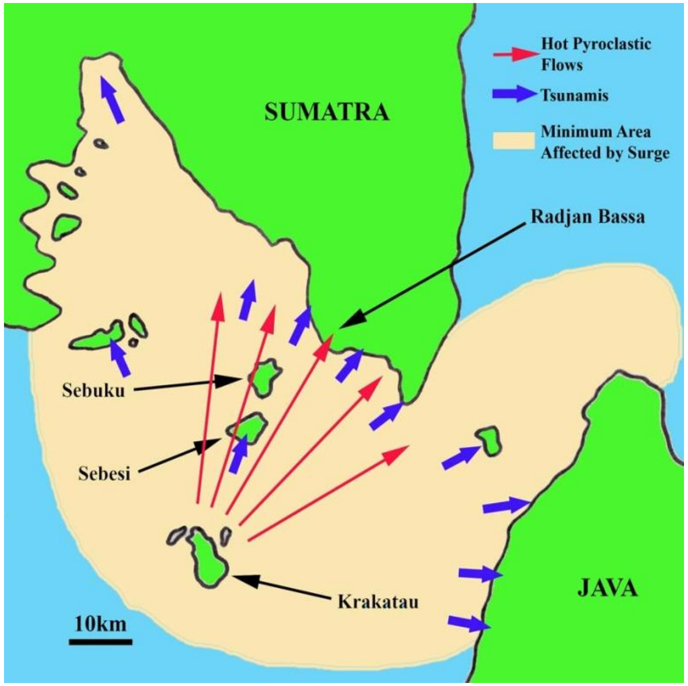

Krakatau
PiSAR-2
L-band
2013

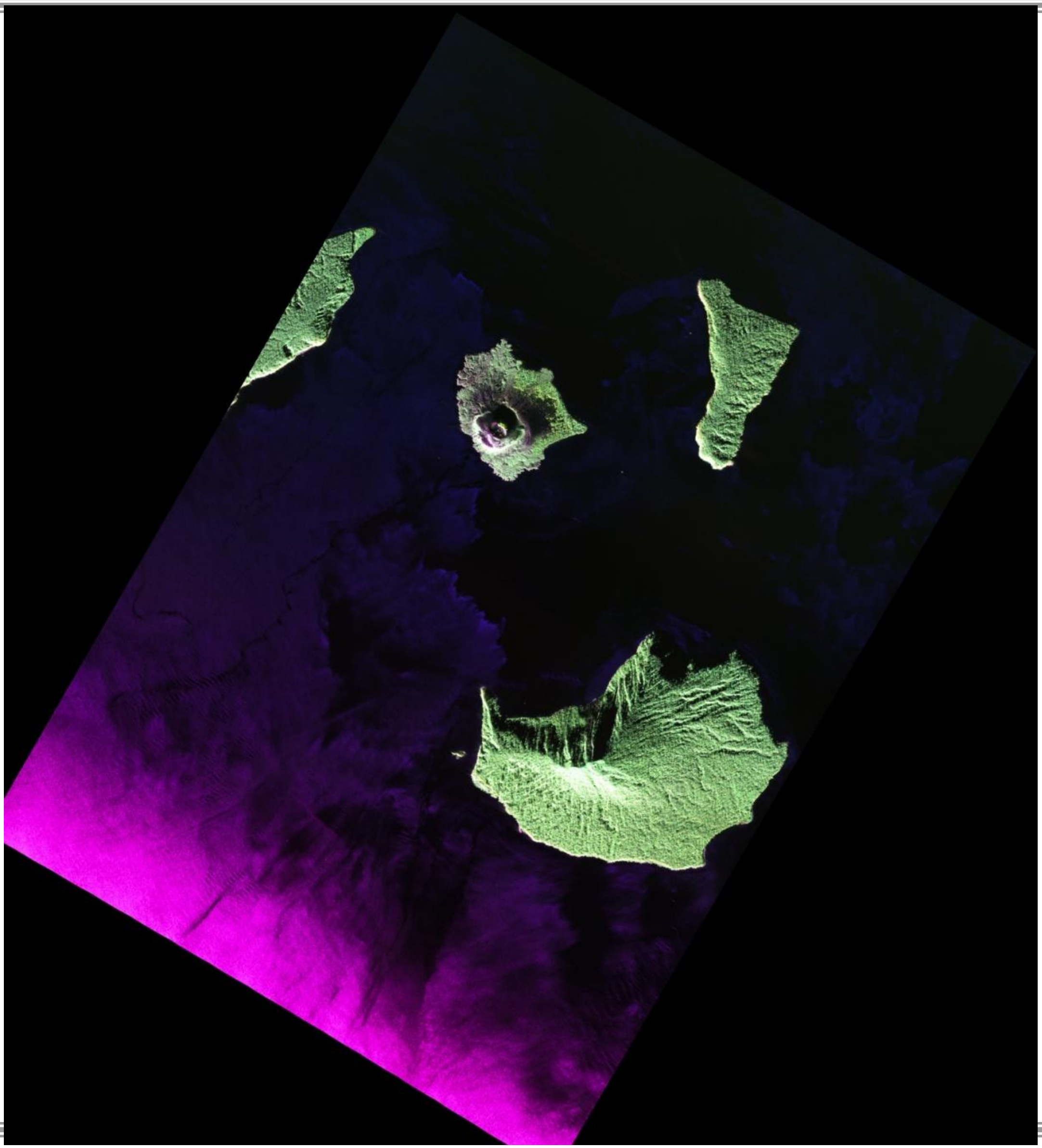

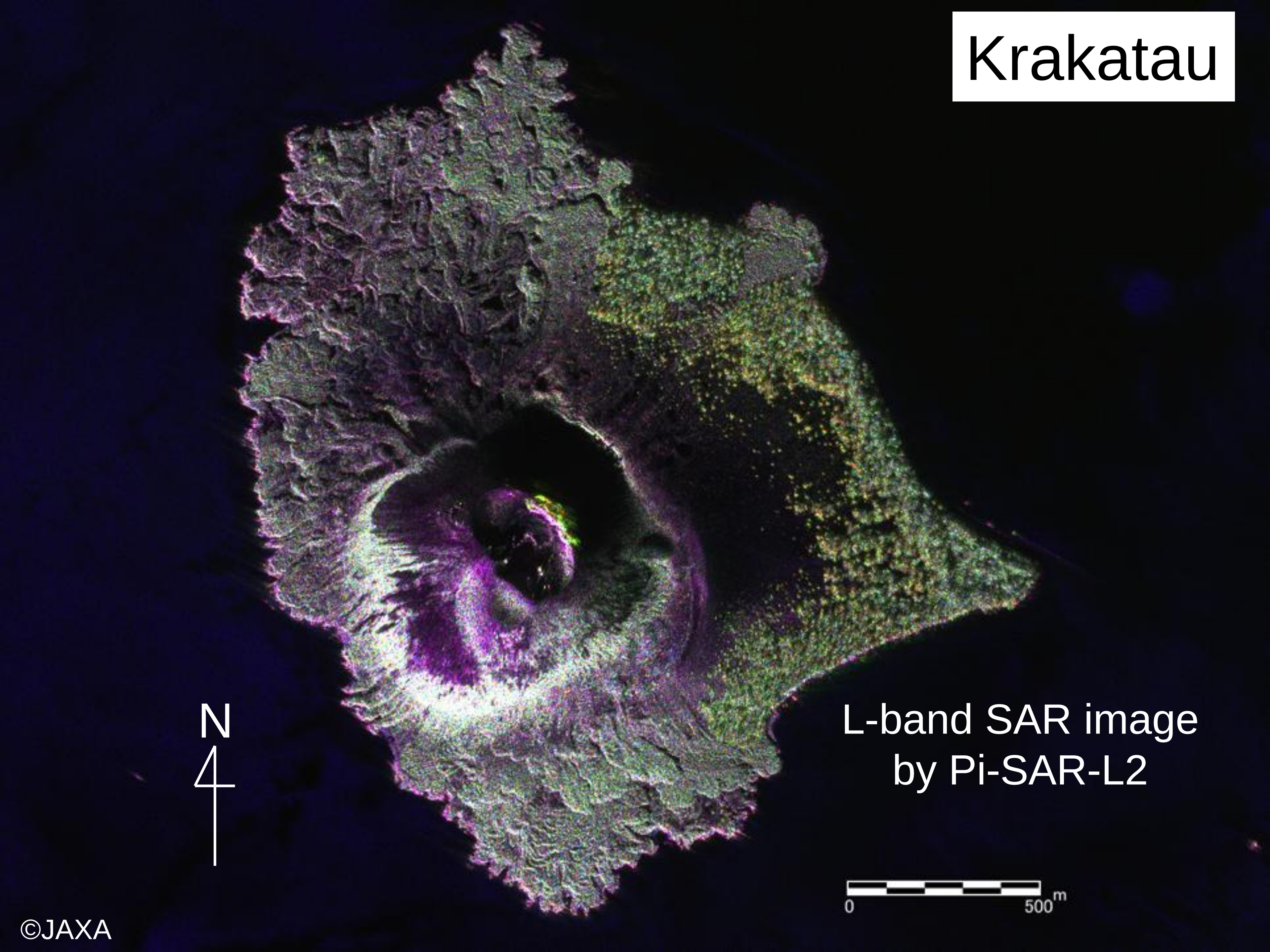
Krakatau
L-band SAR image
by Pi-SAR-L2
N
0
500
m
©JAXA

SAR Meteorology

- Although various airborne & satellite weather radars had been developed, the need for meteorological SAR is in urgent need because of detecting close to surface phenomena over land and ocean:

  The first positive implementation resulted from TerraSAR-X, being demonstrated for both cloud cover and volcano plume assessment; and the

  Addition of a K_a Band fully polarimetric POLSAR Satellite sensor would be of great use.

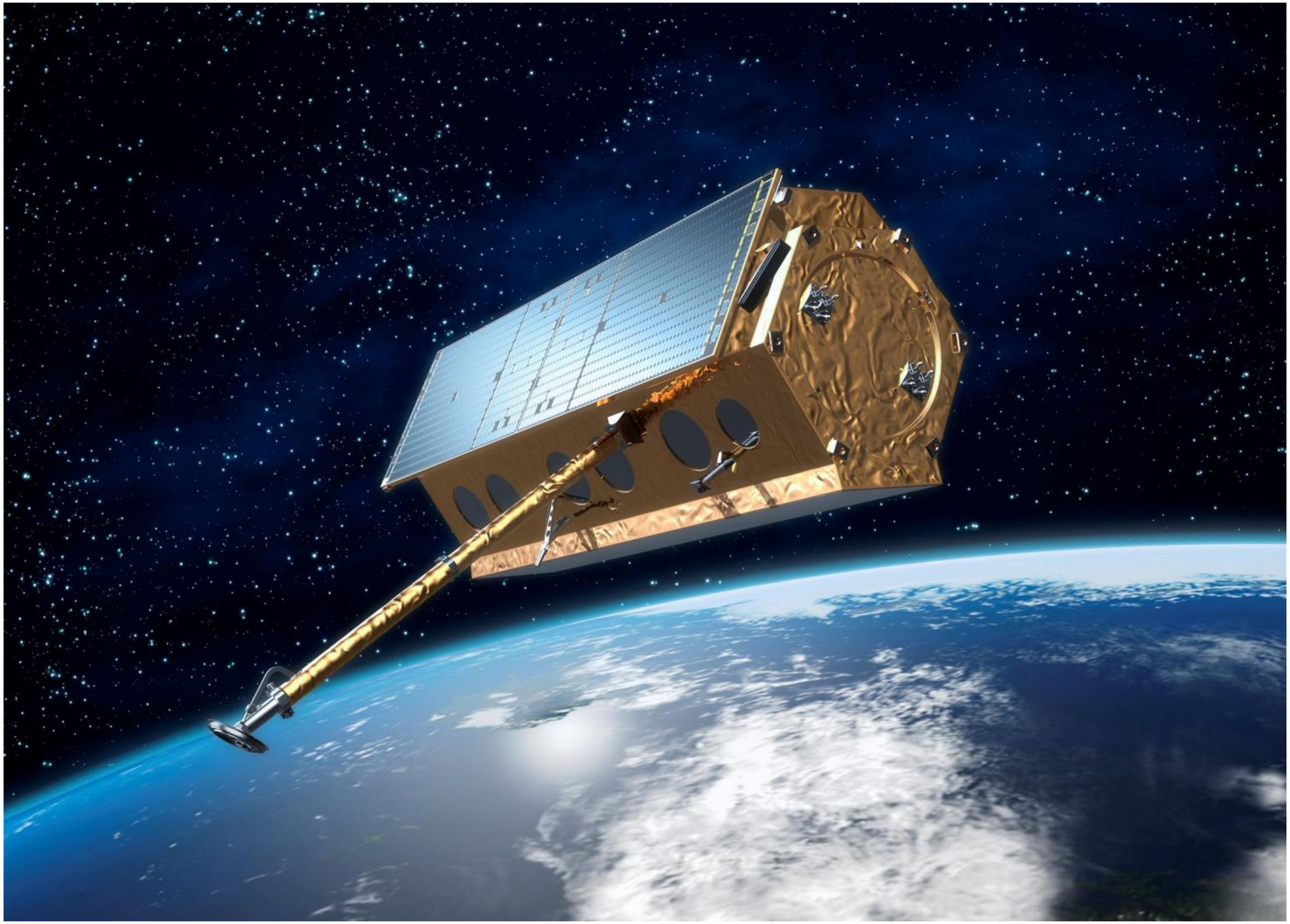

The TerraSAR-X Satellite

Physical interpretation of rain cell signatures

- Partial backscattering at hydrometeors (precipitation volume)
- Attenuation of incident wave

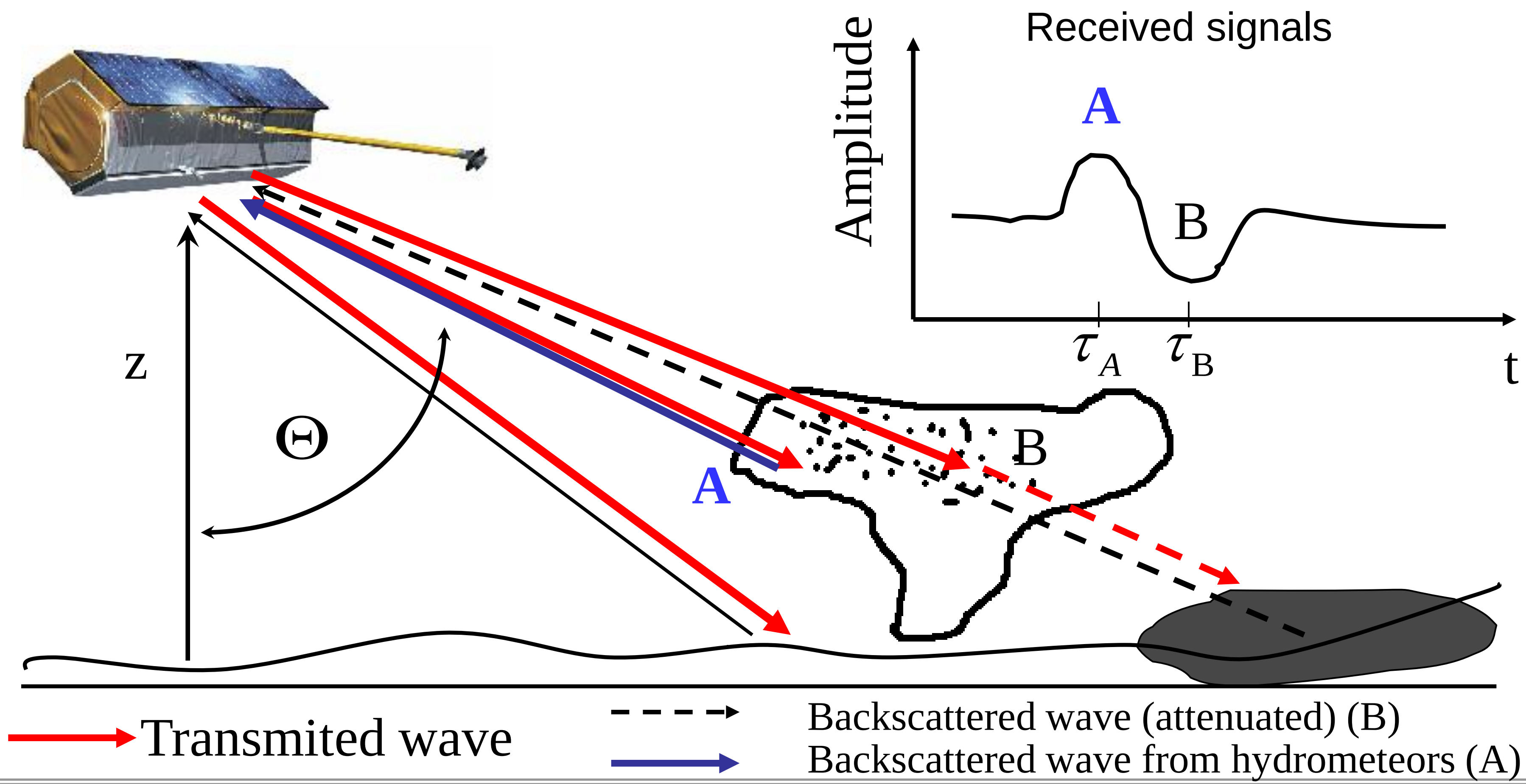

Overview of effects

Effects:

- delay
- **attenuation**
- noise
- scintillation

caused by:

- atmospheric gases
- **rain, precipitation**
- clouds, fog
- ionosphere

Transmission spectrum of the atmosphere / Attenuation

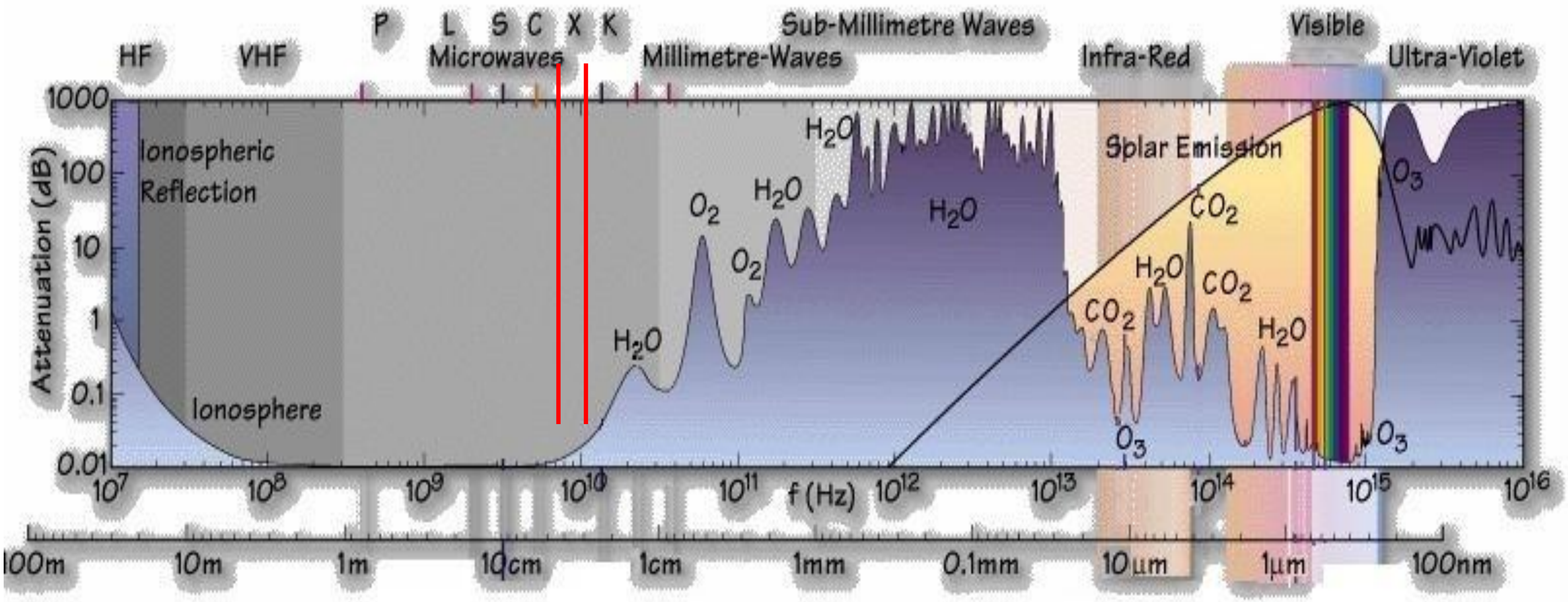

Gaseous attenuation negligible
→ focus on precipitation

→

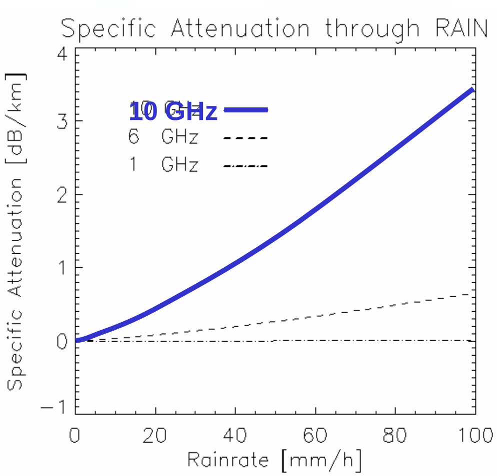

Slant range reflectivity profile („A-scope“) for the rain cell cut from a very recent TerraSAR-X measurement

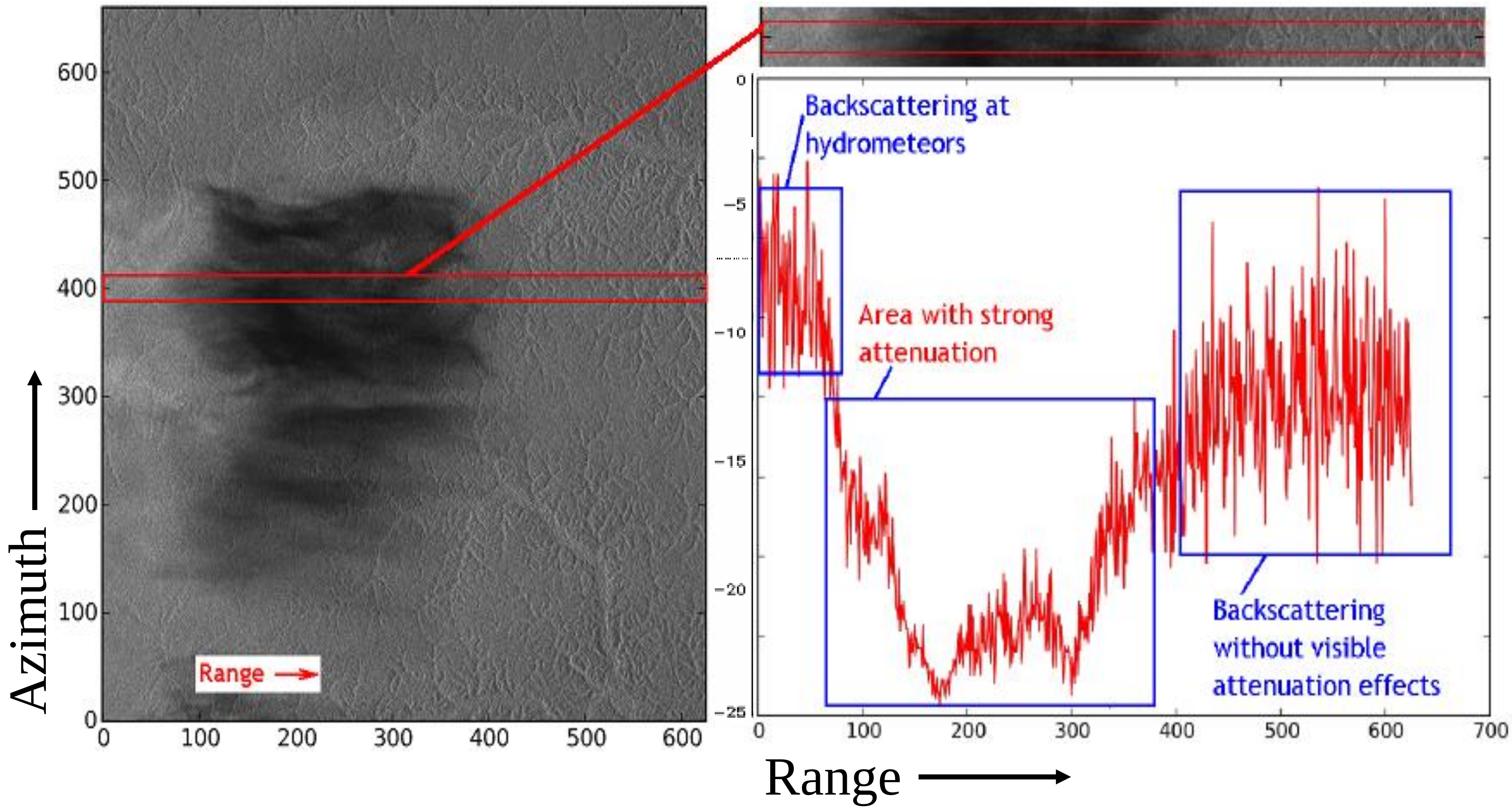

Recent examples of propagation effects recorded withTerraSAR-X

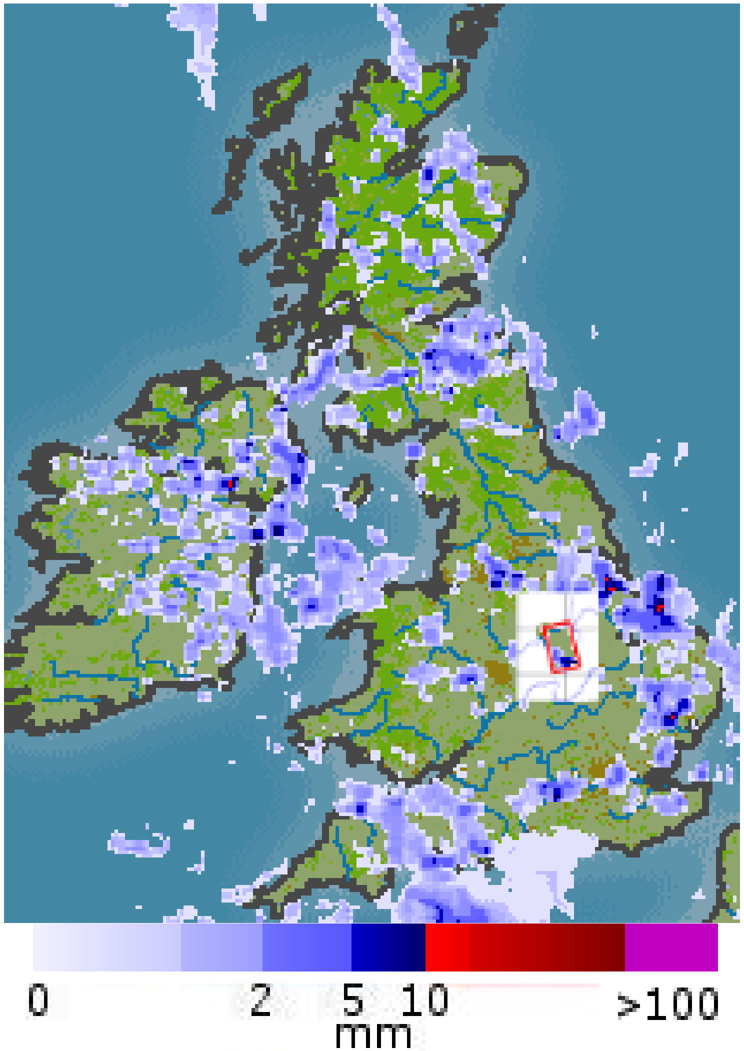

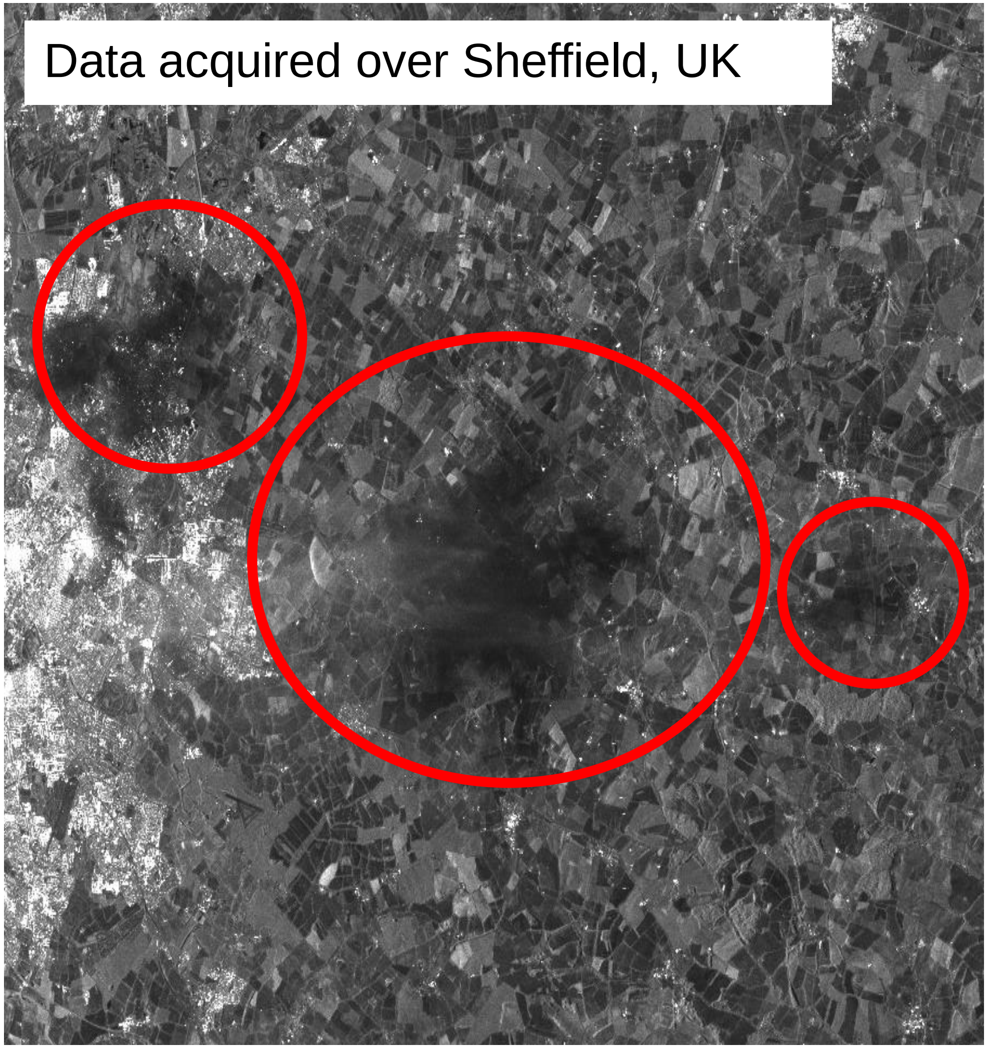

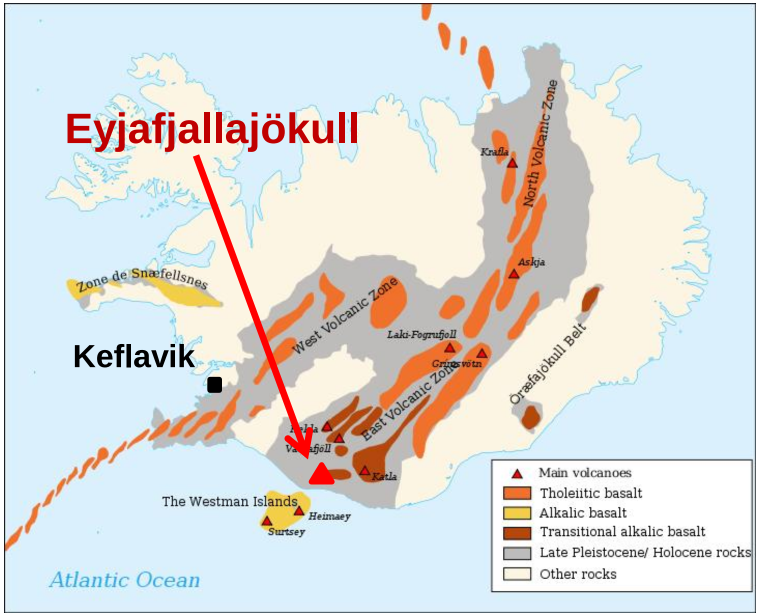

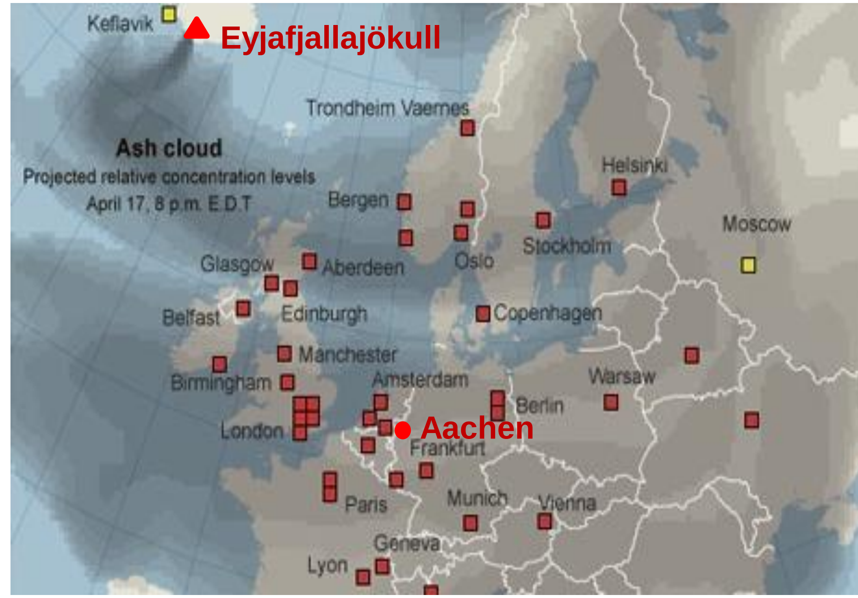

Iceland, Eyjafjallajökull Volcano



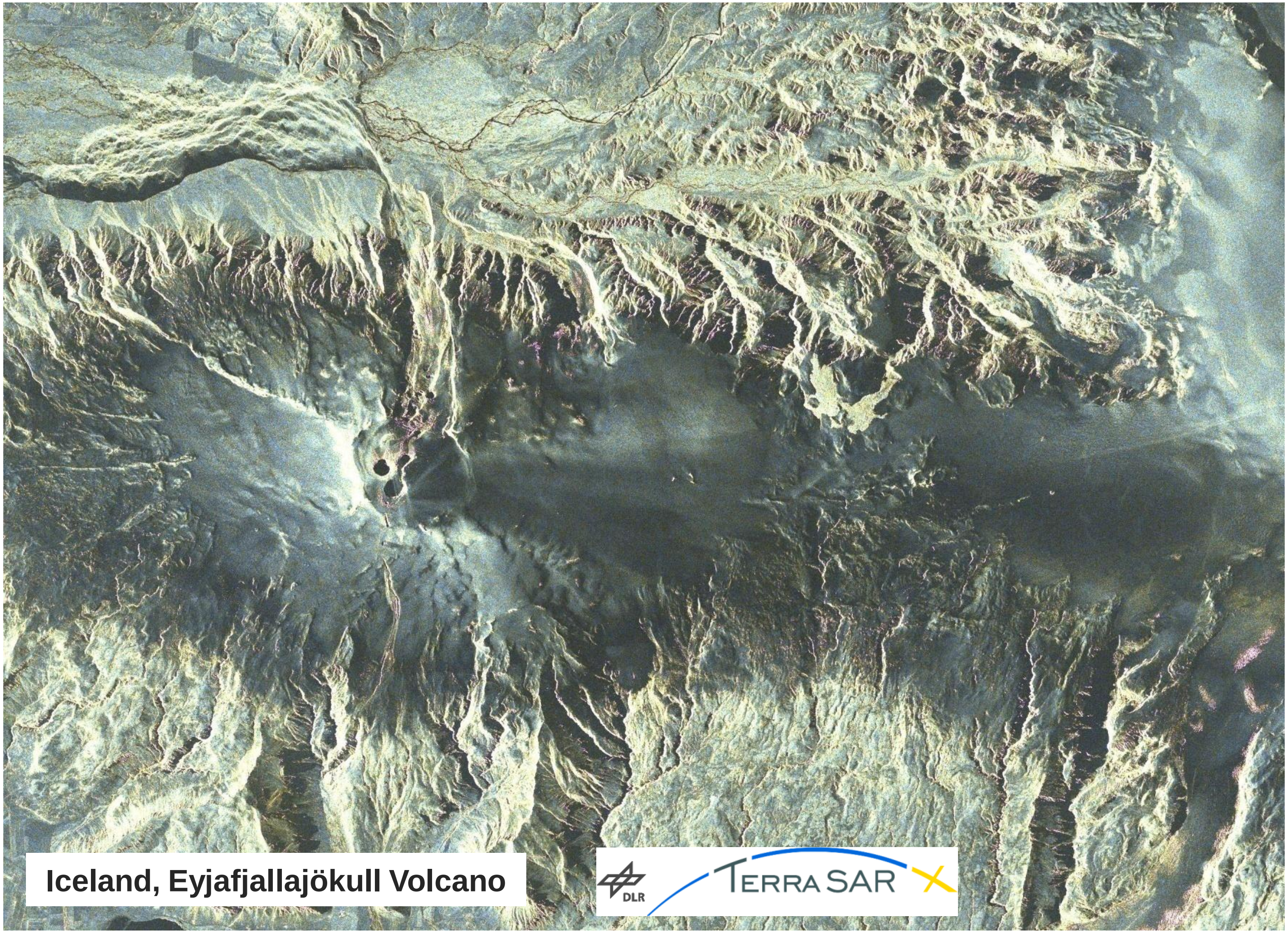
Iceland, Eyjafjallajökull Volcano
DLR
TERRASAR X

NASA-JPL UAVSAR on Global Hawk

Most affected regions

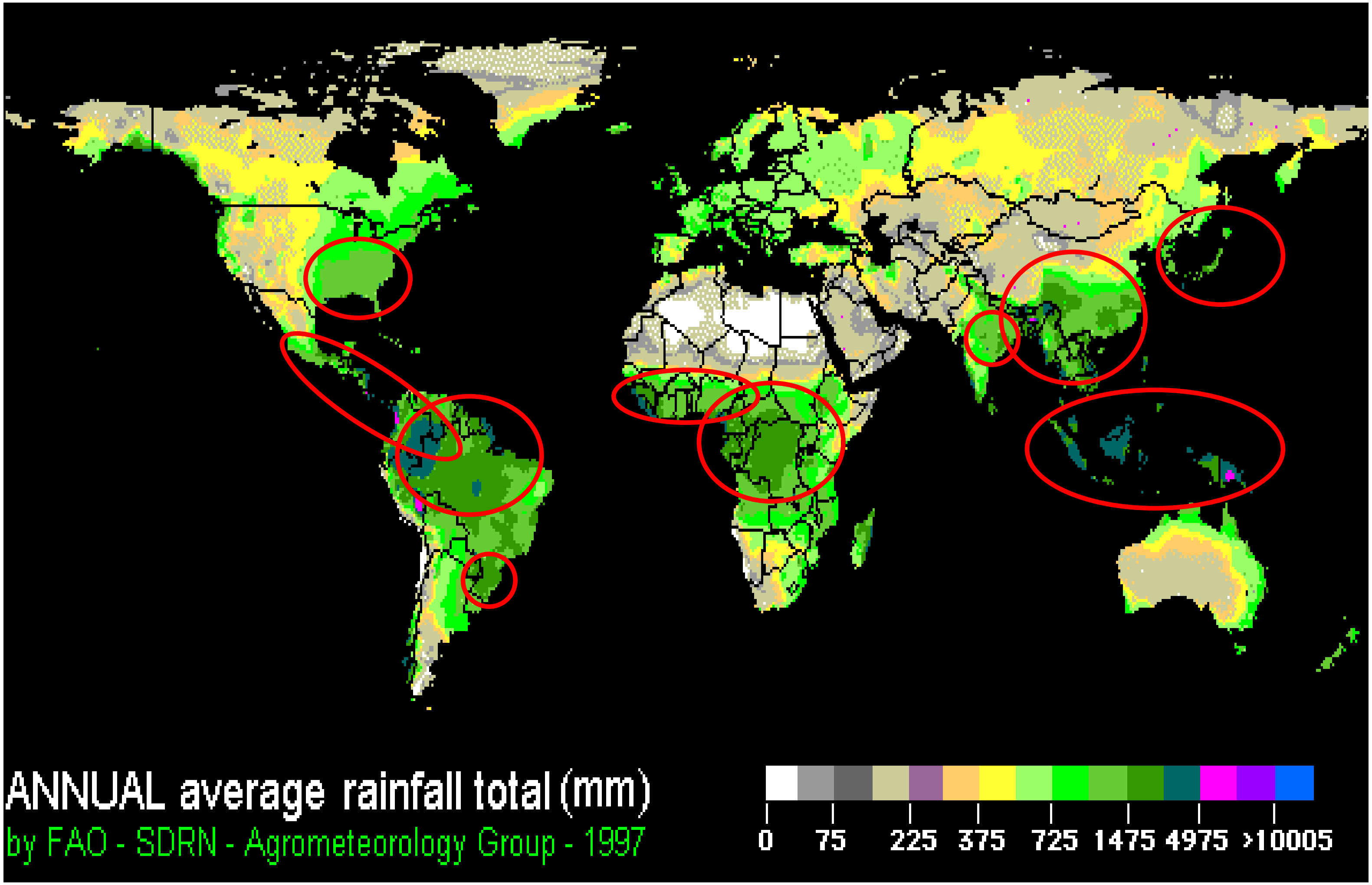

Upcoming High-altitude PolSAR Sensors

UAVSAR JPL
Gulf-Stream III
L (Quad - Pol)

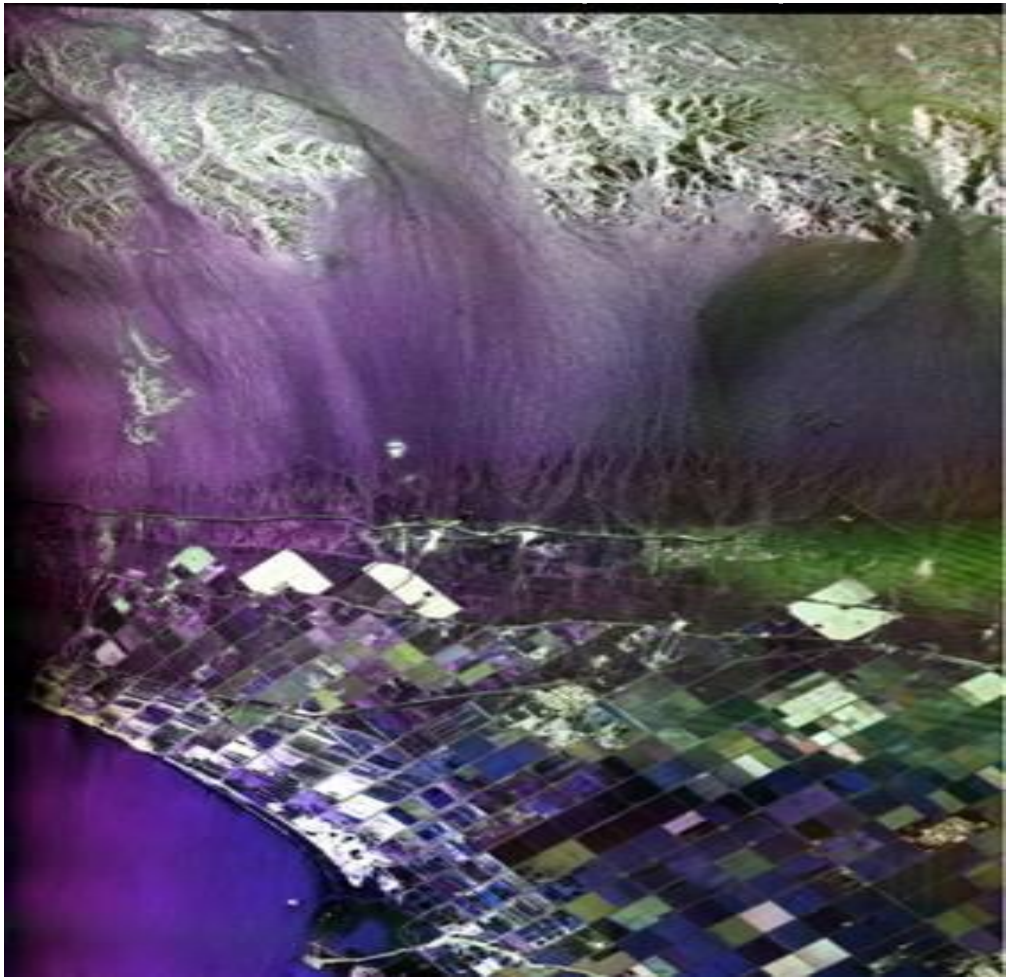

(HH-VV, HV, HH+VV)

Prediction of Future Megastorms: California & East Coast

PART-IV, Needs for Multi-Band &Tandem Satellites & Future Outlook

14. New space borne Tandem SAR satellite sensors, P, L, S, C, X, K, V, W-bands
15. Additional Back-up Airborne FSAR Test measurements in all pertinent bands
16. Development of additional UAW Multi-Band POLSAR sensors
17. Development of Equator-orbiting wide-swath, multi-band POLSAR Satellite sensors
18. Identification of regional needs for Equator-orbiting sensors: Pacific ocean & islands,

    Africa & Atlantic, South & Central America
19. Natural and Man-made Interferences and its reduction
20. Acquisition of Natural Background Terrestrial Radiation
21. Textbooks and Tutorials

Outlook & Future Needs

- New Sensors, space-borne: TandemSAR-X, TandemSAR-L (Destiny), . . .
-New Sensors, air-borne: F-SAR (P, L, S, C, X, K, V, W) , …
- New Sensors, ultrahigh air-borne: JPL-UAV (Global Hawks), ...

- Algorithm Developments: Fully Polarimetric RP-POLinSAR assessment

- Applications: Focused increase providing clear-cut successes

POLinSAR 2011 Single & Tandem Space-borne POL-SAR Sensors, Increase number of Text books & Training Workshops

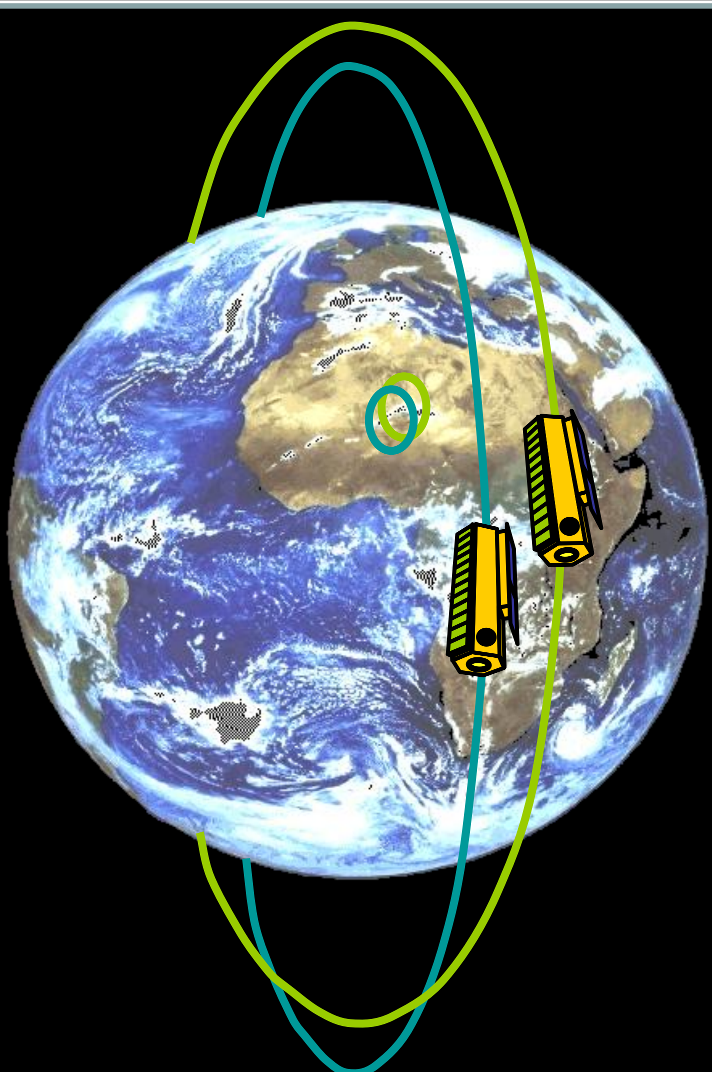

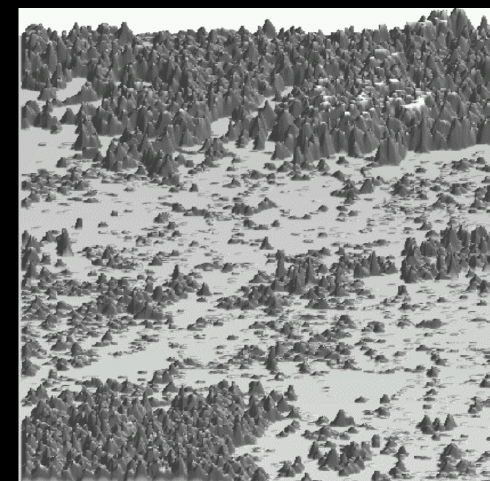

Global Monitoring of Bio-, Geo-, Cryo- and Hydrosphere processes with hith temporal and spatial resolution.

(Prof. A. Moreira – POLINSAR09)

Radar Interferometry

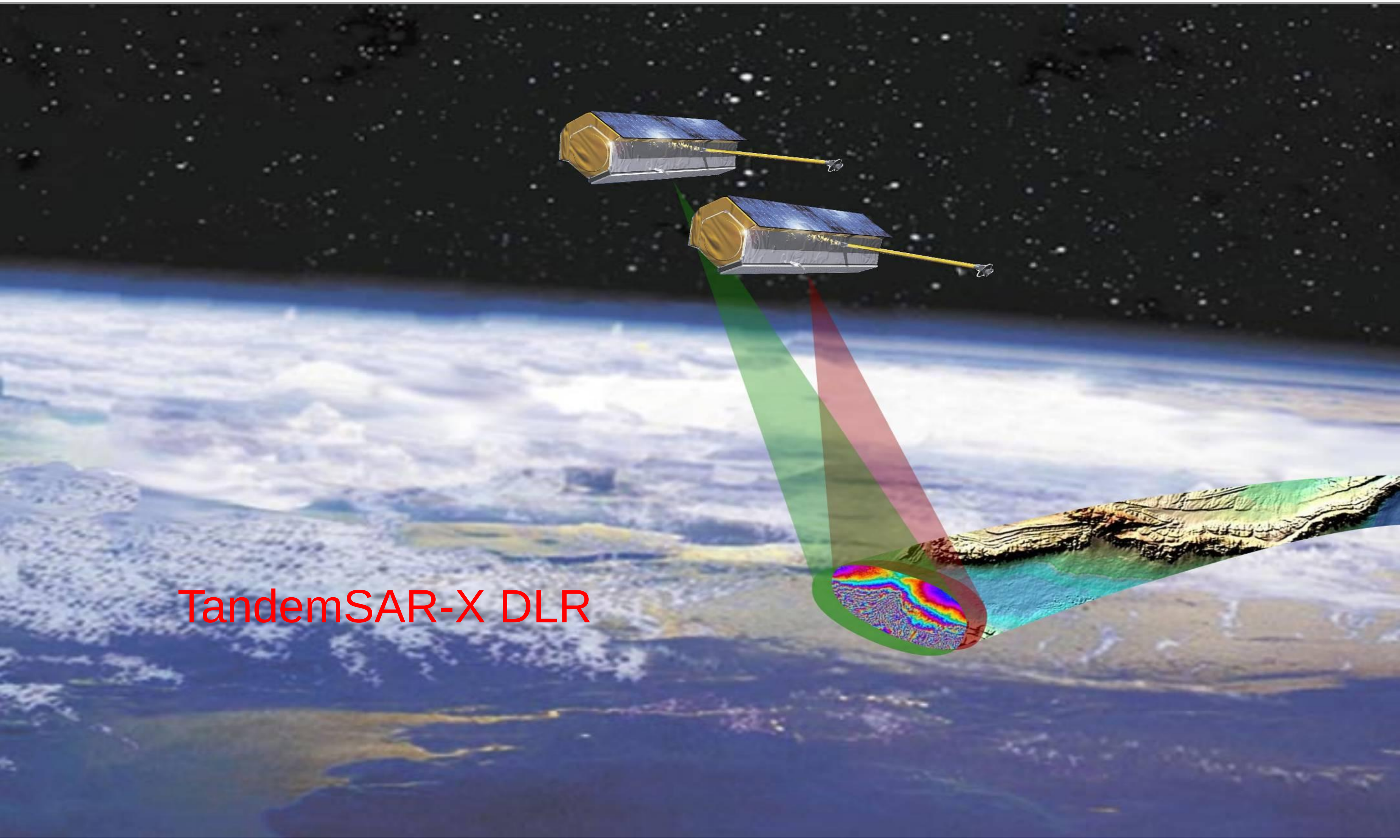
TandemSAR-X DLR

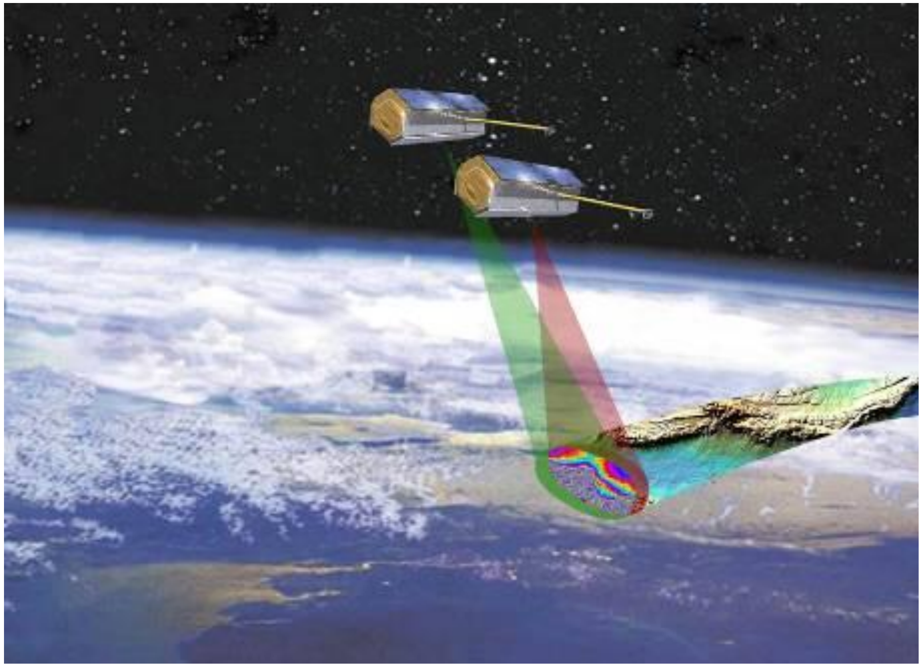

TerraSAR – X (1 & 2)
(2010)

Pol – InSAR Sensors

TanDEM-X

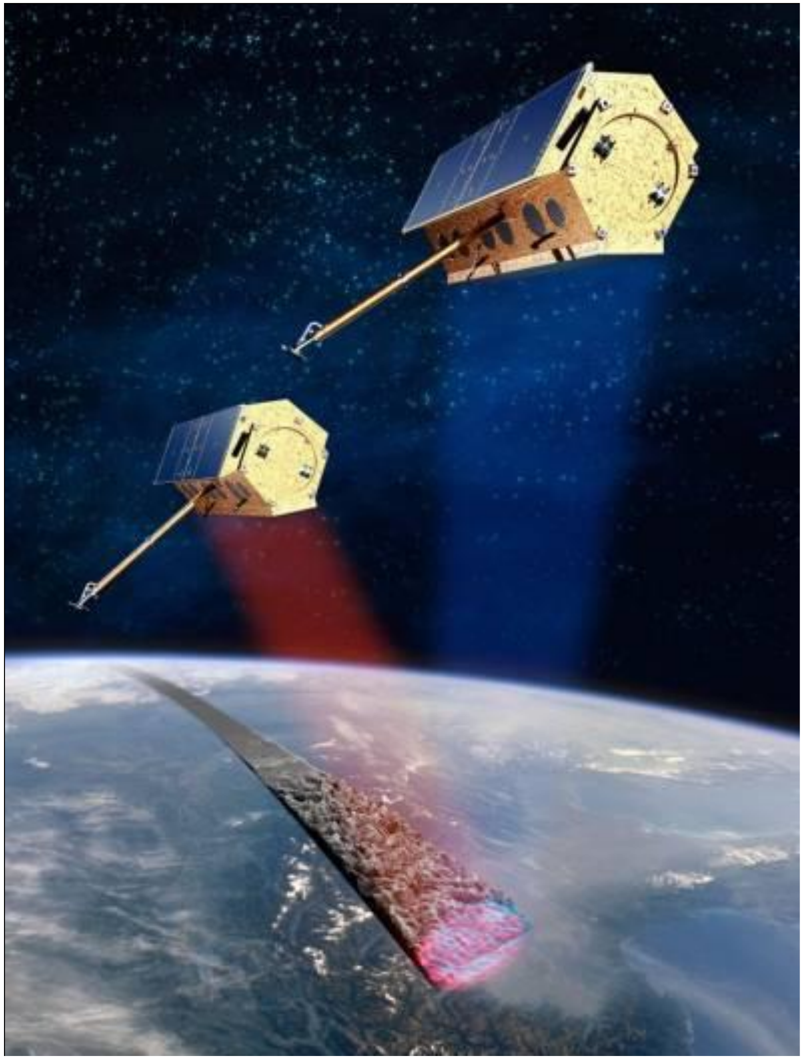

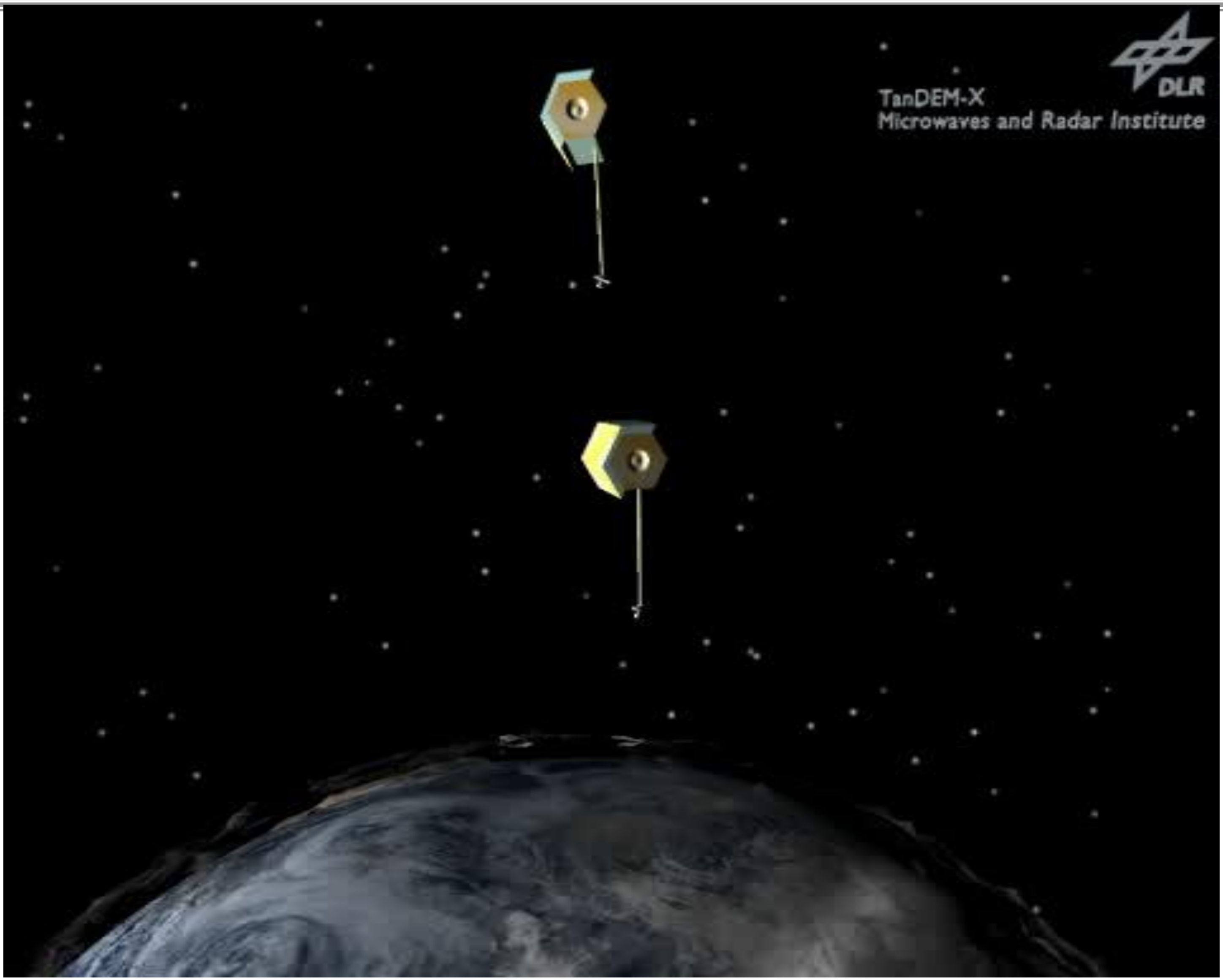
TanDEM-X
Microwaves and Radar Institute
DLR

TandemSAR-L (Destiny): JAXA & DLR

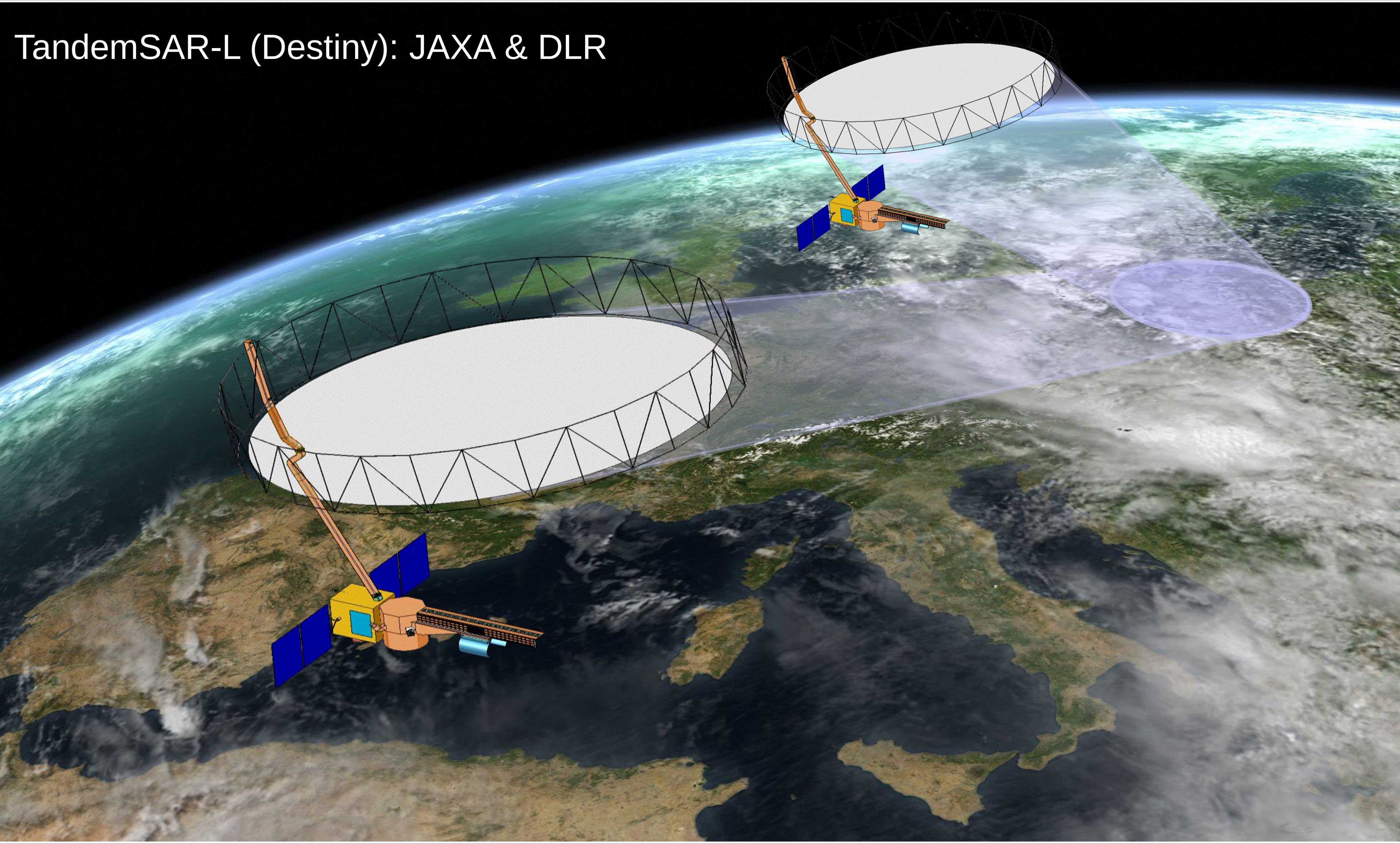

Tandem-L: Imaging Capacity and Coverage Analysis for a Nearly Eqautorial Orbit

German Aerospace Center - DLR

Microwaves and Radar Institute

Oberpfaffenhofen

Digital Beamforming with Reflector Antennas

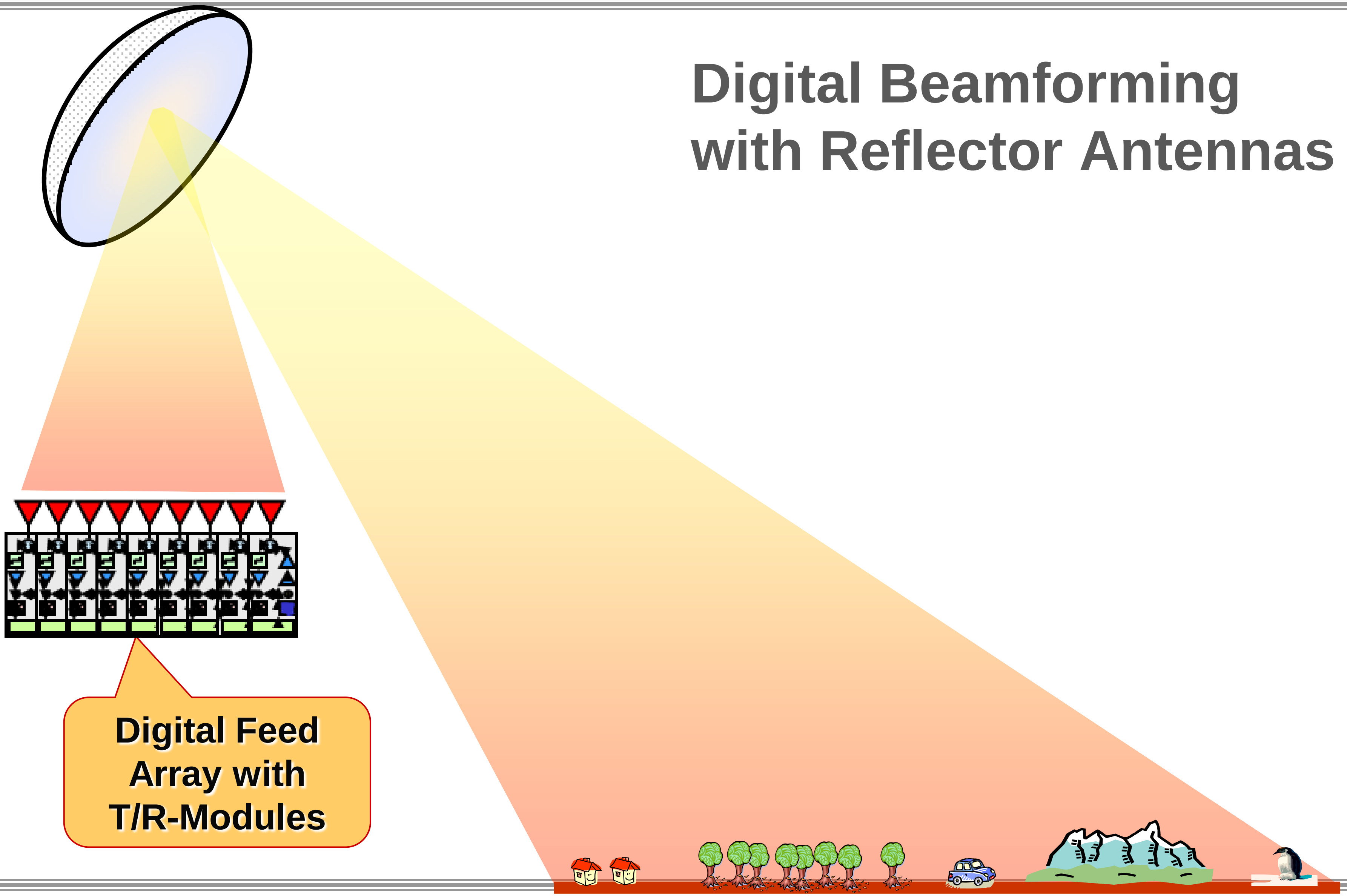

Digital Beamforming with Reflector Antennas

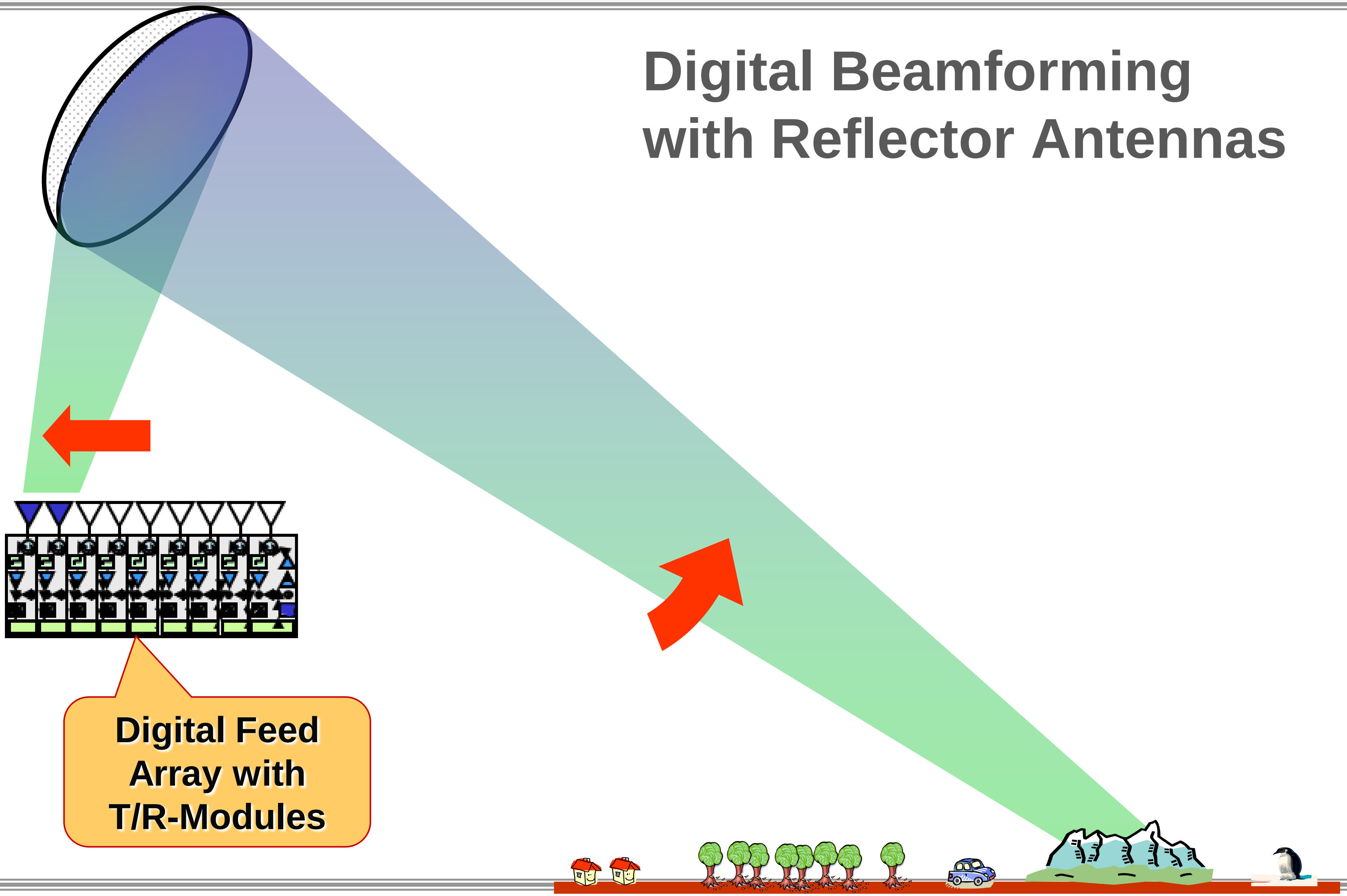

Digital Beamforming with Reflector Antennas

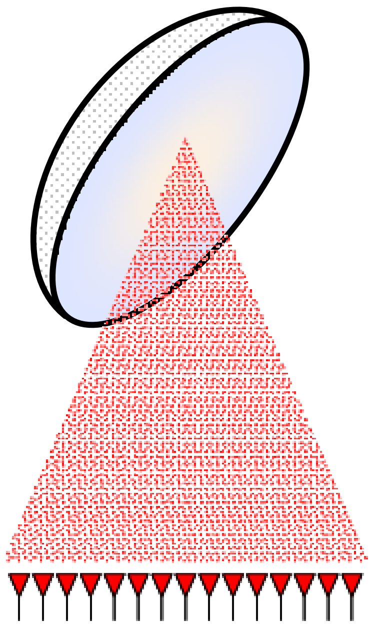

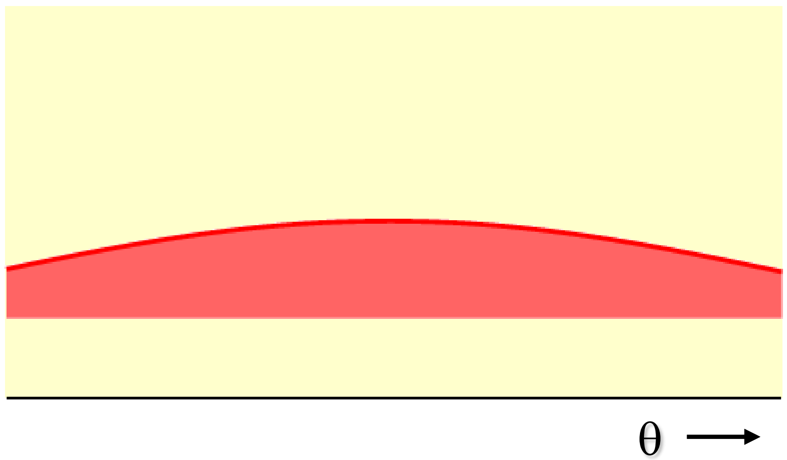

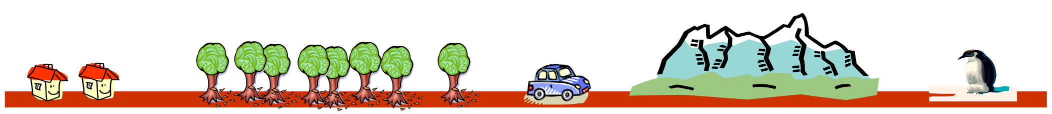

Simulation Parameters for a Tandem-L Satellite with a nearly Equatorial Orbit

Repeat Periode	3 days
Repeat Cycles	44
Near Range	180 km
Swath Width	547 km
Orbit Inclination	20 degrees

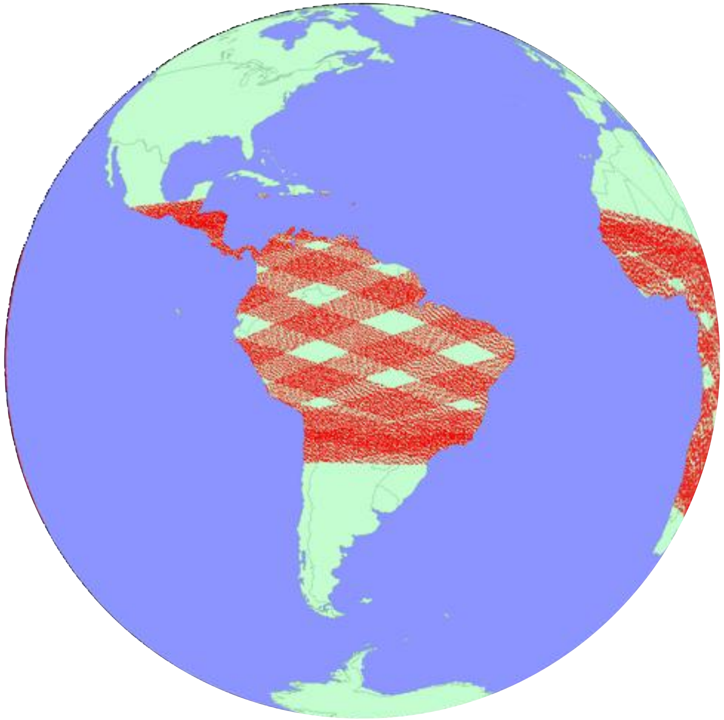

Comparison of Imaging Capability (Polar Orbit)

TanDEM-X

1 global coverage / year

Tandem-L

2 global coverages / week

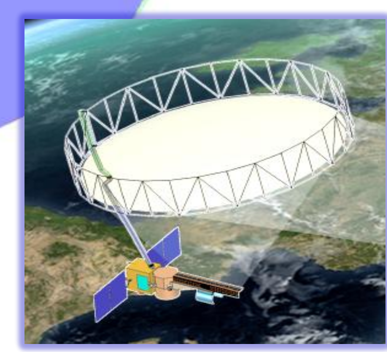

1

Days

Development of equatorially orbiting wide-Swath, multi-band POLSAR sensor technology

- The challenge is to develop equatorially orbiting SAR, preferably POL-SAR satellite sensors, within the desirable P/L/S/C/X/Ka multi-bands, which does pose severe technological problems due to the steep incidence-angle illumination on one hand, and because of the fact that the major SAR Technology Designers reside far outside the equatorial belt not being excited about SAR sensor development for the tropical belt anywhere.
- Once this urgent goal is achieved, local regions could be observed daily up to 12 to 14 times well suited for equatorial monitoring within orbits of +/- 20* latitude, covering both the land and ocean regions essential for environmental protection and meteorological forecasting, respectively, on a hitherto unprecedented global level.

Satellite Image of Terrestrial Vegetation Cover

Simulation Parameters for a Tandem-L Satellite with a nearly Equatorial Orbit covering total Equatorial belt, +/-23.5°

Repeat Periode	3 days
Repeat Cycles	44
Near Range	180 km
Swath Width	547 km
Orbit Inclination	20 degrees

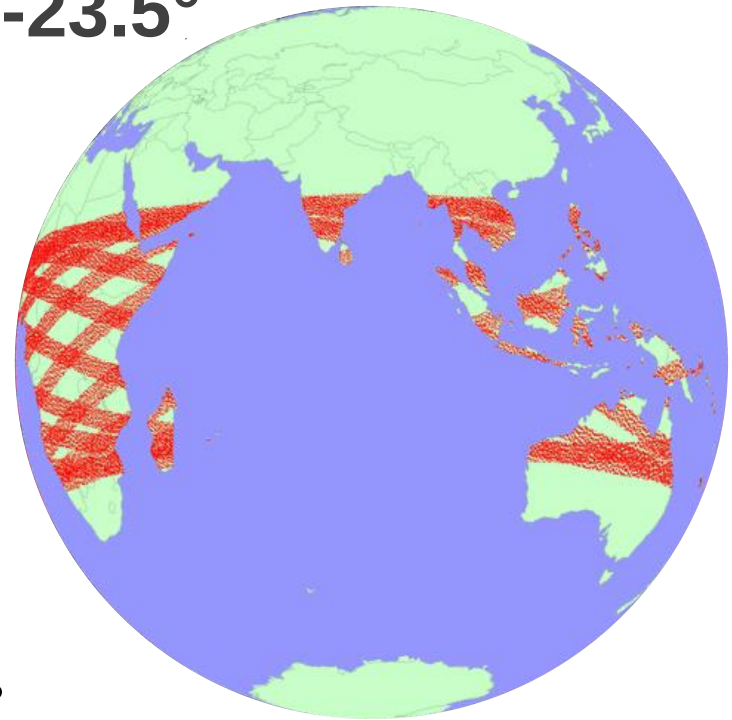

Change of Inclination Angle from 35 ° to 20°

Simulation Parameters for a Satellite with a 500 km Swath (Access Range) and a nearly Equatorial Orbit, +/-23.5°

Repeat Periode	3 days
Repeat Cycles	46
Near Range	180 km
Swath Width	680 km
Orbit Inclination	35 degrees

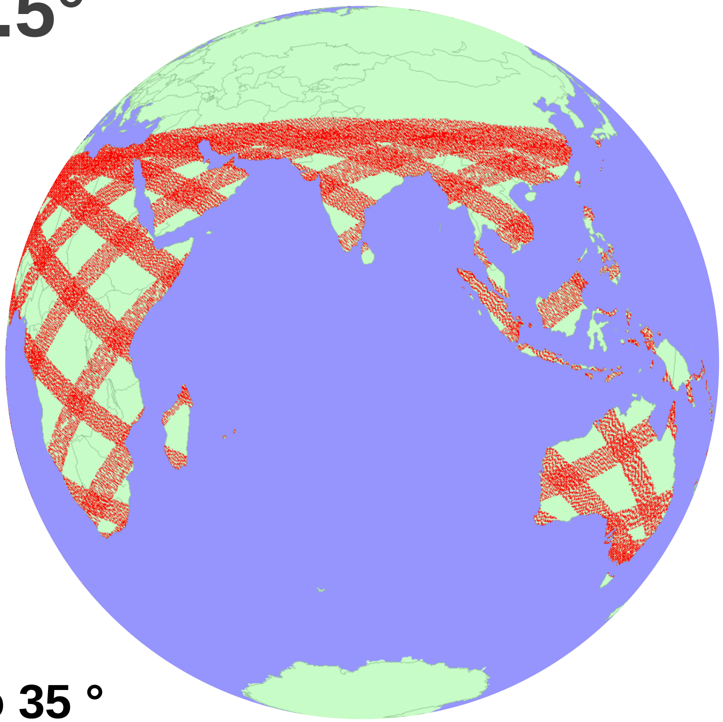

Change of Inclination Angle from 20 ° to 35 °

Daily Coverage for SAR in Nearly Equatorial Orbit covering +/- 18°

Repeat Periode	1 day
Repeat Cycles	15
Swath Width	370 km
Near Range	180 km
Far Range	550 km
Looking Direction	Right
Orbit Altitude	554 km
Orbit Inclination	8 degrees

Change of Inclination Angle from 12° to 8 °

Daily Coverage for SAR in Nearly Equatorial Orbit

Repeat Periode	1 day
Repeat Cycles	14
Swath Width	600 km
Near Range	180 km
Far Range	780 km
Looking Direction	Left
Orbit Altitude	880 km
Orbit Inclination	12 degrees

Change of Inclination Angle from 8° to 12°

Tandem-L

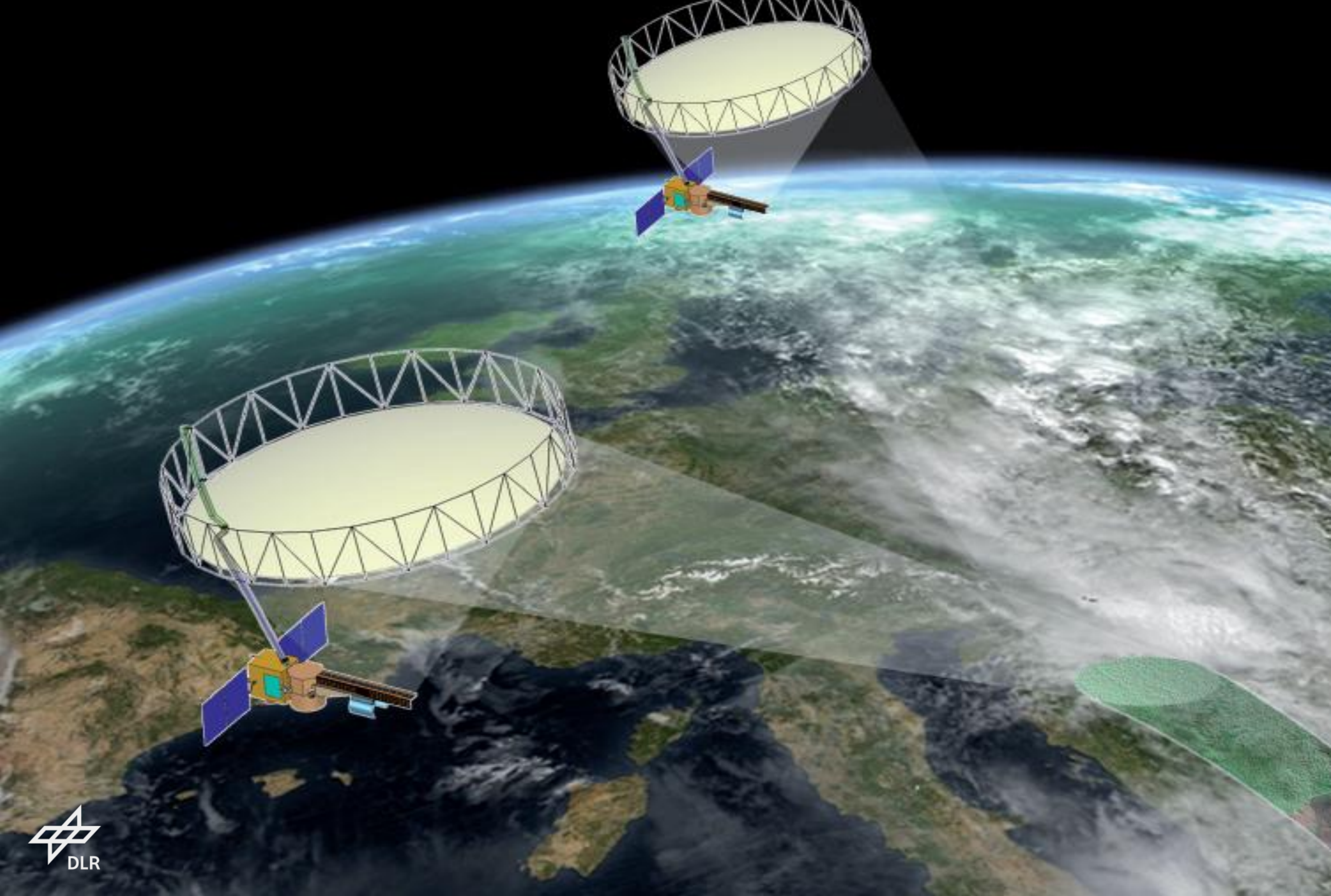

LAPAN-A2 ORBIT PROFILE

(14 pass per 24 hr / orbit time 100 minutes and stay above horizon at about 10 minutes)

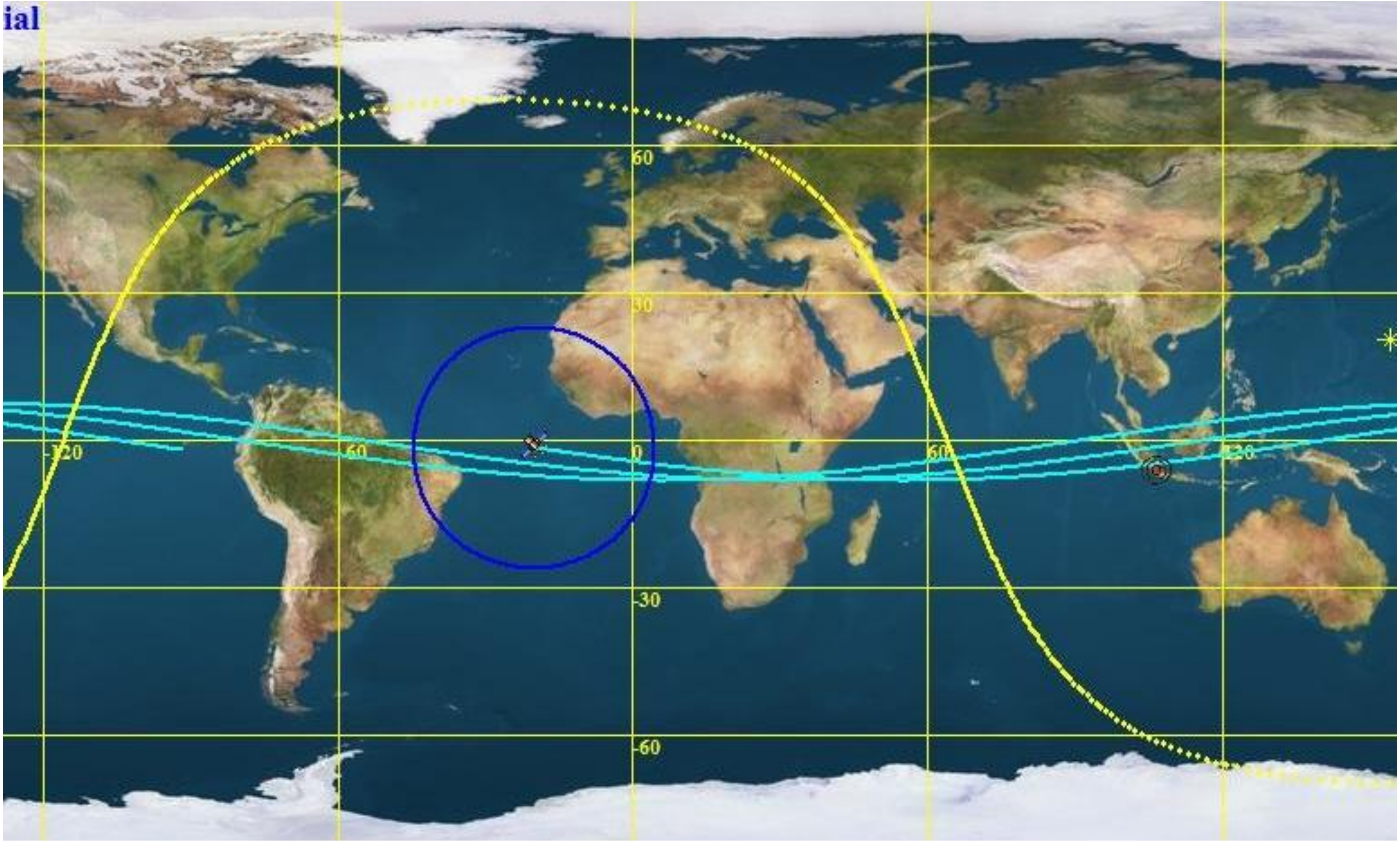

Recent Advances in Fully Polarimetric Space SAR Development and Its Applications

Conclusions:

The Vector (Polarization) Electromagnetic Spectrum:
A Natural Global Treasure

***Terrestrial Remote Sensing with PolSAR* :**
The *Radiology of the Health of the Earth*
at all weather and volcanic conditions
and at day and night ⇔ leading to the
Diagnostics of natural and man-made diasters